Measurements and Detailed Analysis of Seeded High-Gain Free-Electron Lasers at FLASH

Dissertation zur Erlangung des Doktorgrades
an der Fakultät für Mathematik, Informatik und Naturwissenschaften
Fachbereich Physik
der Universität Hamburg

vorgelegt von

Tim Plath

aus Dortmund

Hamburg, 2017

Gutachter der Dissertation:	Prof. Dr. Jörg Rossbach Dr. Jörn Bödewadt
Zusammensetzung der Prüfungskommission:	Prof. Dr. Caren Hagner Dr. Jörn Bödewadt Dr. Tim Laarmann Prof. Dr. Gudrid Moortgat-Pick Prof. Dr. Jörg Rossbach
Vorsitzende der Prüfungskommission:	Prof. Dr. Caren Hagner
Datum der Disputation:	05.10.2017
Vorsitzender Fach-Promotionsausschusses PHYSIK:	Prof. Dr. Wolfgang Hansen
Leiter des Fachbereichs PHYSIK:	Prof. Dr. Michael Potthoff
Dekan der Fakultät MIN:	Prof. Dr. Heinrich Graener

Abstract

Single-pass high-gain free-electron lasers (FELs) are unique photon sources in the ultraviolet and x-ray spectral range which provide ultra-short pulses with unmatched brilliance. They are used by scientists of a wide variety of natural sciences. When starting from noise the longitudinal coherence properties of these pulses are limited. Providing a coherent input signal and, thus, seeding the FEL process allows to improve these properties and generate spectra which are comprised of a single peak.

The sFLASH experiment at FLASH is dedicated to the study of phase-space manipulating seeding techniques where the interaction of a seed laser and the electron beam is used to generate Fourier components in the current profile that start the FEL process. The High-Gain Harmonic Generation process at sFLASH at 38 nm – the 7th harmonic of the seed laser wavelength – has been thoroughly characterized and studied with available numerical simulation tools. The unique hardware arrangement at sFLASH enables the reconstruction of the pulse power profiles from the longitudinal phase space distribution of the electron bunch on a femtosecond scale. The same measurements can be used to estimate slice properties of the electron bunch and predict the seeded performance for different longitudinal laser-electron timings. This femtosecond characterization of the electron bunch supports a more reliable operation of soft x-ray seeded FEL facilities.

The experience gained from the sFLASH experiment and the benchmark of the used simulation tools facilitate the discussion of two design proposals for a seeded user facility at the FLASH2 undulator beamline. One upgrade option discussed is self-seeding where the output of a first undulator FEL stage traverses a monochromator and is used to directly seed a second stage. The second upgrade option studied aims to implement a seeding scheme similar to the sFLASH experiment at FLASH1. After the analysis of both options a brief discussion on benefits and drawbacks of both schemes is given.

Zusammenfassung

Stark verstärkende Freie-Elektronen-Laser (FELs) sind einzigartige Lichtquellen, die ultrakurze Photonenpulse mit unerreichter Brillianz im ultravioletten bis harten Röntgenbereich erzeugen. Sie werden von Wissenschaftlern aus einer Vielzahl verschiedener Naturwissenschaften genutzt.

Startet der FEL-Verstärkungsprozess aus dem Rauschen der Elektronenverteilung, so sind die erzeugten Lichtpulse nur begrenzt longitudinal kohärent. Wird dem FEL-Prozess jedoch beim sogenannten *Seeding* ein kohärentes Eingangssignal vorgegeben, kann die longitudinale Kohärenz des Lichtpulses kontrolliert werden. Die Einzelschussspektren dieser Pulse zeigen dann nur noch ein zentrales gaussförmiges Maximum.

Am experimentellen Testaufbau sFLASH, installiert an der FEL-Nutzeranlage FLASH bei DESY, werden phasenraummanipulierende *Seeding*-Methoden erforscht. Diese Methoden nutzen die Interaktion eines externen *Seed*-Lasers mit einem ultra-relativistischen Elektronenstrahl, um scharfe Spitzen im Stromprofil der Elektronen zu erzeugen, die den FEL-Prozess starten. In dieser Arbeit wird der *Seeding*-Prozess bei einer Abstrahlungswellenlänge von 38 nm – der siebten Harmonischen der *Seed*-Laser-Wellenlänge – charakterisiert und mit numerischen Simulationsprogrammen untersucht. Die einzigartige Anordnung des experimentlellen Aufbaus bei sFLASH ermöglicht eine zeitaufgelöste Rekonstruktion der Leistungsprofile der Photonenpulse. Dies geschieht durch die Analyse der mit einer Auflösung von einigen Femtosekunden gemessenen longitudinalen Phasenraumverteilung der Elektronpakete. Zusätzlich könenn aus diesen Messungen Zeitprofile der Eigenschaften des Elektronenpaketes abgeleitet werden. Dies erlaubt die Effizienz des *geseedeten* FEL-Prozesses für verschiedene Laser-Elektronen-Zeitabstimmungen vorauszusagen. Diese Charakterisierung auf der Femtosekundenskala ermöglicht einen zuverlässigeren Betrieb von *geseedeten* FEL-Anlagen im weichen Röntgenbereich.

Auf Basis der im sFLASH-Experiment gewonnenen Erfahrung werden zwei Vorschläge für eine *geseedete* Undulator-Strecke im Nutzerbetrieb bei FLASH2 diskutiert. Eine dieser Optionen ist das sogenannte *Self-Seeding*. Hier wird das Licht eines ersten Undulators durch einen Monochromator in seiner Bandbreite eingeschränkt, um anschließend den FEL-Prozess in einer folgenden Undulator-Strahlführung direkt zu *seeden*. Die zweite Erweiterungsoption, die untersucht wurde, zielt darauf ab, ein *Seeding*-Schema zu implementieren, welches dem bei sFLASH sehr ähnlich ist. Nach der Analyse beider Optionen folgt eine kurze Diskussion um die Vor- und Nachteile beider Schemata.

Contents

List of Figures

List of Publications

This thesis is based on the following publications:

Refereed Journal Articles

T. Plath, et al., *Mapping few-femtosecond slices of ultra-relativistic electron bunches*, Scientific Reports 7, DOI: 10.1038/s41598-017-02184-3 (2017)

Ph. Amstutz, **T. Plath**, et al., *Confining continuous manipulations of accelerator beamline optics*, Phys. Rev. Accel. Beams 20, 042802 (2017)

T. Plath, et al., *Free-Electron Laser Multiplex driven by a Superconducting Linear Accelerator*, J. Synchrotron Rad. 23, 1070-1075 (2016)

B. Faatz, ... , **T. Plath**, et al., *Simultaneous operation of two soft X-ray free-electron lasers driven by one linear accelerator*, New J Physics 18, 062002 (2016)

Conference Proceedings

K. Hacker, ..., **T. Plath**, et al., *First Lasing of an HGHG Seeded FEL at FLASH*, Proc. 37th International Free-Electron Laser Conference, Daejeon, Korea, 646 – 649 (2015)

G. Feng, ..., **T. Plath**, et al., *Seeded FEL Study for Cascaded HGHG Option for FLASH2*, Proc. 37th International Free-Electron Laser Conference, Daejeon, Korea, 246 – 250 (2015)

T. Plath, et al., *Influence of Laser Wavefront Imperfections on HGHG Seeding Performance*, Proc. 37th International Free-Electron Laser Conference, Daejeon, Korea, 643 – 645 (2015)

Ph. Amstutz, ..., **T. Plath**, et al., *Optics Compensation for Variable-gap Undulator Systems at FLASH*, Proc. 6th International Particle Accelerator Conference, Richmond, VA, USA, 1499 – 1501 (2015)

J. Bödewadt, ..., **T. Plath**, et al., *Recent Results from FEL Seeding at FLASH*, Proc. 6th International Particle Accelerator Conference, Richmond, VA, USA, 1366 – 1369 (2015)

T. Plath, et al., *Conceptual Study of Self-seeding Scheme at FLASH2*, Proc. 36th International Free-Electron Laser Conference, Basel, Schweiz, 53 – 57 (2014)

G. Feng, ..., **T. Plath**, et al., *Start-to-End Simulation for FLASH2 HGHG Option*, Proc. 36th International Free-Electron Laser Conference, Basel, Schweiz, 244 – 247 (2014)

N. Ekanayake, ..., **T. Plath**, *Indirect Measurements of NIR and UV Ultrashort Seed Laser Pulses using a Transverse Deflecting RF-Structure*, Proc. 36th International Free-Electron Laser Conference, Basel, Schweiz, 272 – 274 (2014)

1. Introduction

High-resolution imaging has always been an important tool to study dynamic processes or material structures in Physics and other natural sciences. In an attempt to resolve smaller structures, scientists need light of small wavelength with a sufficient number of photons. In a comparison of different radiation sources, the spectral brilliance $\mathcal{B}$ is often used to measure the performance. It does not only describe the photon flux in a certain spectral range, but is normalized to the angle the photons are emitted in and the source surface. Brilliance thus not only favors a high flux, but also a high phase-space density [1]. The brilliance or brightness $\mathcal{B}$ is defined as [2]

$$\mathcal{B}(\omega) = \frac{\Phi(\lambda)}{4\pi^2 \sigma_\mathrm{x}\sigma_\mathrm{y}\sigma'_\mathrm{x}\sigma'_\mathrm{y}}, \tag{1.1}$$

where $\Phi(\omega)$ is the photon flux within a relative spectral bandwidth of 0.1%, $\omega = 2\pi f$ is the angular frequency, σ_x and σ_y describe the transverse rms sizes of the source and σ'_x and σ'_y the respective opening angles of the radiation. Brilliance is thus measured in #photons/(s mm^2 mrad^2 0.1%BW). Most photon experiments require a high photon count of nearly monochromatic light that can be focused down onto a sample and, thus, demand a high brilliance.

One source of radiation that shows a high brilliance even at small wavelengths are charged particles, e.g. electrons. The radiation emitted by electric charges accelerated to highly relativistic energies is called synchrotron radiation and has first been observed in 1947 at the General Electric Laboratories [3]. Even though synchrotron radiation shows a broad spectrum, it provides a high brilliance over many orders of magnitude of wavelengths [2]. These favorable characteristics lead to wide usage of synchrotron radiation as a tool for high-resolution imaging based on acceleration of charged particles. The light sources employing these techniques can be classified in generations [1]:

First generation light sources are electron storage rings built for nuclear physics which have been parasitically used to generate synchrotron radiation. These facilities have shown the appeal of the radiation which soon led to the construction of the first *second generation* sources: Accelerators dedicated and optimized to the generation of synchrotron radiation in their bending magnets, e.g. BESSY I commissioned in 1981 [4]. The usage of insertion devices such as undulators and wigglers that are magnet arrangements dedicated to generate radiation in combination with a reduced emittance enabled the construction of the first *third generation* light sources like BESSY II commissioned in 1997 [5].

In current third-generation machines, the electrons circulate millions of times per second and every time they traverse the insertion devices radiation is generated. In contrast, the approach for *fourth generation* light sources is to build single-pass or few-pass machines with significantly shorter electron bunches that have a high peak current and low emittance. These machines can generate highly brilliant photon pulses with durations of tens of femtoseconds or even less. One example for these kind of machines are high-gain Free-Electron Lasers (FELs). FELs are comprised of a linear accelerator followed by a long undulator allowing the generated light to couple back to the electron bunch and to rearrange the particles into micro-bunches. These electrons are then able to radiate coherently, enhancing the photon flux by 4 to 8 orders of magnitude compared to *third generation* light sources. Figure 1.1 shows the peak brilliance of different accelerator based light sources. As can be seen from the figure, there is a gap of several orders of magnitude between Free-Electron lasers and third generation light sources.

The startup of the FEL is driven by statistical processes. Thus, the characteristics of the generated photon pulses can vary from shot to shot. One approach to overcome these limitations is to introduce well-defined starting conditions and thus seed the FEL process with an initial light field or electron bunching. The FEL will now merely act as an amplifier for this signal and the final pulse properties will be determined by the seed signal. The seeding experiment sFLASH at the Free-Electron Laser FLASH at DESY in Hamburg is dedicated to the study of this seeding process.

In this thesis, the realization of the phase-space manipulating high-gain harmonic generation seeding scheme is presented along with experimental results and detailed analysis of the FEL process. Due to the unique hardware arrangement at FLASH, it was possible to analyze the longitudinal phase-space distribution of the electron bunch after FEL lasing has occured and extract FEL pulse profiles from the energy loss of the participating electrons. This enables a simple derivation of slice parameters from single-shot measurements of the phase space distribution. The seeding process can serve as a local probe to verify theoretical predictions and allows to find information on the initial conditions imprinted by the seed laser. The second part of the thesis focuses on theoretical considerations for a dedicated seeding setup at the second undulator beamline at FLASH. Two seeding schemes are studied regarding their feasibility and generated photon pulse characteristics.

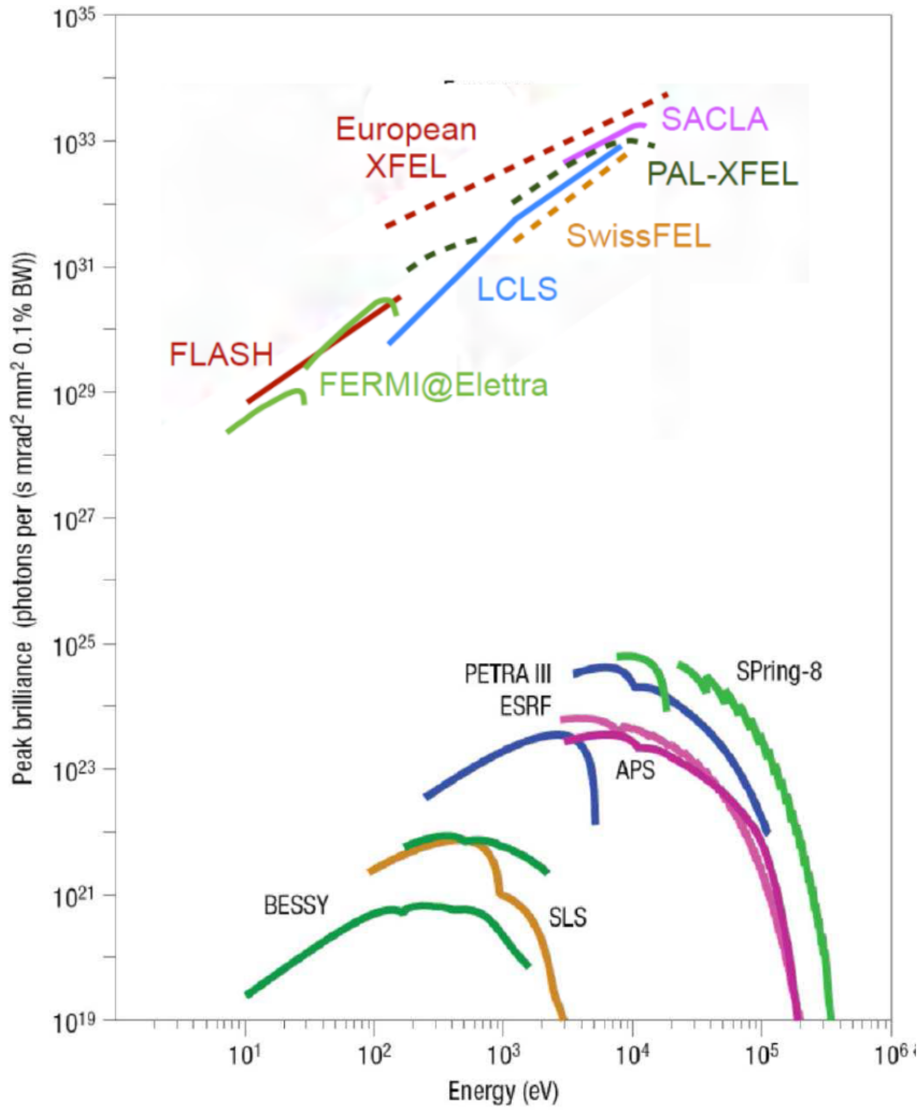

Figure 1.1.: Peak brilliance as a function of photon energy of different accelerator based photon sources. The lower batch are second and third generation electron storage rings. The higher brilliance machines are Free-Electron Lasers that have a brilliance several orders of magnitudes higher. Dashed lines indicate facilities that are currently under construction. Courtesy S. Ackermann, M. Tischer.

2. An Introduction to Free-Electron Lasers

Free-Electron Lasers (FELs) were first described by John M. J. Madey in 1971 [6] and experimentally demonstrated by his group in the 1970s at a wavelength of 10.6 µm [7]. Nowadays, FELs generate high-intensity light pulses from the infrared down to hard x-ray spectral range that are used by a wide variety of sciences to probe microscopic systems. The following descriptions of FEL theory closely follow the ones in [8] and [9], if not stated otherwise.

The radiation of an FEL is generated by deflecting relativistic electron bunches traversing a structure of periodically alternating dipole magnets called undulator. When the electrons stay in overlap with the generated radiation, the light field couples back to the electrons and modulates their energy at a wavelength of the emitted light. Due to the dispersive character of the undulator, the electrons get a longitudinal displacement that is proportional to their energy deviation. This leads to a current modulation on the light wavelength called microbunching. The microbunched electrons can radiate coherently, since – compared to the light wavelength – they are at the same longitudinal position. The coherent radiation process results in the characteristic exponential power gain of the FEL process.

The movement of the electrons within the undulator system is a crucial ingredient for the FEL process. Permanent-magnet undulators are the most common and usually have periods λ_u of a couple of cm. It is known from basic electrodynamic that electric charges which are accelerated emit light which is called synchrotron radiation [10]. If they are moving through a bending magnet, the radiation is known to have a wide spectrum up to a frequency called critical frequency $\omega_\mathrm{c} = \frac{3c\gamma^3}{2R}$, where c is the speed of light in vacuum, R the bending radius and γ is the relativistic Lorentz factor

$$\gamma = \frac{1}{\sqrt{1 - \left(\frac{v}{c}\right)^2}} = \frac{W}{m_\mathrm{e}c^2}. \tag{2.1}$$

Here, m_e is the rest mass of the electron, v its velocity and W the total relativistic energy of the electron. The power $P \propto \gamma^4/R^2$ is concentrated in an opening angle of $1/\gamma$ centered around the tangent to the circular motion at the moment of emission. Note that quantities and equations throughout this thesis are given in SI units.

To characterize the properties of this radiation generated by a series of bending magnets with alternating polarity, we have to take a closer look at the trajectory of the electron when traversing the undulator. Let B_0 be the magnetic peak field on the axis between the magnetic yokes. Then, by assuming a simplified alternating magnetic field of the undulator $B_\mathrm{y}(z) = B_0 \sin(k_\mathrm{u} z)$, where $k_\mathrm{u} = 2\pi/\lambda_\mathrm{u}$, we can derive the velocity vector $\mathbf{v}$ of an electron experiencing the Lorentz force to be [8]

$$\mathbf{v} = \begin{pmatrix} v_\mathrm{x} \\ v_\mathrm{y} \\ v_\mathrm{z} \end{pmatrix} = \begin{pmatrix} \frac{Kc}{\gamma}\cos(k_\mathrm{u} z) \\ 0 \\ \bar{\beta} c \end{pmatrix}, \qquad \bar{\beta} = \left(1 - \frac{1}{2\gamma^2}\left(1 + \frac{K^2}{2}\right)\right). \tag{2.2}$$

Here, $K = \frac{eB_0}{m_\mathrm{e} c k_\mathrm{u}}$ denotes the dimensionless undulator parameter, e is the elementary charge, and m_e the electron rest mass. The undulator parameter can be obtained in practical units by inserting all physical constants:

$$K = \frac{eB_0}{m_\mathrm{e} c k_\mathrm{u}} = 0.934 \cdot B_0[\mathrm{T}] \cdot \lambda_\mathrm{u}[\mathrm{cm}]. \tag{2.3}$$

In its rest frame the electron traversing the undulator performs harmonic oscillations in the x-z-plane. The frequency ω^* for the transverse oscillation is given by

$$\omega^* \approx \frac{\gamma c k_\mathrm{u}}{\sqrt{1 + K^2/2}}. \tag{2.4}$$

The longitudinal motion has a by far smaller amplitude and oscillates with twice the frequency. For the time being, the latter oscillation will be ignored. When transforming the frequency of the transverse oscillation back to the laboratory frame we get the central wavelength of the undulator radiation

$$\lambda_\mathrm{l} = \frac{\lambda_\mathrm{u}}{2\gamma^2}\left(1 + \frac{K^2}{2} + \gamma^2\theta^2\right), \tag{2.5}$$

where θ is the angle of emission with respect to the direction of electron movement. The spectrum of this spontaneous undulator radiation follows a characteristic sinc^2 function with a full width at half maximum (fwhm) of $\Delta\omega = \omega_\mathrm{l}/N_\mathrm{u}$, where N_u is the number of undulator periods traversed and $\omega_\mathrm{l} = 2\pi c/\lambda_\mathrm{l}$.

For an FEL, as described earlier, the generated light has to stay in overlap with the electron bunch in order for the electrons to couple back to the light field.

2.1. Low-Gain FEL

In the presence of an electric field, the electron energy W will change according to the Lorentz force. Assuming an initial electric field with only an x-component $E_\mathrm{x} = E_0 \cos(k_\mathrm{l} z - \omega_\mathrm{l} t + \phi_0)$ the derivative of the electron energy becomes

$$\begin{aligned} \frac{\mathrm{d}W}{\mathrm{d}t} = m_\mathrm{e} c^2 \frac{\mathrm{d}\gamma}{\mathrm{d}t} &= -e v_\mathrm{x} E_\mathrm{x} \\ &= -\frac{eE_0 Kc}{2\gamma}\{\cos[(k_\mathrm{l} + k_\mathrm{u})z - \omega_\mathrm{l} t + \phi_0] + \cos[(k_\mathrm{l} - k_\mathrm{u})z - \omega_\mathrm{l} t + \phi_0]\} \\ &= -\frac{eE_0 Kc}{2\gamma}\{\cos\Psi + \cos\chi\}, \end{aligned} \tag{2.6}$$

where ϕ_0 is an arbitrary phase between the sinusoidal trajectory of the electron and the light, k_u the wave number of the undulator, k_l and ω_l are the wave number and angular frequency of the light. Also introduced in the equation are the phases Ψ and χ, containing $(k_\mathrm{l} + k_\mathrm{u})$ and $(k_\mathrm{l} - k_\mathrm{u})$ respectively. To ensure a net energy transfer from the electrons to the electric field, the phase terms have to be constant.

Looking at the first term of Eq. (2.6), the condition for the ponderomotive phase Ψ to be constant leads to

$$\frac{\mathrm{d}\Psi}{\mathrm{d}t} = (k_\mathrm{l} + k_\mathrm{u})\frac{\mathrm{d}z(t)}{\mathrm{d}t} - k_\mathrm{l}c = 0, \tag{2.7}$$

where $\frac{\mathrm{d}z(t)}{\mathrm{d}t} = v_\mathrm{z}$. For the approximation that $\bar{\beta} \approx 1$, we can expand this expression to obtain the resonance condition of the FEL process for sustained energy transfer

$$\lambda_\mathrm{l} = \frac{\lambda_\mathrm{u}}{2\gamma^2}\left(1 + \frac{K^2}{2}\right). \tag{2.8}$$

The resonance condition has the same form as the central wavelength of the undulator radiation on-axis leading to the fact, that the FEL can be efficiently started from spontaneous undulator radiation.

Note that the condition (2.7) is equivalent to the requirement that the path lengths difference between electrons and light propagating through one undulator period $lambda_\mathrm{u}$ is exactly one light wavelength λ_l. In other words, the resonance condition ensures that the slippage between light field and electrons per undulator period is always one light wavelength which provides a constant net energy transfer from the electrons to the electric field.

The second term in Eq. (2.6), however, cannot be kept constant, since a similar analysis to the one for Ψ leads to negative wave numbers of the light wave, which is physically impossible. When rewriting the argument of the cosine function, we can observe that it oscillates twice per undulator period

$$\chi(z) = \Psi(z) - 2k_\mathrm{u}z. \tag{2.9}$$

This part can thus be neglected, since the net energy transfer in an undulator period is zero. The remaining part of Eq. (2.6) gives the first of the FEL pendulum equations that relates the energy change of the electrons with the ponderomotive phase:

$$\frac{\mathrm{d}W}{\mathrm{d}t} = -\frac{eE_0Kc}{2\gamma}\cos\Psi \tag{2.10}$$

As can be seen from the equation, the ponderomotive phase determines the direction of the energy transfer between electrons on light. Since Ψ is constant along the propagation of the electron beam the initial choice of ϕ_0 determines if the energy change is positive or negative.

For further description of the process, we introduce the electron resonance energy γ_r. It is the energy of an electron that emits light on the wavelength of the initial field under the resonance condition Eq. (2.8). We can now define the relative energy deviation

$$\eta = \frac{\gamma - \gamma_\mathrm{r}}{\gamma_\mathrm{r}}, \tag{2.11}$$

and rewrite the equation for the energy transfer

$$\frac{\mathrm{d}\eta}{\mathrm{d}t} = -\frac{eE_0K}{2\gamma_\mathrm{r}^2 m_\mathrm{e} c}\cos\Psi \tag{2.12}$$

When taking electrons into account with a non-zero energy deviation their ponderomotive phase is no longer constant. Starting from the left part of Eq. (2.7) and inserting the velocity of the electrons from Eq. (2.2) we end up with

$$\frac{\mathrm{d}\Psi}{\mathrm{d}t} = k_\mathrm{u}c - \frac{k_\mathrm{l}c}{2\gamma^2}\left(1+\frac{K^2}{2}\right). \tag{2.13}$$

With $k_\mathrm{u}c$ being replaced using the resonance condition this becomes

$$\frac{\mathrm{d}\Psi}{\mathrm{d}t} = \frac{k_\mathrm{l}c}{2}\left(1+\frac{K^2}{2}\right)\left(\frac{1}{\gamma_\mathrm{r}^2}-\frac{1}{\gamma^2}\right). \tag{2.14}$$

When we expand the right side of this equation for small energy deviations from γ_r ($\eta << 1$) and rewrite Eq. (2.12) we get a system of coupled differential equations called the FEL pendulum equations:

$$\frac{\mathrm{d}\Psi}{\mathrm{d}t} = 2k_\mathrm{u}c\eta(t) \tag{2.15}$$

$$\frac{\mathrm{d}\eta}{\mathrm{d}t} = -\frac{eE_0K}{2m_\mathrm{e}c\gamma_\mathrm{r}^2}\cos\Psi(t) \tag{2.16}$$

Note that these considerations do not allow the initial electric field to change its amplitude E_0 significantly while passing through the undulator since we did not consider any dependence of E_0 on t. The pendulum equations describe the motion of an electron in the Ψ - η phase space. Fig. 2.1 shows the numerical solution of the equation system (2.15) and (2.16). The figure also shows the separatrix of an FEL bucket that isolates the regions of bound and unbound motion.

From Fig. 2.1a, one can see that there will be no energy gain of the light field if all electrons are injected on resonance. If the electrons however are injected with a small positive energy detuning there is more energy loss than gain in the ensemble and the light field will experience a net intensity gain. The intensity gain G of the low-gain FEL is described as a function of the detuning parameter by the Madey Theorem:

$$G(\xi) \propto \frac{\mathrm{d}}{\mathrm{d}\xi}\left(\frac{\sin^2\xi}{\xi^2}\right), \tag{2.17}$$

where $\xi = 2\pi N_\mathrm{u}\eta$, with N_u being the number of undulator periods traversed by the electron bunch. The maximum gain of the low-gain FEL is thus not at the resonance energy, but for a positive detuning.

Correction of Undulator Parameter

Since an undulator not only radiates light on its fundamental, but also on odd harmonics, the coupling of the electrons to the light field is not completely described by the model

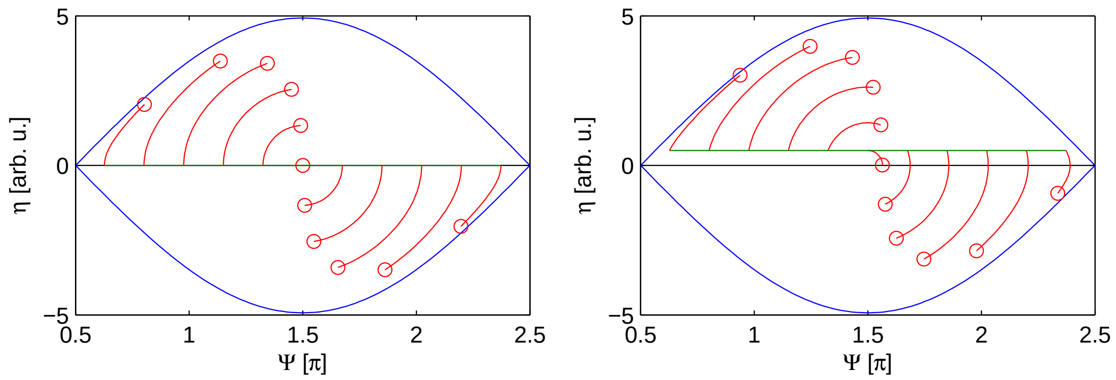

(a) on resonance (b) positive detuning

Figure 2.1.: Movement of electrons taking part in the FEL process in phase space. The blue line is the seperatrix that confines the bound from unbound states. The red line shows the movement of electrons starting with equally distributed phases. The electrons in (a) are injected on resonance, while the electrons in (b) have a small positive detuning.

above. For planar undulators this changes the coupling of the electrons and the fundamental. To incorporate this effect into the model described above, the undulator parameter in Eq. (2.15) and (2.16) has to be substituted by the modified parameter

$$K_{\mathrm{JJ}} = K\left[J_0\left(\frac{K^2}{4+2K^2}\right) - J_1\left(\frac{K^2}{4+2K^2}\right)\right] \tag{2.18}$$

Here, J_0 and J_1 are the Bessel functions of zeroth and first order, respectively.

2.2. One Dimensional Theory of High-Gain FEL

To achieve high output powers from the low-gain FEL process the light is amplified by multiple electron bunches while it oscillates in an optical cavity. Mirrors are set up with a distance of a couple of meters, surrounding the undulator magnets, and the power of the FEL pulse is amplified by a new electron bunch in each cycle.

However, since no mirrors are available for small wavelengths ranges, FELs in the XUV and X-ray range are usually built as single-pass machines. The electron bunch current is high enough for the FEL process to generate powers in the Gigawatt range within just a single pass through a couple of tens of meters of undulator. In this regime, the low-gain FEL theory no longer applies since the amplitude of the electric field changes significantly while the electrons traverse the undulator. Furthermore, the initial electric field now takes a complex form for simplicity of the mathematics. The new ansatz for $\tilde{E}_{\mathrm{x}}$ thus is

$$\tilde{E}_{\mathrm{x}}(z,t) = \tilde{E}_{\mathrm{x}}(z)\exp[i(k_{\mathrm{l}}z - \omega_{\mathrm{l}}t)], \tag{2.19}$$

where the tilde denotes complex quantities and $\tilde{E}_{\mathrm{x}}(z)$ denotes the z-dependent amplitude function. The real electric field is just described by the real part of this equation.

One of the driving mechanisms of an FEL is the microbunching process. Electrons interacting with the electric field will get a sinusodial modulation on the light wavelength. Since the undulator is a series of dipoles it has dispersive characteristics. Higher energy electrons fall back while lower energy electrons catch up leading to the formation of microbunches which have the periodicity of the light wavelength. These microbunches are able to radiate coherently since they are much shorter than the wavelength. From this periodicity we can express a periodicity in the ponderomotive phase and we can write the current density as

$$\tilde{j}_{\mathrm{z}}(\Psi, z) = j_0 + \tilde{j}_1(z)\exp[i\Psi]. \tag{2.20}$$

The evolution of the field amplitude can be derived, starting with the wave equation

$$\left[\nabla^2 - \frac{1}{c^2}\frac{\partial^2}{\partial t^2}\right]\tilde{E}_{\mathrm{x}}(z,t) = \mu_0 \frac{\partial \tilde{j}_{\mathrm{x}}}{\partial t} + \underbrace{\frac{1}{\epsilon_0}\frac{\partial \tilde{\rho}_{\mathrm{x}}}{\partial x}}_{=0}, \tag{2.21}$$

where μ_0 is the vacuum permeability constant and $\tilde{\rho}$ is the charge density of the electron bunch. The last term vanishes, since the only dependence of $\tilde{\rho}$ we assume in one-dimensional theory is a longitudinal one. The term with $\tilde{j}_{\mathrm{x}}$ describes the sinusoidal trajectory of the electrons through the undulator as a source term for the evolution of the electric field. If we plug Eq. (2.19) into the wave equation we get

$$\left[2ik_{\mathrm{l}}\frac{\mathrm{d}\tilde{E}_{\mathrm{x}}}{\mathrm{d}z} + \frac{\mathrm{d}^2\tilde{E}_{\mathrm{x}}}{\mathrm{d}z^2}\right]\exp[i(k_{\mathrm{l}}z - \omega_{\mathrm{l}}t)] = \mu_0\frac{\partial \tilde{j}_{\mathrm{x}}}{\partial t}. \tag{2.22}$$

To further simplify the equation, it is useful to neglect the second order derivative in the scope of the so called slowly varying amplitude (SVA) approximation. It states that $\tilde{E}_{\mathrm{x}}$ is a smooth function and only experiences small changes over one undulator period and that the second derivative with respect to z can be neglected compared to the first derivative. Additionally, one can relate the transverse current density $\tilde{j}_{\mathrm{x}}$ to the longitudinal one leading to

$$\frac{\mathrm{d}\tilde{E}_{\mathrm{x}}}{\mathrm{d}z} = \frac{\mu_0 c K_{\mathrm{JJ}}}{4\gamma}\tilde{j}_1. \tag{2.23}$$

The microbunches that form under the influence of the light field are a periodic disturbance of the electron charge density. This modulation causes an inhomogeneous longitudinal space charge field $\tilde{E}_{\mathrm{z}}$ that can be calculated from the charge density by applying the first Maxwell equation:

$$\tilde{E}_{\mathrm{z}}(z) \approx -\frac{i\mu_0 c^2}{\omega_{\mathrm{l}}}\cdot\tilde{j}_1(z). \tag{2.24}$$

This electric field will induce an energy change of the electrons that has to be added to Eq. (2.16). With $z = \bar{v}_{\mathrm{z}}t$ the combined equation for both effects then yields

$$\frac{\mathrm{d}\eta}{\mathrm{d}z} = -\frac{e}{m_{\mathrm{e}}c^2\gamma_{\mathrm{r}}}\Re\left[\left(\frac{K\tilde{E}_{\mathrm{x}}}{2\gamma_{\mathrm{r}}} + \tilde{E}_{\mathrm{z}}\right)\exp\left(i\phi\right)\right]. \tag{2.25}$$

An expression for $\tilde{j}_1$ can be found by expanding the longitudinal electron distribution into a Fourier series. Together with Eq. (2.15), (2.23) and (2.25), this expression gives the complete set of coupled first-order equations in a periodic model of the electron bunch:

$$\frac{\mathrm{d}\Psi_\mathrm{n}}{\mathrm{d}z} = 2k_\mathrm{u}\eta_\mathrm{n}, \tag{2.26}$$

$$\frac{\mathrm{d}\eta_\mathrm{n}}{\mathrm{d}z} = -\frac{e}{m_\mathrm{e}c^2\gamma_\mathrm{r}}\Re\left[\left(\frac{K_\mathrm{JJ}\bar{E}_\mathrm{x}}{2\gamma_\mathrm{r}} - \frac{i\mu_0c^2}{\omega_\mathrm{l}}\cdot\tilde{j}_1\right)\exp\left(i\Psi_\mathrm{n}\right)\right], \tag{2.27}$$

$$\tilde{j}_1 = j_0\frac{2}{N}\sum_{\mathrm{n}=1}^{N}\exp\left(i\Psi_\mathrm{n}\right) \tag{2.28}$$

$$\frac{\mathrm{d}\tilde{E}_\mathrm{x}}{\mathrm{d}z} = -\frac{\mu_0cK_\mathrm{JJ}}{4\gamma_\mathrm{r}}\cdot\tilde{j}_1, \tag{2.29}$$

where the subscript n denotes parameters for the nth electron ($n = 1...N$). Here, we again corrected the undulator parameter K with K_JJ. Since electron bunches used for generation of FEL radiation usually carry charges of tens to hundreds of picocoulomb and thus a number of electrons that can exceed 10^9, this system of equations cannot be solved analytically but must be solved by numerical integration.

Under the assumption of small periodic density modulation, the single-particle coordinates Ψ_n and η_n can be eliminated from the above system of coupled differential equations, leaving only one third-order differential equation for the electric field amplitude $\tilde{E}_\mathrm{x}$ [11].

$$\frac{\tilde{E}_\mathrm{x}'''}{\Gamma^3} + 2i\frac{\eta}{\rho_\mathrm{FEL}}\frac{\tilde{E}_\mathrm{x}''}{\Gamma^2} + \left(\frac{k_\mathrm{p}^2}{\Gamma^2} - \left(\frac{\eta}{\rho_\mathrm{FEL}}\right)^2\right)\frac{\tilde{E}_\mathrm{x}'}{\Gamma} - i\tilde{E}_\mathrm{x} = 0 \tag{2.30}$$

Here, the primed quantities are absolute derivatives with respect to z. We introduced the gain parameter Γ and the space-charge parameter k_p [11]

$$\Gamma = \left[\frac{\mu_0K_\mathrm{JJ}^2e^2k_\mathrm{u}n_\mathrm{e}}{4\gamma_\mathrm{r}^3m_\mathrm{e}}\right]^{\frac{1}{3}} \tag{2.31}$$

$$k_\mathrm{p} = \sqrt{2\lambda_\mathrm{l}}\lambda_\mathrm{u}\frac{\omega_\mathrm{p}^*}{c}, \tag{2.32}$$

where n_e is the particle density, $\omega_\mathrm{p}^* = \sqrt{\frac{n_\mathrm{e}e^2}{\gamma_\mathrm{r}\epsilon_0m_\mathrm{e}}}$ the plasma frequency and ϵ_0 the vacuum permittivity constant. We also introduced a new quantity called the Pierce parameter [12]

$$\rho_\mathrm{FEL} = \frac{\Gamma}{2k_\mathrm{u}} = \frac{1}{4\pi\sqrt{3}}\frac{\lambda_\mathrm{u}}{L_\mathrm{g0}}, \tag{2.33}$$

which is a central parameter for the FEL process. The power gain length L_g0 is defined when solving the third-order differential equation. The complete solution, however, has to be found with a certain set of initial conditions, as for every differential equation. While there are many ways to start the FEL process, the following solution will focus on an initial monochromatic light field of the form $E_\mathrm{x}(z,t) = E_\mathrm{in}\cos(k_\mathrm{l}z - \omega_\mathrm{l}t)$ with $k_\mathrm{l} = \omega_\mathrm{l}/c = 2\pi/\lambda_\mathrm{l}$. The evolution of this initial light field can now be studied using the third-order differential equation (2.30). The solution for an on resonance beam ($\eta = 0$) with neglected space-charge parameter ($k_\mathrm{p} = 0$) is given by

$$\tilde{E}_\mathrm{z}(z) = \frac{E_\mathrm{in}}{3}\left[\exp\left((i+\sqrt{3})\Gamma z/2\right) + \exp\left((i-\sqrt{3})\Gamma z/2\right) + \exp(-i\Gamma z)\right]. \tag{2.34}$$

After a certain distance the first term in the brackets will dominate the process. Since $P(z) \propto |\tilde{E}_\mathrm{z}|^2$ we can write the exponential power growth after 2 gain lengths L_g

$$P(z) \simeq \frac{P_\mathrm{in}}{9}\exp(z/L_\mathrm{g0}) \qquad\qquad \text{for } z \geq 2\,L_\mathrm{g0}, \tag{2.35}$$

where P_in is the power of the initial monochromatic light field. We use the gain length L_g0 as defining parameter for the exponential gain. It is given by

$$L_\mathrm{g0} = \frac{1}{\sqrt{3}\Gamma} = \frac{1}{\sqrt{3}}\left[\frac{4\gamma_\mathrm{r}^3 m_\mathrm{e}}{\mu_0 K_\mathrm{JJ}^2 e^2 k_\mathrm{u} n_\mathrm{e}}\right]^{1/3}. \tag{2.36}$$

The space-charge parameter can be neglected for FELs radiating at small wavelengths and high-electron energies. For FLASH, this approximation holds. Neglecting the space-charge parameter only decreases the one-dimensional gain length by 1% [13].

2.3. Analytical Estimation – Ming-Xie formula

The three-dimensional treatment of the FEL process is quite complex and often numerical simulations are the only tool available to make quantitative statements on FEL performance. Ming Xie, however, developed a fitting formula that enables a quick calculation of the three-dimensional gain length of the FEL process [14]. In this formalism a fitting formula was derived that scales the one-dimensional gain length to three dimensions:

$$\frac{L_\mathrm{g0}}{L_\mathrm{g}} = \frac{1}{1+\Lambda}, \tag{2.37}$$

where L_g0 denotes the one-dimensional gain length and L_g the three-dimensional estimation. Λ is the scaling function that depends on the diffraction parameter η_d, as well as η_ϵ and η_γ that characterize the effective spread in longitudinal velocity due to emittance and energy spread.

$$\eta_\mathrm{d} = \frac{1}{4\pi}\frac{\lambda_\mathrm{l} L_\mathrm{g0}}{\sigma_\mathrm{r}^2} \tag{2.38}$$

$$\eta_\epsilon = 4\pi\frac{\epsilon L_\mathrm{g0}}{\beta_\mathrm{avg}\lambda_\mathrm{l}} \tag{2.39}$$

$$\eta_\gamma = 4\pi\frac{\sigma_\gamma L_\mathrm{g0}}{\gamma_\mathrm{r}\lambda_\mathrm{u}} \tag{2.40}$$

Here σ_r is the transverse rms size of the electron beam, ϵ is its transverse emittance. β_avg is the average beta function along the undulator and σ_γ the rms energy spread in multiples of the electron rest mass. The scaling function Λ is then given by

$$\Lambda = a_1\eta_d^{a_2} + a_3\eta_\epsilon^{a_4} + a_5\eta_\gamma^{a_6} + a_7\eta_\epsilon^{a_8}\eta_\gamma^{a_9} + a_{10}\eta_d^{a_{11}}\eta_\gamma^{a_{12}} + a_{13}\eta_d^{a_{14}}\eta_\epsilon^{a_{15}} + a_{16}\eta_d^{a_{17}}\eta_\epsilon^{a_{18}}\eta_\gamma^{a_{19}}. \tag{2.41}$$

The coefficients a_1 to a_{19} are fitted numerical constants that are given in [14]. Λ is always positive and the three-dimensional gain length, thus, always bigger than the one-dimensional. In a very similar way the saturation power has been scaled to the three-dimensional case [15]:

$$P_{\mathrm{sat}} = 1.6\rho \left(\frac{L_{\mathrm{g0}}}{L_{\mathrm{g}}} \right)^2 P_{\mathrm{beam}}, \tag{2.42}$$

where $P_{\mathrm{beam}} = W_0 \cdot I/e$ is the instantaneous power of the electron beam and I its current.

Emittance

One scaling parameter used by the Ming-Xie model is the transverse emittance ϵ of the electron bunch. Multiplied by π it is a measure of the area that the electron beam distribution occupies in the respective transverse phase space (e.g. x, $x' = p_{\mathrm{x}}/p_0$). Here, p_{x} is the x-component of the particle momentum and p_0 is its total momentum [2].

To define an invariant that also stays constant during acceleration of the electron beam, often the normalized emittance is referenced. It is defined by

$$\epsilon_{\mathrm{n}} = \beta\gamma\epsilon \approx \gamma\epsilon, \tag{2.43}$$

where β is the electron velocity in multiples of the speed of light and γ is the relativistic Lorentz factor. Note that the last approximation only holds, if the electrons move with a velocity close to the speed of light. With the exception of the Ming-Xie model presented above that references the non-normalized emittance ϵ, the remaining parts of this thesis will usually refer to the normalized emittance ϵ_{n}.

Another important note is that the emittance can be directly related to the beam size by $\epsilon_{\mathrm{x}} = \sigma_{\mathrm{x}}^2/\beta_{\mathrm{x}}$, where σ_{x} is the rms beam size in the x-plane and β_{x} is the optical β-function of the accelerator [2].

2.4. Self-Amplified Spontaneous Emission

Above, the third-order differential equation for $\tilde{E}_{\mathrm{x}}$ has been solved for the initial condition of a monochromatic incoming light wave, often referred to as the seed. For a high-gain FEL like FLASH that operates in the extreme ultra-violet range, the generation of these seed pulses is very challenging. Fortunately as stated above, the spontaneous undulator radiation can start the FEL process since its central wavelength is the one fulfilling the FEL resonance conditions. This mode of operation is called self-amplified spontaneous emission (SASE) first considered by Derbenev, Kondratenko and Saldin [11, 16]. In this mode, the FEL process is started from inhomogeneities of the electron bunch called shot-noise.

This process can be understood from two different approaches that explain the same physical phenomenon: (i) The electron beam generates spontaneous undulator radiation in the first periods of a long undulator magnet that then seeds the FEL process very similar to the process studied above. (ii) Since an electron bunch carries a lot of randomly distributed particles, a white noise spectrum is generated in the current distribution. The FEL process can then start from spectral components within the FEL bandwidth.

To quantify the shot-noise, one can define a shot-noise equivalent electrical field amplitude E_{eq}. This is the amplitude of a monochromatic seeded beam that will lead to the same exponential behavior after a couple of gain lengths. It is given by

$$E_{\text{eq}} = \frac{\mu_0 c K_{\text{JJ}}}{4\gamma_{\text{r}}\Gamma}\sqrt{\frac{eI_0\Delta\omega}{\pi A_{\text{b}}^2}}, \tag{2.44}$$

where I_0 is the direct current of the electron bunch, $\Delta\omega$ is the bandwidth of the FEL, and A_{b} the beam cross section. The electrical field of an initial seed has to significantly exceed this shot-noise equivalent in order for the seed to determine the characteristics of the final FEL pulse. For an FEL process started from noise, the saturation length L_{sat} amounts to

$$L_{\text{sat}} \approx 4\pi\sqrt{3}L_{\text{g0}} = 21.8L_{\text{g0}}. \tag{2.45}$$

When starting from noise, no input signal is available that provides full longitudinal coherence. Instead the longitudinal coherence is only given over a time called coherence time τ_{coh} that can be estimated to be

$$\tau_{\text{coh}} \approx \frac{\pi}{\sigma_\omega}, \tag{2.46}$$

where $\sigma_\omega(z) = 3\sqrt{2}\rho_{\text{FEL}}\omega_{\text{l}}\sqrt{L_{\text{g0}}/z}$ is the rms power bandwidth. When considering a flat-top bunch of the length T_{bunch} the number of coherently radiating parts of the bunch amounts to

$$M = \frac{T_{\text{bunch}}}{\tau_{\text{coh}}}. \tag{2.47}$$

Each of these regions is considered a longitudinal mode and gives, on average, a spike in the SASE frequency spectrum. The characteristic width of the spike is, for a flat-top bunch, given by

$$\Delta\omega_{\text{spike}} = \frac{2\sqrt{2\ln 2}}{T_{\text{bunch}}}. \tag{2.48}$$

Each of these coherently radiating parts of the electron bunch will have a fluctuation in generated pulse energy U_{SASE}, since the electron distribution is subject to randomness. The probability distribution of the pulse energy per pulse is given by the Gamma distribution [17, 18]

$$p_{\text{M}}(u) = \frac{M^M}{\Gamma_{\text{f}}(M)}u^{M-1}\frac{1}{\langle U_{\text{SASE}}\rangle}\exp(-uM), \tag{2.49}$$

where $u = U_{\text{SASE}}/\langle U_{\text{SASE}}\rangle$, and $\langle U_{\text{SASE}}\rangle$ is the average photon pulse energy. Γ_{f} denotes the Gamma function. Note that this distribution holds for electron bunches that excite more than one longitudinal mode. The operation of a free electron laser where $T_{\text{bunch}} < \tau_{\text{coh}}$ has a different pulse energy statistic and generates a fully coherent wave packet, even when starting from noise.

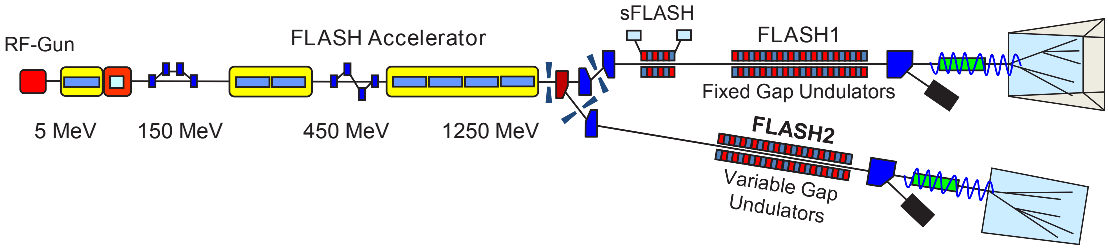

Figure 2.2.: Schematic overview of the FLASH facility. The radio-frequency (rf) gun on the left emits electrons that are accelerated by the yellow rf cavities. Downstream of the accelerator the electron bunch can be distributed to FLASH1 or FLASH2. Both undulator beamlines have their own dedicated photon user end stations.

2.5. FLASH – A SASE FEL User Facility

From the first theoretical discussion of the startup from noise it took almost 20 years until the first single-pass high-gain FEL SASE operation at 12 µm [19]. This experimental breakthrough was soon followed by the first Free-Electron Laser in the visible (530 nm) and ultra-violet range (385 nm), starting from noise and reaching saturation, at the low-energy undulator test line (LEUTL) at the Argonne National Laboratory in 2000 [20]. The Tesla Test Facility (TTF) reported saturation at 109 nm in 2001 [21] and down to 4 nm after being upgraded to the SASE FEL user facility FLASH in 2007 [22].

Today's SASE FELs reach down to several tenth of nm in case of LCLS in Stanford or SACLA at SPring-8 [23]. FLASH, however, is the only FEL facility yet that uses a superconducting linear accelerator enabling the generation of bunch trains with a repetition rate of 1 MHz within the train. Since 2005, FLASH has been operating as a user facility delivering high-brilliance extreme ultra-violet (XUV) and soft X-ray radiation from 4.2 nm to 52 nm wavelength to experiments with pulse energies up to several hundreds of microjoule. In 2011, construction for a second undulator beamline, FLASH2, started which was comissioned in 2014 and is also in user operation today. This second parallel beamline covers a similar parameter range as FLASH1, with up to 90 nm in the long-wavelength limit [24, 25].

In this section, the essential parts of the FLASH accelerator and undulator beamlines will be described. Figure 2.2 shows an overview of the FLASH facility, including the linear accelerator and the two parallel undulator beamlines. A description of the seeding hardware will be given in the next chapter.

2.5.1. Photo-Injector

The electron bunches at FLASH are emitted from a Cesium Telluride (Cs_2Te) cathode when it is hit by an ultra-violet laser pulse [26]. The laser pulse has a pulse duration of 6.4 ps (rms) in standard operation. After emission, the electrons are accelerated by a 1.5-cell normal conducting radio-frequency (rf) cavity operated at 1.3-GHz to an energy of about 5 MeV. While the bunch traverses the cavity, it is radially focused by a solenoid magnet in order to compensate for space-charge induced emittance growth. While the FLASH facility runs with bunch charges up to 1 nC, the seeded operation typically uses less electrons. While the charge for the seeded electron bunches should be as low as possible to reduce the impact of collective effects which deteriorate the bunch quality, the charge has to be high enough to form a homogeneous core region with a high peak current and low emittance and slice energy spread. For standard sFLASH operation this region has a length of about 200 fs for bunches at 0.4 nC.

2.5.2. Linear Accelerator

The electron gun is followed by a 130-m-long linear accelerator that consists of seven super-conducting 1.3 GHz accelerating modules. The first module accelerates the electron bunch up to 164 MeV before it enters the decelerating 3rd-harmonic module (marked in red in Fig. 2.2) which operates at 3.9 GHz and linearizes the longitudinal phase space distribution by removing the 1.3 GHz curvature of the first accelerator module from the uncompressed electron bunches [27]. Depending on the settings of the accelerating radio-frequency in the first two modules, the electron energy amounts to about 150 MeV after the 3rd-harmonic module when the electron bunch enters the first compression chicane. In this dispersive section of the linear accelerator, the electrons traverse energy-dependent path lengths allowing the higher energy electrons to catch up with the lower energy electrons. If the longitudinal phase space is properly prepared, such that the lower energy particles are in the head of the bunch, while higher energy particles follow in its tail, the electron bunch is compressed to higher peak currents and shorter bunch durations. A second stage of two super-conducting modules can then accelerate the beam to 450 MeV before a further chicane compresses the electron bunch up to a maximum peak current of 2.5 kA. The last four accelerator modules then allow acceleration of the electron beam up to 1.25 GeV kinetic energy.

Since the linear accelerator uses super-conducting rf modules, it is capable to maintain a constant accelerating gradient over several hundreds of µs. This so called macro-pulse is able to accelerate multiple electron bunches with a spacing of 1 µs leading to an intra-bunch repetition rate of 1 MHz. One macro-pulse can accelerate up to 800 pulses and is then repeated with 10 Hz.

2.5.3. FLASH1 Beamline

After traversing an energy collimator, the electrons enter the 25-m-long experimental section (sFLASH) that will be described in the next chapter. Downstream of the experimental seeding section the FLASH1 main undulator is located. It is composed of six fixed-gap planar undulator modules with a length 4.5 m each. The on-axis peak magnetic field of the undulator is $B_0 = 0.48\,T$ and its gap 12 mm [24]. The undulator parameter K is then given by

$$K = \frac{eB_0}{m_\mathrm{e} c k_\mathrm{u}} = 1.23. \tag{2.50}$$

Downstream of the FLASH1 main undulator, the electron beam is dumped and the photon pulse can be diagnosed or sent to a user experiment. The diagnostic tools at FLASH1 include, among others, a Ce:YAG screen to diagnose the transverse beam profile,

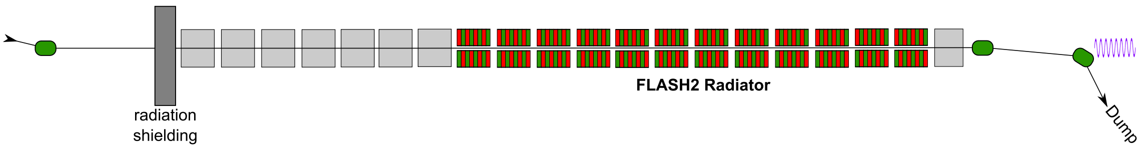

Figure 2.3.: Schematic overview of the FLASH2 beamline. The grey boxes along the undulator mark empty FODO half-cells.

	FLASH1	**FLASH2**
	Electron Beam	
electron energy	0.3 - 1.25 GeV	
peak current	$\leq 2.5\,\mathrm{kA}$	
bunch charges	up to 1 nC	
rf macro-pulse length	800 µs	
number of bunches per train	1-800	1-800
repetition rate	10 Hz	
	Main Undulator System	
type	planar, fixed gap	planar, variable gap
period *lambda*$_\mathrm{u}$	27.3 mm	31.4 mm
undulator parameter K	1.23	0.7 - 2.8
module length	4.5 m	2.5 m
number of modules	6	12
	FEL Radiation	
wavelength λ	54-4.2 nm	90-4 nm
pulse energy	$10 - 500\,\mu\mathrm{J}$	$10 - 500\,\mu\mathrm{J}$
pulse duration (fwhm)	$< 50 - 200\,\mathrm{fs}$	$< 50 - 200\,\mathrm{fs}$
spectral bandwidth (fwhm)	0.7-2.0%	0.7-2.0%

Table 2.1.: Experimental Parameters of the FLASH facility [24]

a gas monitor detector (GMD) as well as a grating spectrometer. The photon diagnostic systems are capable to resolve every photon pulse within the bunch train in order to provide shot-to-shot online diagnostics for user experiments [28].

2.5.4. FLASH2 Beamline

The extraction of the electron bunches to the FLASH2 beamline as well as the adaption of the bunch repetition scheme is briefly explained in Sec. 3.7. In this section we will focus on the downstream undulator system that consists of 12 modules. The modules have a length of 2.5 m each and a period length of *lambda*$_\mathrm{u} = 31.4\,\mathrm{mm}$. The maximum undulator parameter of the system is

$$K_\mathrm{max} = 2.8. \tag{2.51}$$

The undulator modules are organzied within the drift-space parts of 6 FODO cells. A FODO channel is comprised of a sequence of equidistant quadrupole magnets with the same magnetic field strengths. Focussing and defocussing quadrupole magnets alternate with drift spaces in between. A FODO cell is the smallest potion of the lattice that can be continued periodically [2]. At FLASH2 it has a length of $\lambda_{\mathrm{FODO}} = 6.6\,\mathrm{m}$ and consists of one focussing and one defocussing magnet. At an FEL with a FODO lattice the drift spaces in between the magnets are equipped with undulator modules.

Within the FLASH2 tunnel, some space is foreseen for a seeding setup. As can be seen in Fig. 2.3, only 12 of 20 FODO half-cells are filled with undulator modules. The other 8 are available for seeding hardware.

The photon diagnostic of FLASH2 is very similar to the systems installed at FLASH1 [28]. During the experiment described in Sec. 3.7 the spectrometer and GMD were not available. The only available diagnostic was a calibrated micro-channel plate (MCP).

Experimental parameters of the FLASH facility are summarized in Table 2.1.

3. Seeding at FLASH

When starting a high-gain free-electron laser from noise, properties of the generated photon pulse such as central wavelength and spectral shape are subject to fluctuations. Additionally, as described in Sec. 2.4, the longitudinal coherence of a SASE pulse is limited due to several longitudinal modes lasing independent from each other. One option to overcome these limitations is seeding the FEL process with an external coherent signal. This signal can either be a light field in case of direct seeding and self-seeding or a periodic modulation of the longitudinal charge density as used in, e.g., high-gain harmonic generation (HGHG), as discussed in Sec. 3.1.

When directly seeding an FEL, an external laser at the FEL fundamental wavelength is used and brought into overlap with the electron bunch. If the power of the light field significantly exceeds the spontaneous power of the shot-noise, the FEL acts as an amplifier and the coherence properties of the final FEL pulse will be determined by the initial seed. The sFLASH experiment has successfully shown the feasibility of direct seeding at 38 nm and 19 nm from a 38 nm seed laser beam in 2013 demonstrating spectral brightness contrast of 36 compared to SASE [29].

After this demonstration, the experimental focus of the sFLASH project shifted to seeding schemes that manipulate the longitudinal electron phase space distribution and prepare the electron bunch with a periodic current modulation to start the FEL process. The most simple scheme is the single-stage high-gain harmonic generation that uses an external laser pulse to imprint an energy modulation onto the electron beam and a dispersive chicane to convert this energy to a density modulation [30]. The experimental results presented in this thesis are based on this technique. This chapter will focus on theoretical foundation of this scheme as well as the hardware available at FLASH.

3.1. High-Gain Harmonic Generation

The most basic setup to seed an electron bunch using the high-gain harmonic generation (HGHG) technique consists of a short undulator, called modulator, that is used to imprint

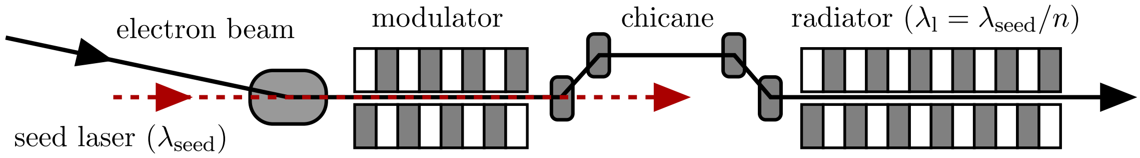

Figure 3.1.: Schematic layout of HGHG scheme. The laser pulse is brought to overlap with the electron beam in the modulator. A subsequent dispersive chicane converts the imprinted energy modulation to a density modulation that can radiate coherently in the radiator.

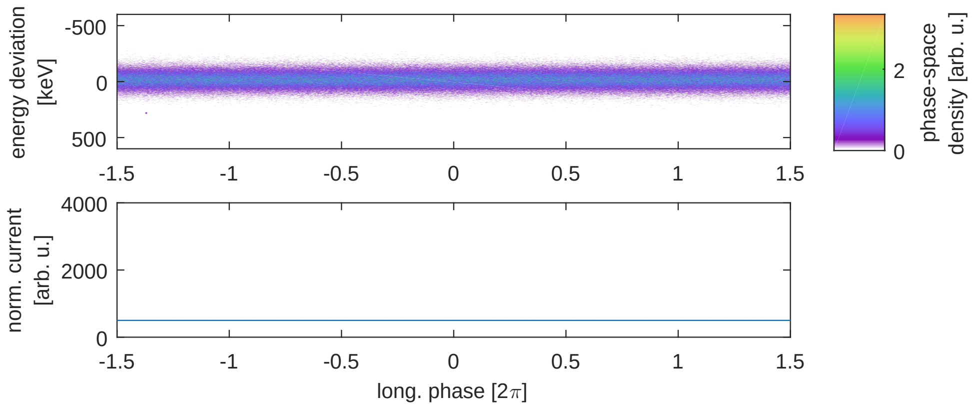

(a) Electron beam with a kinetic energy of $W_0 = 700\,\mathrm{MeV}$ and an uncorrelated energy spread of $\sigma_\mathrm{W} = 60\,\mathrm{keV}$ before modulation.

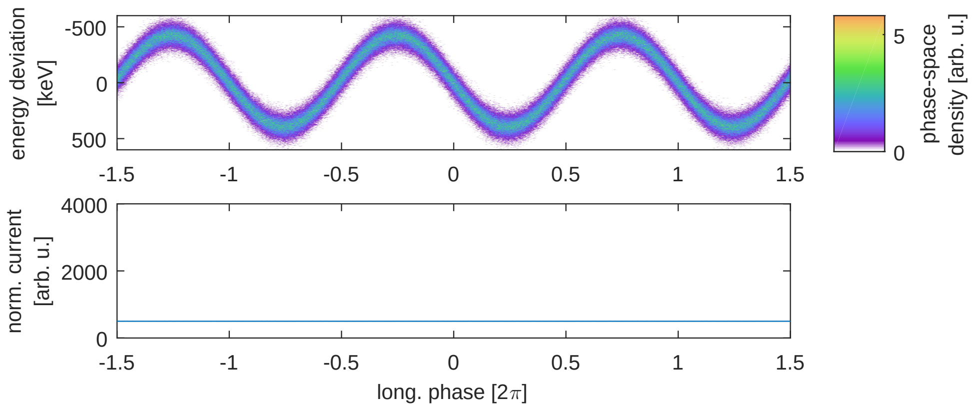

(b) The electron beam gets modulated with a modulation amplitude of about $\Delta W = 400\,\mathrm{keV}$ or $\Delta\gamma = 0.8$ at a wavelength of $\lambda_\mathrm{seed} = 266\,\mathrm{nm}$.

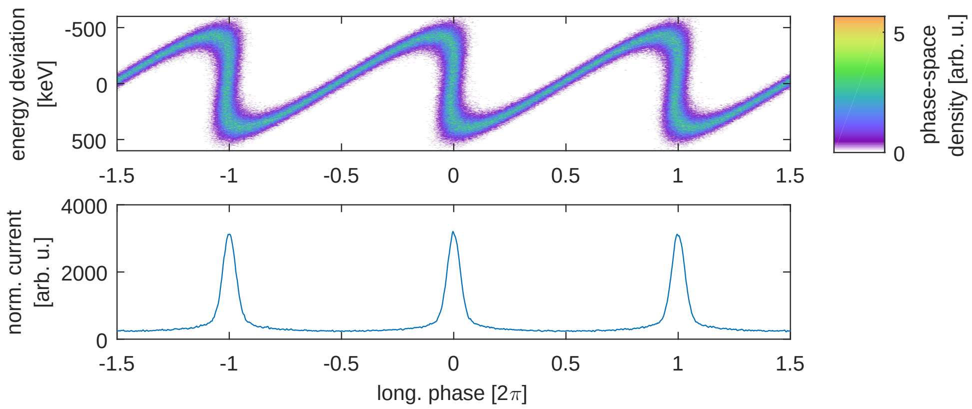

(c) The chicane with a dispersive strength of $-83\,\mathrm{\mu m}$ converts the induced energy modulation to a strong density modulation.

Figure 3.2.: Longitudinal phase space distributions and current profiles of an electron bunch *(a)* before entering the modulator, *(b)* after modulation, and *(c)* after the dispersive chicane. The parameters used to calculate these distributions are given in the captions of the individual figures.

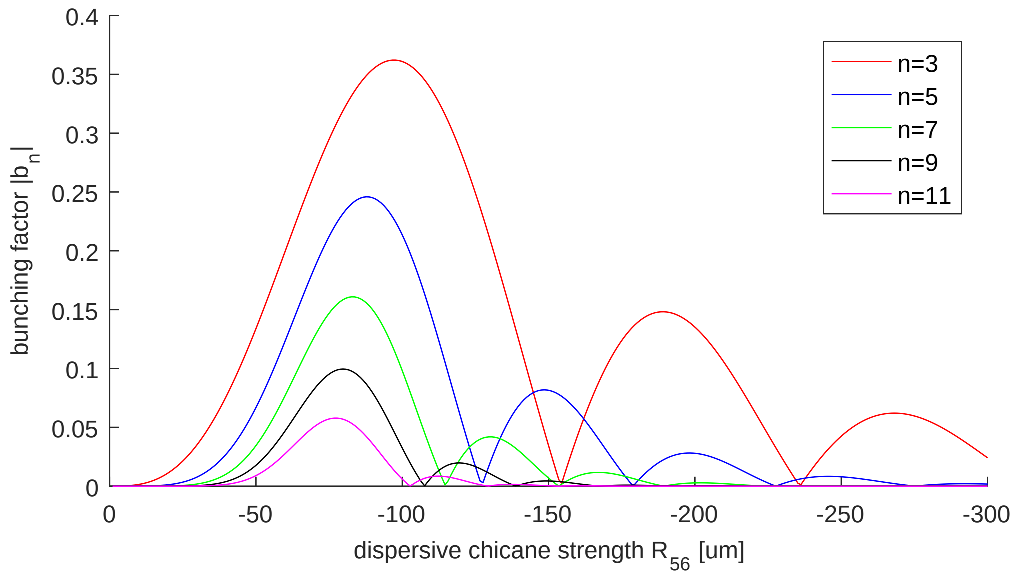

Figure 3.3.: Absolute of bunching factor on odd harmonics of the fundamental λ_l. The even harmonics are omitted in this figure to improve the readability. The calculations have been made for the parameters used in Fig. 3.2.

the energy modulation on the electron beam, a dispersive chicane that converts the energy modulation to a density modulation and a downstream long undulator, called radiator, where the FEL process gets started by the current modulation as depicted in Fig. 3.1. Though it was first proposed by L.-H. Yu [30], this section will closely follow a review article on laser-electron interaction [31].

The laser-electron interaction in the modulator works according to the theory we derived for the low-gain FEL. When transforming Eq. (2.12) to a comoving frame of the electron bunch, we can substitute the ponderomotive phase with $\Psi \to k_\mathrm{l} s/\bar{\beta}_\mathrm{z}$, where $\bar{\beta}_\mathrm{z} \approx 1$ is the electron velocity along the undulator axis and s is the co-moving intra-bunch coordinate. Here, $k_\mathrm{l} = 2\pi/\lambda_\mathrm{seed}$, since the resonance of the modulating undulator is tuned to the seed laser wavelength. The equation then becomes

$$\frac{\mathrm{d}\gamma}{\mathrm{d}z} = -\frac{eE_0 K_\mathrm{JJ}}{2\gamma m_\mathrm{e} c^2} \cos(k_\mathrm{l} s). \tag{3.1}$$

Since the induced modulation is small compared to the electron beam energy, the dispersive effects can be neglected in first order and an integration of this equation over z gives the energy deviation of the electron $\Delta\gamma$ from the mean energy of the electron bunch

$$\Delta\gamma(s) = \sqrt{\frac{P_\mathrm{L}}{P_0}} \frac{2K_\mathrm{JJ} N_\mathrm{u} \lambda_\mathrm{u}}{\gamma w_0} \cos(k_\mathrm{l} s). \tag{3.2}$$

Here, N_u is the number of undulator periods, λ_u the undulator period, and $P_\mathrm{L} = \epsilon_0 \frac{cE_0^2}{2} \frac{\pi w_0^2}{2}$ the laser beam energy with w_0 being the radius at which the intensity of the transverse laser beam profile drops to $1/e^2$ of its maximum. The total length of the undulator is then given by $L_\mathrm{u} = N_\mathrm{u}\lambda_\mathrm{u}$. Additionally, we define $P_0 = I_\mathrm{A} m_\mathrm{e} c^2/e \approx 8.7\,\mathrm{GW}$, where $I_\mathrm{A} = 4\pi\epsilon_0 m_\mathrm{e} c^2/e \approx 17\,\mathrm{kA}$ is the Alfvén current.

The projected energy spread of the electron beam after modulation is a superposition of its uncorrelated energy spread $\sigma_{\mathrm{W},0}$ and the induced modulation amplitude $\Delta\gamma$

$$\sigma'_\mathrm{W} = \sqrt{\sigma^2_{\mathrm{W},0} + \frac{(\Delta\gamma m_\mathrm{e} c^2)^2}{2}} = \sqrt{\sigma^2_{\mathrm{W},0} + \frac{\Delta W^2}{2}}, \tag{3.3}$$

where we introduced the absolute modulation amplitude $\Delta W = \Delta\gamma m_\mathrm{e} c^2$.

An electron beam that traverses the modulator will develop a relative energy deviation with the periodicity of the seed laser of

$$p' = p + A\sin(k_\mathrm{l} s), \tag{3.4}$$

where $A = \Delta\gamma/\sigma_\gamma$. Here, $p = \frac{\gamma-\gamma_0}{\sigma_\gamma}$ is the dimensionless energy deviation of the particle before the modulation process and p' the energy deviation afterwards. A beam that has a uniform longitudinal phase space distribution $f(p) = \frac{N_0}{\sqrt{2\pi}}\exp(-p^2/2)$ before the modulation process, will have a sinusoidally modulated electron phase space distribution after the modulator

$$f_1(s,p) = \frac{N_0}{\sqrt{2\pi}} \exp\left[-(p - A\sin(k_\mathrm{l} s))^2/2\right], \tag{3.5}$$

where N_0 is the number of electrons per unit length. After modulation the electron bunch traverses a dispersive element like a magnetic chicane. In linear beam optics, the longitudinal position of the electron is related to its energy deviation by the matrix element R_{56}, also called dispersive strength of the chicane[1]. With this relation $\mathrm{s}' = s + R_{56} p \sigma_\gamma/\gamma_0$ for the position of an electron after the chicane, the electron phase space distribution is given by

$$f_2(s,p) = \frac{N_0}{\sqrt{2\pi}} \exp\left[-(p - A\sin(k_\mathrm{l} s - Bp))^2/2\right], \tag{3.6}$$

where $B = R_{56} k_\mathrm{l} \sigma_\gamma/\gamma_0$. An integration of f_2 over p gives the one-dimensional electron density which can be expanded into a Fourier series with the Fourier coefficients c_n. For convenience, we however look at the bunching factor $b_\mathrm{n} = c_\mathrm{n}/2$ for the nth harmonic of the initial modulation period which can be given in analytical form:

$$b_\mathrm{n} = \exp^{-\frac{1}{2}B^2 n^2} J_\mathrm{n}(-ABn). \tag{3.7}$$

Thus, with a suitable combination of modulation amplitude $\Delta\gamma$ and dispersive strength R_{56}, significant bunching can be created. Figure 3.2 shows the longitudinal phase space distribution along with the current profiles of an HGHG seeded electron bunch. The parameters used for the plot are typical for the sFLASH experiment: $W = 700\,\mathrm{MeV}$, $\sigma_\mathrm{W} = 60\,\mathrm{keV}$, $\Delta W \approx 400\,\mathrm{keV}$, $\lambda_\mathrm{l} = 266\,\mathrm{nm}$ and $R_{56} = -83\,\mathrm{\mu m}$. In terms of the dimensionless

[1] Note, that the quantity R_mn refers to the matrix element of the transfer matrix in the mth row and nth column. Transfer matrices are square matrices with a dimension of 6. They map a vector characterizing the 6-dimensional state of a particle to its state after traversing the beamline described by the matrix. A full description can be found in [2].

scaling parameters used above, this corresponds to $A \approx 6.81$ and $B \approx 0.17$. sFLASH usually operates at the 7th harmonic where the bunching is about $|b_7| \approx 16\%$ with the parameters given above. A bunching on the percent level thus is more than sufficient to start the FEL lasing, since equivalent bunching one can associate with an FEL starting from noise is in the order of 10^{-4} [32]. Figure 3.3 shows the absolute of the bunching factor for the odd harmonics up to the 9th harmonic for the experimental parameters given above. Every harmonic has a slightly different optimum dispersive strength and the maximum of these maxima decreases. The smaller local maxima that follow the main one are cause by overbunching effects where the longitudinal phase space is strongly sheared and electrons are displaced by more than a fourth of the wavelength. Mathematically, this decrease in bunching factor is caused by the exponential factor in Eq. (3.7). It also shifts the values for optimum bunching to smaller R_{56} than the Bessel functions maxima.

The exponential factor in Eq. (3.7) will suppress the bunching at higher harmonics unless $B \approx n^{-1}$ in order to keep this factor from becoming too small. At the same time, the Bessel function should be maximized to achieve the highest possible bunching. Since the Bessel function of the order n reaches its maximum at a value of about n, this leads to

$$A \approx n \Leftrightarrow \Delta\gamma = n\sigma_\gamma. \tag{3.8}$$

This means that, as a rule of thumb, the induced laser modulation amplitude has to be n times bigger than the energy spread in order to generate the optimum bunching factor for the given harmonic.

Once a sufficient bunching is generated, the radiator downstream of the chicane can be tuned to the nth harmonic of the seed laser wavelength. As stated in the preceding chapter, the solution of the third-order differential equation, describing the evolution of the power during the FEL process, will look slightly different, when the FEL starts from an initial density modulation as compared to when it starts from an incoming seed light field. The solution is a superposition of the coherent emission of a bunched electron beam at the beginning of the undulator and the exponential FEL gain [33]:

$$P(z) = P_{\text{th}} \left[\frac{\frac{1}{3}\left(\frac{z}{L_{\text{g}}}\right)^2}{1+\frac{1}{3}\left(\frac{z}{L_{\text{g}}}\right)^2} + \frac{\frac{1}{2}\exp\left[\frac{z}{L_{\text{g}}} - \sqrt{3}\right]}{1+\frac{P_{\text{th}}}{2P^*_{\text{sat}}}\exp\left[\frac{z}{L_{\text{g}}} - \sqrt{3}\right]} \right], \tag{3.9}$$

where $P^*_{\text{sat}} = P_{\text{sat}} - P_{\text{th}}$ and $P_{\text{th}} = \rho_{\text{FEL}}|b_{\text{n}}|^2 P_{\text{beam}}$ is the power threshold at which the behavior of the power gain changes from the quadratic z-dependency of coherent radiation to the exponential regime of the free-electron laser. Here, b_{n} denotes the bunching factor on the nth harmonic of the seed laser, though it will be the fundamental of the FEL process in the radiator.

3.2. Echo-Enabled Harmonic Generation

A more advanced seeding technique that manipulates the longitudinal phase space distribution of the electron bunch is called echo-enabled harmonic generation (EEHG). It was first proposed by G. Stupakov in 2009 [34] who transfered the echo effect observed at

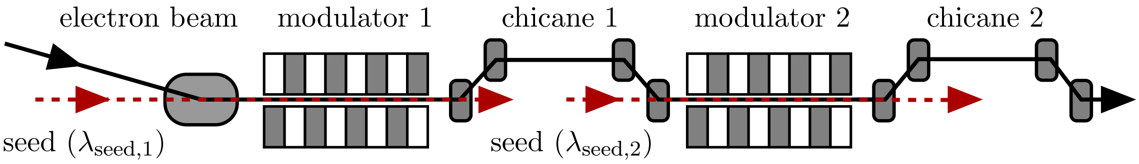

Figure 3.4.: Schematic layout of EEHG scheme. The first modulator and chicane are used to overshear the electron phase space distribution and produce thin stripes that are modulated again and bunched very similar to the process used during HGHG (see Fig. 3.1).

hadron accelerators to the generation of density modulations at high-harmonics in electron beams.

In this scheme (see Fig. 3.4), two modulator-chicane pairs provide the necessary phase space manipulation to generate current modulation at harmonics, the HGHG scheme cannot provide. A first modulator imprints an energy modulation at the laser wavelength $\lambda_{\mathrm{seed},1}$ that is used in the subsequent chicane with a high dispersive strength to overfold the electron bunch and create almost horizontal stripes in the longitudinal phase space distribution as can be seen in Fig. 3.5a. During this process, one period of the modulated electron beam is sheared in such a way, that its longitudinal extent covers several period lengths after the dispersive chicane. Since the particle density in phase space stays constant during the shearing process [2], the energy spread has to shrink while the longitudinal extent grows. Due to the periodicity of the modulation, the longitudinal phase space distribution features a lot of almost horizontal stripes, each with a small energy spread. A second modulator again imprints a modulation at wavelength $\lambda_{\mathrm{seed},2}$ and its subsequent chicane bunches the beam very much like in the HGHG case. With proper adjustment of the dispersive strengths, the resulting beam has a density modulation at the frequency of $mf_{\mathrm{seed},1} + nf_{\mathrm{seed},2}$, where m and n are integers and f is the frequency of the seed lasers. As can be seen in Fig. 3.5b, the fine stripes create much more narrow current peaks that contain more higher harmonics, due to their small effective energy spread. The plots have been created using the parameters prestend in [35] for an energy spread of $\sigma_{\mathrm{W}} = 60\,\mathrm{keV}$. Thus, among other advantages, EEHG can achieve higher harmonics than HGHG from the same electron and laser beam with relatively low laser modulation amplitudes.

3.3. Self-Seeding

A third option to seed an FEL, that was not yet treated in this thesis, is the self-seeding. In this seeding scheme a first FEL stage that starts from shot noise serves photon pulses with energies of a few microjoules. This radiation traverses a monochromator that cuts out a part from the photon pulse that corresponds to one spectral mode. The length of the resulting pulse spans the complete electron bunch longitudinally and gives a coherent input signal for the second undulator stage. Here the electron bunch is brought to overlap with the monochromatic light in order to start an FEL process with a coherent input signal.

This scheme will be treated in more detail in Sec. 6.1, but has to be mentioned here for completeness.

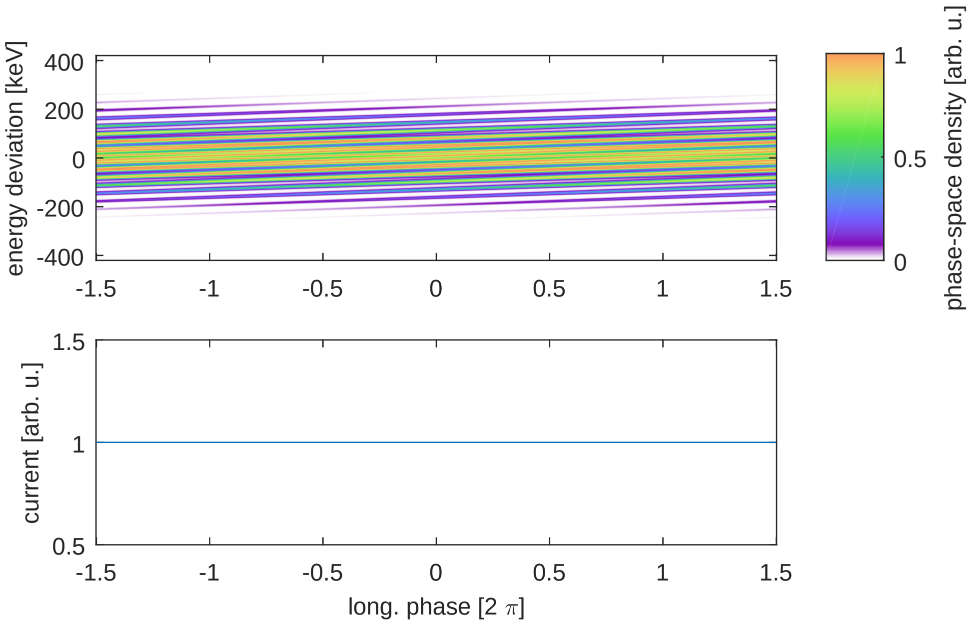

(a) Electron beam with an uncorrelated energy spread of $\sigma_\mathrm{W} = 60\,\mathrm{keV}$ after the first chicane of the EEHG setup.

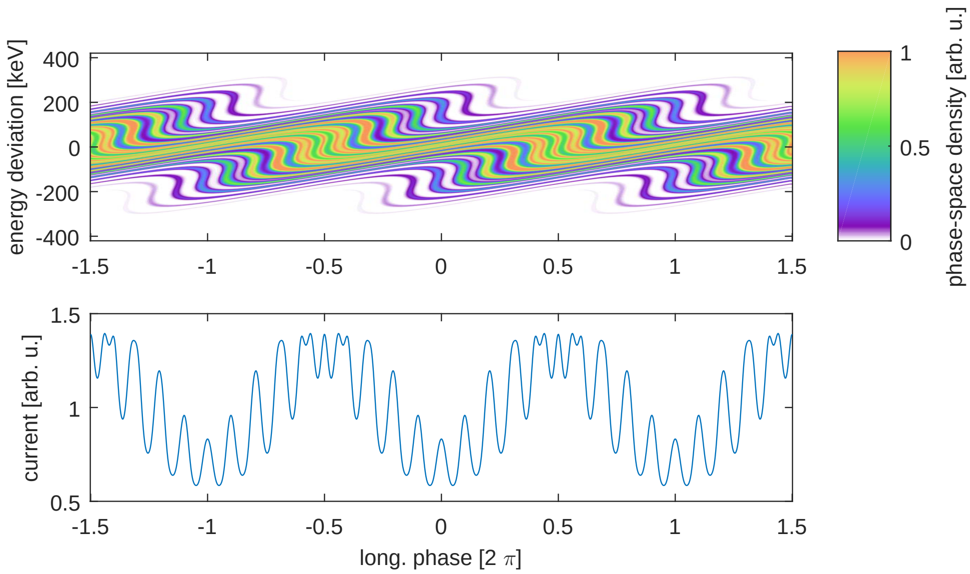

(b) Electron beam after second chicane of the EEHG setup optimized to lase at the 10th harmonic of the second seed laser.

Figure 3.5.: Longitudinal phase space distributions and current profiles of an electron bunch *(a)* after the first chicane of an EEHG setup and *(b)* after the second chicane.

3.4. Overview of Seeded Facilities

Seeding of an FEL is a technique that is pursued at many facilities over the world. In this section, a comparison of a few selected facilities in the x-ray and ultraviolet wavelength range is given together with characteristic numbers for the sFLASH experiment. The choice of facilities only includes phase-space manipulating techniques like HGHG and EEHG as well as self-seeding and omits FELs directly seeded with an external laser.

The first experimental realization of this seeding scheme has been done at Brookhaven National Laboratory (BNL) by L.-H. Yu and others in 2000 [36]. A 10.6 µm CO_2 laser generates the modulation amplitude. The FEL process at the second harmonic of the modulating laser saturated in a 2 m-long undulator. With an energy of 65 µJ, the HGHG signal exceeded the SASE signal of the undulator by more than 6 orders of magnitude. The first advance to HGHG seeding with smaller wavelength by the same group at the Deep Ultraviolet FEL (DUV FEL), only three years later, achieved a spectral brightness contrast of 10^5 in contrast to SASE. Here, the radiation was generated at 266 nm, the third harmonic of the seed laser [37]. Since these pioneering experiments, an HGHG seeded FEL user facility was built in Trieste (FERMI) and meanwhile operates two parallel undulator beamlines [38]. The single-stage HGHG at FEL-1 covers a wavelength range of 20 to 100 nm with pulse energies up to 200 µJ. The second beamline, FEL-2, runs in a cascaded HGHG setup where a first HGHG stage generates the input seed radiation for a second stage. This way, the facility offers 4 nm radiation to user experiments with an average energy per pulse of 10 µJ [39]. Other HGHG facilities include the Shanghai deep-ultraviolet FEL (SDUV-FEL) and the FEL user facility Dalian Coherent Light Source (DCLS) that started operation in 2016 [40, 41].

The first proof-of-principle experiment for echo-enabled harmonic generation was conducted by D. Xiang and other in 2010 [42]. The group reported the generation of radiation from the 3rd and 4th harmonic of the second seed laser at an experiment at Next Linear Collider Test Accelerator (NLCTA) at SLAC National Accelerator Laboratory. Recently, the generation of harmonics up to the $75th$ of the second seed laser wavelengths was achieved by E. Hemsing and other at the same facility [43]. Here, a 120 MeV electron beam was modulated with two different laser pulses ($\lambda_{\text{seed},1} = 800\,\text{nm}$, $\lambda_{\text{seed},2} = 2400\,\text{nm}$) according to the EEHG principle. Though the beam current was not sufficient to start an exponential gain process, coherent radiation has been observed down to 32 nm.

Self-seeding was successfully demonstrated at LCLS in the soft and hard x-ray range in 2015 and 2012, respectively. The hard x-ray setup works with a diamond crystal that is used as a monochromator and achieved a reduction of the FEL photon pulse bandwidth by a factor of 40-50 at a wavelength of about 0.14 nm [47]. The soft x-ray design features a compact grating monochromator and operates at wavelength of about 1.2 to 2.5 nm [48]. The feasibility of an adaption of this scheme to FLASH parameters is studied in Sec. 6.1.

Table 3.1 shows an incomplete list today's seeded FEL facilities and their experimental parameters.

	sFLASH	SDUVFEL	DCLS
seeding scheme	HGHG	HGHG,EEHG	HGHG
location	Hamburg, Germany	Shanghai, China	Dalian, China
wavelength range	29.5 – 38.1 nm	HGHG: single-stage: 290 – 790 nm double-stage: 300 nm EEHG: 350 nm	50 – 150 nm
energy per pulse	70 µJ	HGHG: 100 nJ to 1 µJ EEHG: 1 µJ	100 µJ
rel. spectral width (rms)	$\leq 2.5 \cdot 10^{-3}$ at 38.1 nm	10^{-3} at 350 nm	10^{-3} at 20 nm
references	[44]	[40, 45]	[41, 46]

	FERMI@Elettra	NLCTA	LCLS
seeding scheme	HGHG FEL-1: single-stage FEL-2: double-stage	EEHG	Self-Seeding
location	Trieste, Italy	Stanford, USA	Stanford, USA
wavelength range	FEL-1: 20 – 100 nm FEL-2: 4 nm	down to 32 nm	soft x-ray: 2.5 – 1.2 nm hard x-ray: 0.137 – 0.155 nm
energy per pulse	30–200 µJ	no FEL gain	soft x-ray: 200 µJ hard x-ray: 60 µJ
rel. spectral width (rms)	FEL-1: 10^{-4} FEL-2: $6 \cdot 10^{-2}$ at 4 nm	10^{-4}	soft x-ray: $8 \cdot 10^{-5}$ at 1.3 nm hard x-ray: $5 \cdot 10^{-5}$ at 0.149 nm
references	[38, 39]	[43]	[47, 48]

Table 3.1.: Comparison of experimental parameters of a selection of today's seeded FEL facilities.

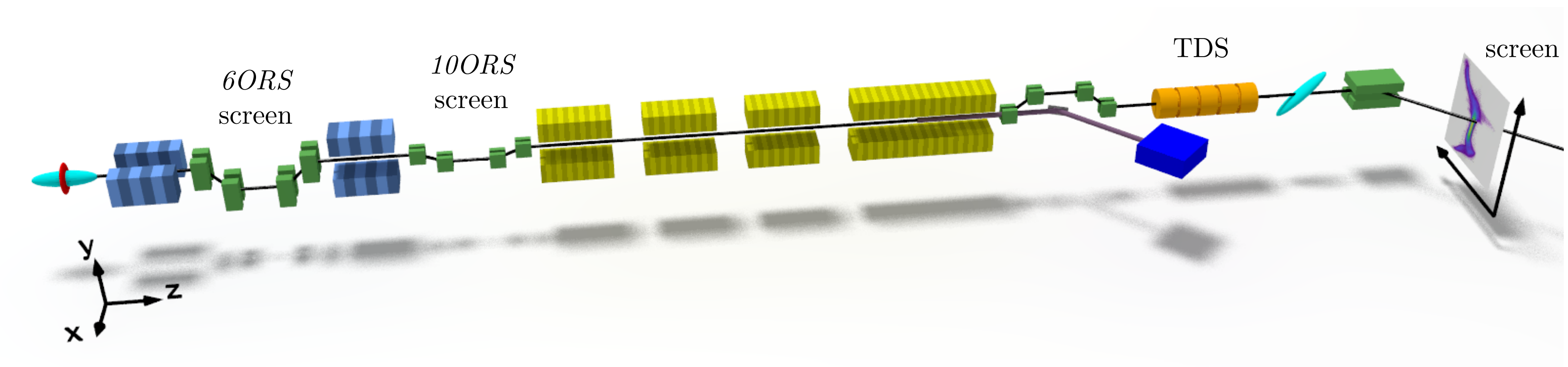

Figure 3.6.: Schematic layout of the sFLASH experiment. The electron bunch comes from the linear accelerator (left) and gets overlapped with the laser beam (red). The beamline provides two modulators (blue), the first with a horizontal field and the second with a vertical field. These modulators are followed by one chicane each. The first chicane exhibits stronger magnets to allow for the overshearing of the longitudinal phase space distribution and enables EEHG operation. The deflection of the second chicane, which is usually used as bunching chicane in HGHG operation, is smaller. The modulator chicane pairs are followed by the long radiator section which consists of four dedicated variable-gap undulators (yellow) described in more detail in the text. After radiation, the electron bunch bypasses the photon extraction mirror that couples the FEL pulse out to a set of photon diagnostics and a photon characterization laboratory (blue box). The electron bunch traverses an rf deflector (TDS) setup that – together with a dipole spectrometer – allows for the measurement of the longitudinal phase space distribution of the electron bunch after FEL lasing.

3.5. sFLASH – The seeding Experiment at FLASH1

Since 2014, the sFLASH experiment focuses on the demonstration and investigation of seeding schemes that manipulate the longitudinal phase space of the electron bunch before lasing. With its hardware setup, the experiment provides hardware for HGHG, as well as EEHG seeding schemes.

The beamline section devoted to the experiment has a total length of about 25 m and is located right after the energy collimator section downstream of the linear accelerator section. A schematic overview of the section including the rf deflector setup, can be seen in Fig. 3.6. The two modulator undulators are electro-magnetic undulator modules with a period length of $\lambda_u = 0.2\,\mathrm{m}$, 5 effective periods and a maximum undulator parameter of $K_{\mathrm{max}} = 10.8$ that were originally installed for the Optical Replica Synthesizer (ORS) experiment [49]. The undulators, however, have different orientations. The first undulator deflects in the vertical plane with a horizontal magnetic field, while the second deflects horizontally. Both modulators are followed by a dedicated chicane that deflects vertically in both cases. The first chicane can generate a maximum longitudinal dispersion of $R_{56} = 700\,\mu\mathrm{m}$, the second one can introduce a dispersion up to $R_{56} = 200\,\mu\mathrm{m}$ at an electron energy of 700 MeV. The first chicane can achieve a higher dispersion in accordance with the needs of the EEHG scheme, where the first chicane has to overfold the electron bunch with a high R_{56}.

Both chicanes are equipped with screen stations to analyze the seed laser light or radiation from the modulators. The screen stations feature a Ce:YAG crystalline screen that is used for precise measurements of the beam position. A screen that generates optical transition radiation can be used for accurate measurements of the beam size. Both screens are imaged via an optical system that employs one of two lenses for different magnifications and uses different filters for intensity attenuation. The two screens are called *6ORS* and *10ORS*, respectively.

The second chicane is followed by the radiator section. The sFLASH radiator is comprised of four variable-gap undulator modules: Three U32 undulators with a period length of $\lambda_u = 31.4\,\mathrm{mm}$, 60 periods and a maximum undulator parameter of $K_{\mathrm{max}} = 2.72$ precede a fourth U33 module with a period length of $\lambda_u = 33.0\,\mathrm{mm}$, 120 periods and $K_{\mathrm{max}} = 3.03$ [50]. A quadrupole magnet on a transverse moving system, a wire scanner to measure electron beam sizes, and a screen system for electron and laser beam size and position measurement is located in the 0.7-m-gap between every undulator module. The quadrupoles also contain beam position monitors that determine the beam position by picking up the electro-magnetic fields that a passing electron beam generates [51]. Every drift between the undulator modules also contains a compact electro-magnetic phase shifter that can be used to adjust the phase of the electrons with respect to the propagating light field to ensure a continuing energy transfer from the electrons to the light field in the subsequent undulator module.

Downstream of the radiator another chicane is located that enables the electron bunch to bypass the extraction optics for the FEL pulse. The extraction mirror diverts the photons either to a photon diagnostics setup featuring a micro-channel plate (MCP) and a spectrometer, or to the experimental laboratory to further characterize the sFLASH photon pulses.

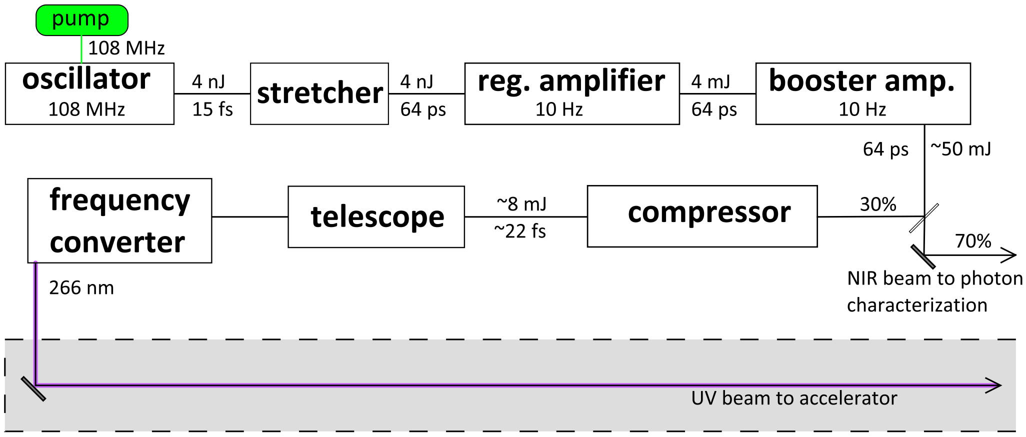

Figure 3.7.: Schematic layout of the seed laser system. Pulse energies and lengths are referenced between the stages, as well as the repetition rates at the stages.

The electron beam traverses an rf deflector setup further downstream. In combination with a dipole spectrometer this rf deflector enables measurements of the longitudinal phase space distribution in a destructive way. Alternatively, the electron bunch can be sent through the main undulator of the FLASH1 beamline. Note that an operation of the sFLASH experiment with closed sFLASH undulators can, depending on the energy, strongly influence the optical functions in the FLASH1 main undulator. Especially a change of the gaps without disturbances of FLASH1 operation is challenging.

A novel mathematical method has been developed to calculate corrections for quadrupole currents for these optics disturbances [52]. It bases on keeping the transfer matrix within the beamline section constant in order to maintain the downstream optical functions. Continuous correction functions for six quadrupole currents can be found that keep the transfer matrix constant by means of the implicit function theorem. In contrast to the numerical methods used in particle tracking codes to solve these kind of problems, the novel formalism can determine continuous functions for correction parameters that compensate the disturbance (e.g. for the closing process of a variable-gap undulator). The method has successfully been used for the compensation of the undulator focussing of the sFLASH undulator system at 700 MeV and 1000 MeV.

3.5.1. Seed Laser System

Though the laser setup has been recently modified, this section gives a brief overview of the laser setup at the time of acquisition of the data presented here [53]. A schematic overview can be found in Fig. 3.7. The laser oscillator system is a commercially available solid-state titanium-sapphire laser. The generated pulses are amplified by means of the chirped pulse amplification technique to an energy of 50 mJ per pulse at 800 nm central wavelength with a bandwidth of about 35 nm and a repetition rate of 10 Hz. Note that with this repetition rate only one bunch in every pulse train can be seeded at sFLASH.

Before the amplified bunches are compressed down to a fwhm pulse length of 50 fs with a remaining pulse energy of 8 mJ, they traverse a beam splitter and energy attenuator that allows the control of the pulse energy in the compressor. The beam splitter separates 70% of the beam energy that is sent to the photon characterization lab of sFLASH. The main part of the 800 nm beam is then transported over 12 m to the frequency tripling setup. The transport line is composed of 3 m distance in air, a fused silica vacuum window and 9 m of vacuum beamline. In order to avoid non-linear effects that could disturb the laser wavefronts, the beam size is increased by a factor of 3 to about 12 mm for the transport.

For frequency tripling the beam first enters a β-Barium borate (BBO) crystal that converts the 800 nm beam up to its second harmonic at 400 nm. A subsequent α-BBO plate adds the delay to the fundamental mode in order for the two colors to overlap longitudinally, and a wave plate ($\lambda/2$ for 800 nm, λ for 400 nm) aligns the polarization of both beams in the second BBO crystal for efficient upconversion to the third harmonic at 266 nm. The conversion efficiencies to second and third harmonic are approximately 20% and 9%, respectively. The fwhm pulse duration of the third harmonic after the conversion is estimated to be 150 fs short.

The ultraviolet 266 nm laser beam is then coupled into the electron beamline via three mirrors that are motorized in order to remotely steer the laser beam for transverse laser-electron overlap in the modulator.

3.5.2. Operation Procedures

Running the HGHG experiment reliably needs preparation of the electron beam. Additionally to standard FLASH setup procedures, the electron bunch optics need to be controlled carefully. For this, standard matching procedures are applied that calculate quadrupole current corrections to adapt the electron beam optics to a theory optic. To achieve reproducible experimental conditions for the seeded operations, several iterations of the matching procedure to the standard theory optics in the FLASH injector area are performed. Another set of iterations is conducted with measurements and correcting quadrupoles in the sFLASH experimental section. This procedure is crucial to achieve small beam sizes in the undulator segments for an efficient modulation and FEL process. Additionally, the extensive analysis of the experimental results described in this thesis would not be possible without knowledge of the electron optics.

In order to avoid unnecessary kicks of the microbunched electron beam that might deteriorate the bunching factor, all quadrupoles between the second modulator and last segment of the radiator are switched off. Also quadrupoles upstream of the modulator deviate from standard operation settings, since they are used to create a beam waist within the sFLASH radiators.

After careful setup of the electron beam conditions, the bunch and seed laser are brought to transverse overlap in the modulator using the screens *6ORS* and *10ORS* to measure transverse positions of the seed laser and electron beam. Once transverse overlap has been established, the bunching chicane is switched on to a dispersive strength between $R_{56} = -50\,\mu\mathrm{m}$ and $R_{56} = -100\,\mu\mathrm{m}$. A delay stage is utilized to scan the longitudinal overlap while monitoring the electron bunch on the dispersive screen of the rf deflector setup. The modulation can be identified on the screen by eye as can be seen in Fig. 5.3 (p. 59).

After the six-dimensional overlap is set, the radiator segments are closed one by one. A gap scan of every module while monitoring the energy signal of the MCP reveals a maximum when the undulator parameter hits the resonance. Note that these scans would look fundamentally different for an FEL operated in SASE mode of operation. The micro-bunched beam ensures an effective start of the FEL process once the K parameter is resonant with a wavelength that is a harmonic of the micro-bunching periodicity. Once two undulator segments are closed and in resonance with the seeded wavelength, the phase shifters between the modules are scanned and set to the currents with maximum output in FEL energy.

Empirical tuning of the electron orbit as well as accelerating rf settings and solenoid current are used to optimize the energy output of the seeded FEL signal.

3.6. FLASH2 – A Seeded User Machine?

The FLASH2 beamline currently enables the generation of high-brilliance FEL SASE pulses. There is, however, enough space upstream of the main undulator modules to install a dedicated seeding beamline that serves its radiation to user experiments. Irrespective of the seeding schemes installed here, the FLASH2 beamline should maintain its current ability to lase in SASE mode of operation. The seeding scheme installed has to exploit the unique advantage of the FLASH facility that can serve electron bunches with higher repetition rate than other free-electron lasers that are not based on a superconducting linear accelerator.

In this thesis, feasibility studies for two different seeding schemes are presented in Chapter 6:

- **Self-Seeding.** As briefly discussed above, self-seeding is a seeding scheme where the light of an upstream undulator is used as a direct seed for a subsequent undulator stage. This way the spectral brightness of the final FEL pulse can be increased. Since a possible seeding scheme should reach down to small wavelength, a working point study for a 5 nm self-seeding scheme employing an adapted monochromator design from LCLS is shown in Sec. 6.1. A sketch of a possible layout is shown in Fig. 3.8a together with the indication of what changes would have to be done to the existing hardware.

- **Single-stage HGHG seeding.** As a first step towards more advanced phase-space manipulating seeding schemes such as EEHG or a double-stage cascaded HGHG setup, a single-stage high-gain harmonic generation setup has been studied based on the model of and with the expertise gained from sFLASH. Numerical simulations and a brief discussion on the choice of hardware to be installed is given in Sec. 6.2. A sketch of a possible layout is shown in Fig. 3.8b together with the indication of what changes would have to be done to the existing hardware. The results shown are a contribution to the conceptual design report for a seeded undulator beamline at FLASH2.

3.7. Simultaneous Operation

The draw-back of most modern-day FELs is that they can only serve one user end-station at a given time. As described above, FLASH, however, has two undulator beamlines.

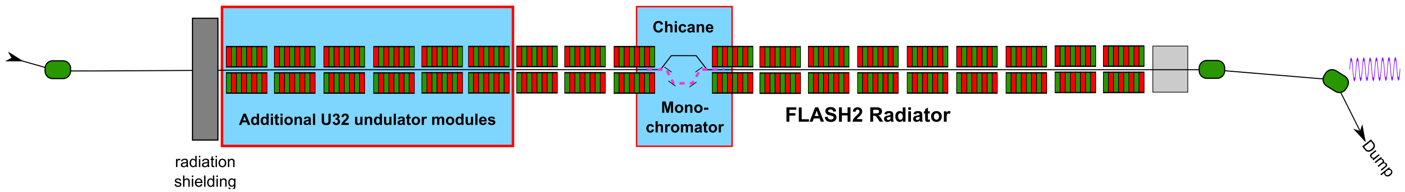

(a) Possible self-seeding-capable layout for FLASH2. A monochromator for the light from the first stage together with a bypassing chicane for the electrons has to be installed between two undulator stages. Additional undulator modules have to be installed in order to generate sufficient FEL pulse energies for seeding.

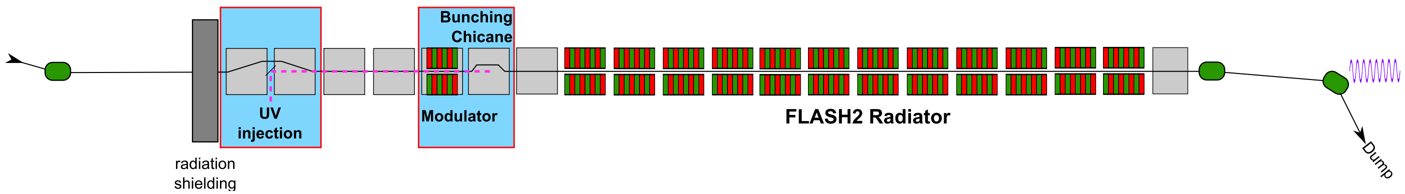

(b) Possible single-stage HGHG-capable layout for FLASH2. An injection for the seed laser, as well as a modulator and bunching chicane have to be added in front of the FLASH2 main undulator that will be used as radiator.

Figure 3.8.: Possible layouts for SASE compatible seeding schemes at FLASH2. Shown are the self-seeding option in panel *(a)* and the HGHG option in panel *(b)*. The blue shaded areas show additions to the existing SASE beamline. The grey shaded boxes are free slots where hardware of the length of one undulator module can be installed.

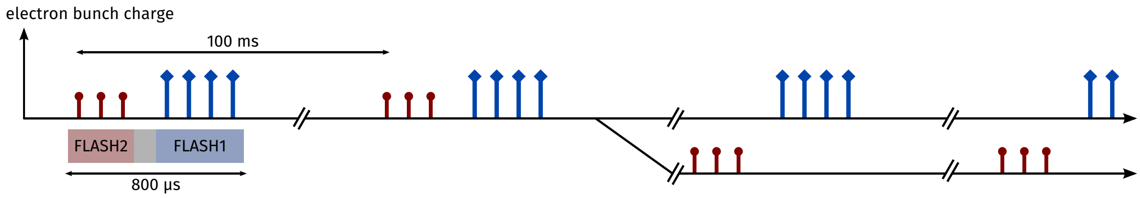

Figure 3.9.: Temporal electron bunch pattern at the FLASH facility. The blue diamond-hatted vertical bars represent the bunch train dedicated to FLASH1, followed by a 30 µs gap that is used to ramp-up the kicker magnet in order to kick the remaining part of the bunch train to FLASH2 (indicated by the red dot-hatted bars). Reprinted with permission by Journal of Synchrotron Radiation [54].

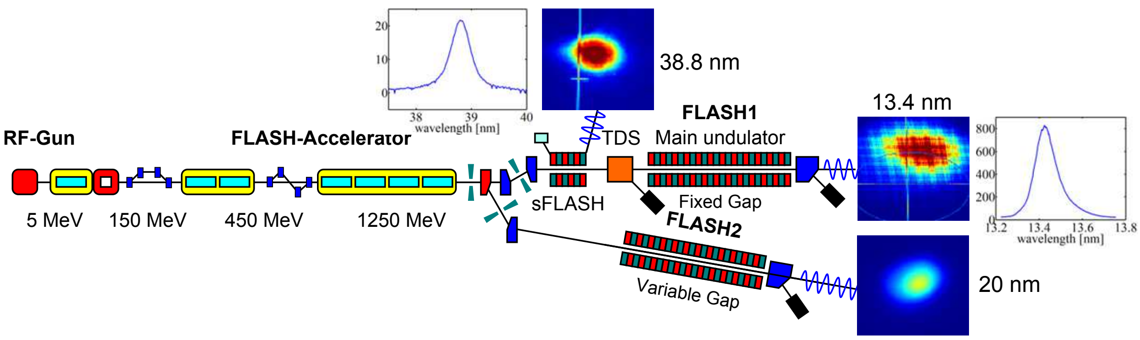

Figure 3.10.: Schematic view of the FLASH facility. The measured beam profiles at all three beamlines as well as averaged spectra for sFLASH and FLASH1 are shown. The beam image of FLASH1 is slightly disturbed due to an MCP intensity detector placed in front of the screen. Reprinted with permission by Journal of Synchrotron Radiation [54].

	sFLASH	FLASH1	FLASH2
Electron bunch energy (MeV)	674	674	692
Charge (nC)	0.26	0.26	0.29
Undulator Parameter K	2.57	1.19	1.53
Undulator Parameter λ_u (mm)	31.4	27.3	31.4
Wavelength λ (nm)	38.8	13.4	20
Photon Pulse Energy	(83 ± 39) nJ	(77.6 ± 2.9) µJ	(146 ± 25.4) µJ
rms energy stability	47.0%	3.7%	17.3%
Relative Spectral Width (fwhm)	1.2%	0.84%	No measurement

Table 3.2.: Electron and photon parameters of the multi-beamline lasing experiment. [54]

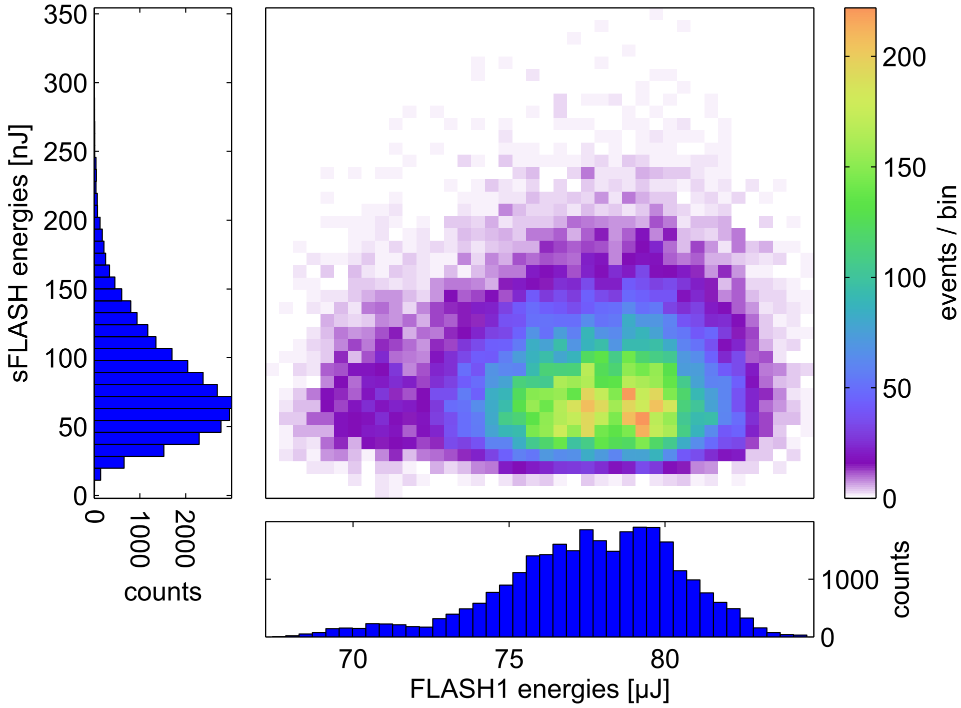

Figure 3.11.: The central plot shows the correlation of measured photon pulse energies of FLASH1 and sFLASH of about 29000 consecutive shots. The color code shows the events per bin. Next to both axes the respective histograms are shown. The sFLASH histogram shows a gamma distribution, while FLASH1 shows a more Gaussian-like distribution as expected from an FEL running into saturation. Reprinted with permission by Journal of Synchrotron Radiation [54].

Electron bunches can be distributed with the full macro-pulse repetition rate of 10 Hz to both beamlines enabling the delivery of photon pulses to two user end stations [25]. With the sFLASH experiment in front of the main undulator of FLASH1, the complete facility can serve photon pulses to three different dedicated end stations. With this layout of undulator beamlines, the FLASH facility is a good test bench for future FEL concepts that incorporate both, parallel and sequential configurations of undulator beamlines [55, 56, 57]. The results presented in this section are a first step towards a simultaneous seeded operation at sFLASH [54].

For simultaneous operation of parallel beamlines, the bunch train generated from the gun has to be split. The rf macro-pulse has a plateau of 800 µs which can accelerate a train of up to 800 bunches with an intra-bunch spacing of 1 µs. In standard operation, the first bunches of this train go to FLASH1, followed by a 30 µs gap that is used to ramp up the current of the kicker magnet that deflect the remaining bunch train to FLASH2. Figure 3.9 shows a schematic view of the bunch pattern at FLASH.

For this proof-of-principle experiment, one electron bunch has been delivered to either beamline separated by 500 µs. The electron beam distributed to FLASH1 was set up at 674 MeV kinetic energy leading to a wavelength of 13.4 nm at the main undulator. The variable-gap undulator systems at sFLASH were tuned to radiate at 38.8 nm. The electron bunches directed to FLASH2 where set up with a slightly higher kinetic energy of 692 MeV and the variable-gap undulator was tuned to 20 nm. Using the transverse deflecting cavity, the peak current of the bunch distributed to FLASH1 could be measured to be 1.3 kA with an rms duration of 83 fs. Though there is no longitudinal diagnostics installed at FLASH2 yet, one can safely assume a similar current profile, since the accelerating rf settings were only slightly changed from those at FLASH1 to optimize SASE output for FLASH2.

The energy of the photon pulse properties have been characterized individually at each photon diagnostic station using calibrated micro-channel plates at sFLASH and FLASH2, and a gas-monitor detector [58] at FLASH1. The photon energies have been measured to be (83 ± 39) nJ at sFLASH, (77.6 ± 2.9) µJ at FLASH1 and simultaneously (146 ± 25.4) µJ at FLASH2. Averaged spectra of sFLASH and FLASH1 have been measured and averaged spectra are shown in Fig. 3.10 next to beam profile measurements. The wavelength for FLASH2 has been calculated using the resonance condition in Eq. (2.8). Experimental parameters are summarized in Table 3.2.

The energy generated by the FEL in SASE mode is subject to statistical fluctuations. Simulations show that the sFLASH undulator length corresponds to about 14 gain lengths with these experimental settings. Since this length is not sufficient to run into saturation, the photon energies at the sFLASH beamline follow a characteristic gamma distribution with high relative pulse energy fluctuations as shown in Fig. 3.11. The figure also shows a correlation of the photon energies measured from the same bunch at sFLASH and FLASH1. Though the FEL process at sFLASH is well in the exponential regime, the gain is too small to have a significant effect on the electron bunch and thus on the FLASH1 photon pulse energies. FLASH1 does not show the gamma distribution, but a photon statistic that is closer to a Gaussian that is typical for an FEL process that runs into saturation [18].

Note that with a proper choice of the undulator parameter the FLASH1 undulator radiates at the third harmonic of the wavelength at sFLASH. Microbunching generated at the seeding beamline could be used to start the FEL process in the FLASH1 main undulator. However, since the experiment shown here utilized photon diagnostics at every undulator beamline, the extraction chicane after the sFLASH radiator had to be powered. The longitudinal dispersion from this chicane smears out any microbunching generated by the FEL process upstream.

These results not only show the feasibility of parallel and cascaded operation of several FELs from one linear accelerator, but are also a first step towards simultaneous seeded operation of the sFLASH experiment. Future efforts can aim to generate photon pulses with energies up to about 100 µJ in both undulator beamlines in FLASH1. If the seeding process extracts more energy from the bunch and thus significantly deteriorates the quality of the electron beam, lasing from the same electron bunch in the subsequent FLASH1 undulator could be less effective. However, since the FLASH accelerator is using superconducting technology, the FLASH1 beamline can run with much more than one electron bunch in its train. One of those electron bunches can be seeded at the sFLASH experiment and extracted by the rf deflector kicking magnet, while the rest of the electron bunch traverses the beamline to FLASH1 lasing with full efficiency.

Note that the undulator parameter of the FLASH1 beamline given here is $K = 1.19$, though the original specifications give a parameter of $K = 1.23$. The sFLASH undulator gap shows a similar deviation towards smaller values of K compared to its look-up table. This suggests that the energy measurement is subject to a systematic deviation. While it shows 674 MeV for the kinetic energy of the electron beam at FLASH1, a value of 683 MeV fulfills the resonance conditions with $K = 1.23$ at FLASH1 and an undulator parameter closer to the look-up table value at sFLASH. This could mean that FLASH electron energy measurements exhibit an error of about 1.4%. This error, however, will not be treated in the remaining parts of the thesis since its impact on the results discussed is small compared to other measurement errors.

4. Pulse Power Profile Reconstruction and Time-Resolved Emittance Estimation

For many photon science experiments exact knowledge of the photon pulse characteristics is highly desirable [59, 60, 61]. Whereas devices like a Gas Monitor Detector (GMD) allow for a non-destructive single-shot measurement of the photon pulse energy [58], the determination of other characteristics usually leads to absorption of a significant part of light.

A non-destructive method to determine the photon pulse characteristics is to measure the medium that amplified it, particularly the longitudinal phase space distribution of the electron bunch after radiating the FEL pulse. Here, the energy drop of the electrons due to radiation can be used to estimate the characteristics of the FEL photon pulse [62]. When the FEL saturates and the photon pulse power reaches P_{sat}, the mean energy drop a lasing slice will experience is about $\Delta W \approx P_{\mathrm{sat}} e/I = 1.6\rho W_0 = 1.7\,\mathrm{MeV}$ for typical parameters at sFLASH ($\rho \approx 1.5 \cdot 10^{-3}$, $W_0 \approx 700\,\mathrm{MeV}$). From this measurement one can reconstruct the longitudinal FEL power profile on a shot-to-shot basis without destructing the photon pulse. At the sFLASH experiment such a characterization is possible with a transverse deflecting structure (TDS) installed directly downstream of the extraction chicane after the last radiator segment. The majority of the results presented in this chapter have been published in [63].

The TDS is a cavity which is powered by a radio-frequency (rf) field kicking the electrons by an amount depending on their arrival time. At a screen installed in a sufficient betatron phase advance distance, this kick translates into an arrival-time dependent offset along the kick direction. A dipole, downstream of the TDS, deflecting in the perpendicular plane disperses the electrons dependent on their energy. On a subsequent screen the electron distribution can then be observed. A schematic layout of the experimental setup can be seen in Fig. 4.1 The coordinate of an electron on the screen can be written as [64]

$$x(\eta) = x_{\mathrm{i}} + D_{\mathrm{x}}\eta, \tag{4.1}$$

$$y(t) = y_{\mathrm{i}} + C_{\mathrm{y}}t + S_{\mathrm{y}}t, \tag{4.2}$$

where D_{x} is the dispersion induced by the dipole, η the relative energy deviation, S_{y} is the shear parameter that describes the induced kick of the TDS, and C_{y} describes the initial $y-t$ correlation of the bunch. The initial transverse coordinates of the particle are denoted by x_{i} for the plane of the electron spectrometer and y_{i} for the kicking plane of the TDS, respectively.

The shear parameter is measured by changing the phase of the deflecting rf field with respect to the electron bunch. The bunch then gets a different kick and the center of mass of the phase space density can be used to determine the arrival time of the electron bunch with respect to the rf phase. With this method, the shear parameter S_{y} was measured for

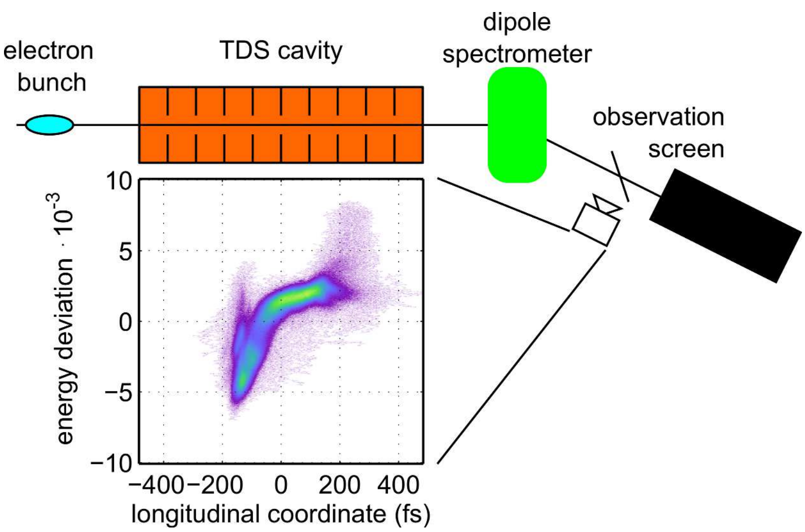

Figure 4.1.: Schematic layout of the transverse deflecting cavity arrangement. The electron bunch travels from left to right. It experiences an arrival-time-dependent deflection in the cavity in the x-plane. Passing through a subsequent dipole the electrons are dispersively kicked in the y-plane. This leads to an image that shows the longitudinal profile in one direction and the energy spectrum in the other. A characteristic measurement of the longitudinal phase space distribution is shown at the bottom. Reprinted with permission by Journal of Synchrotron Radiation [54].

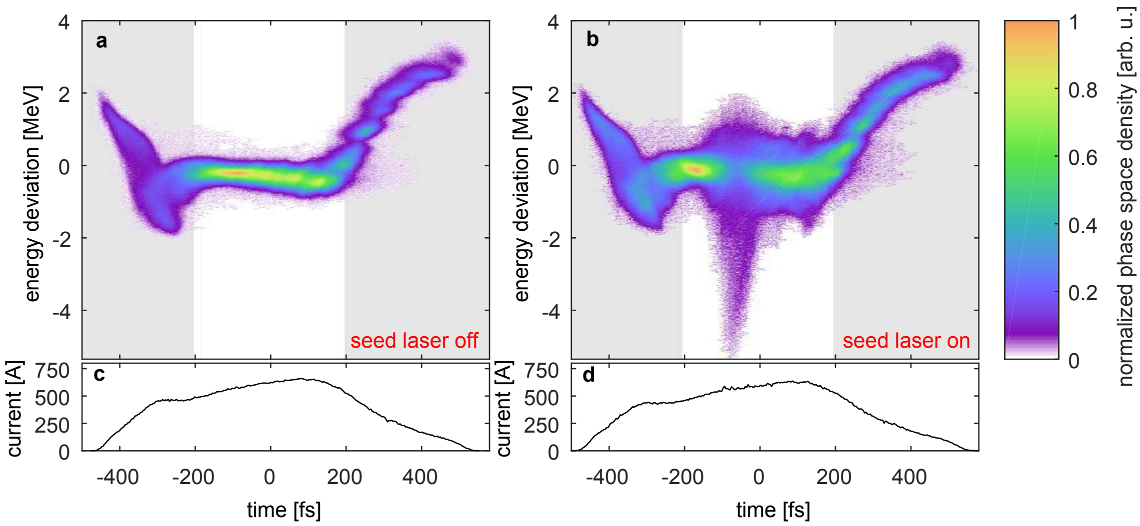

Figure 4.2.: Measurement of the longitudinal phase space distribution downstream of the radiator. The x-axes show the intra-bunch coordinate (time) with respect to the charge center-of-mass, the head of the bunch is located on the left. The y-axes show the energy deviation from the mean energy. Color coded is the phase space density. Panel *(a)* shows shows an electron bunch that was not seeded, panel *(b)* shows a seeded electron bunch close to FEL saturation. Panels *(c)* and *(d)* show the respective current profiles. In the subsequent plots, only the core region (white background) between $-200\,\mathrm{fs}$ and $+200\,\mathrm{fs}$ that supports FEL lasing will be shown. Reprinted with permission by Scientific Reports under Creative Commons Attribution 4.0 International License [63].

both zero crossings of the rf phase to be

$$S_\mathrm{y} = (4.172 \pm 0.065)\,\frac{\mathrm{\mu m}}{\mathrm{fs}}, \tag{4.3}$$

where the error was found from the two measurements using a maximum likelihood method. Sometimes a dimensionless shear parameter $S_\mathrm{y,dl}$ is given that differs from the one given here by a factor of c. The dimensionless the shear parameter was $S_\mathrm{y,dl} = 13.91 \pm 0.22$.

Though the deflection is caused by a magnetic field, it is commonly described by a virtual voltage V_0 that can be calculated from the shear parameter S_y [64]:

$$V_0 = \frac{S_\mathrm{y,dl} W c^2}{\omega e R_{34}} = (11.7 \pm 0.2)\,\mathrm{MV}, \tag{4.4}$$

where ω is the circular frequency of the deflecting rf field, W the kinetic energy of the electrons, e the elementary charge and R_{34} the matrix element of the linear beam transfer matrix from the center of the cavity to the observation screen that describes how an angle (kick) of the electrons evolves into an offset from the design orbit. R_{34} is explicitly given by the electron optics in place during the experiment, the remaining parameters are measured and give the error on the virtual voltage V_0.

A typical measurement of the longitudinal phase space distribution is shown in Fig. 4.2. The left panel shows the phase space distribution of an electron bunch that was not seeded and the right one shows a seeded electron bunch. The time coordinate on the x-axis is given with respect to the center-of-mass of the charge distribution, unless otherwise noted. It can be seen, that the seeding process has significant impact on the phase space distribution once the seeded FEL is close to saturation. This effect will be explored below in Section 4.3.

In this chapter, local characteristics of the electron bunch (e.g. emittance or energy spread) that change along its longitudinal profile will be studied. These local properties will be referred to as slice properties, since they are only given for a longitudinal slice of the electron bunch. A slice typically contains a few periods of the seed laser period of $\lambda_{\mathrm{seed}} = 266\,\mathrm{nm}$. Quantities that describe the complete bunch often are referred to as projected, e.g. projected emittance.

4.1. Initial Correlation

As mentioned above, the incoming bunch can exhibit an initial correlation between the y and t coordinates, leading to different bunch lengths measured on both slopes of the deflecting TDS rf field. In one case, the streaking compensates for the initial correlation, in the other case an enhancing effect takes place. To correct for this initial correlation, one measures the beam size on both slopes ($\sigma_{\pm}$) and for no deflecting field ($\sigma_{\mathrm{y},0}$). The three beam sizes are then given by [65]

$$\sigma_{\mathrm{y},\pm} = \sqrt{\sigma_{\mathrm{y,i}}^2 + (C_{\mathrm{y}} \pm |S_{\mathrm{y}}|)^2 \sigma_{\mathrm{t}}^2}, \quad \sigma_{\mathrm{y},0} = \sqrt{\sigma_{\mathrm{y,i}}^2 + C_{\mathrm{y}}^2 \sigma_{\mathrm{t}}^2}, \tag{4.5}$$

where $\sigma_{\mathrm{y,i}}$ is the intrinsic beam size without any spatio-temporal correlation and σ_{t} is the bunch duration. With these three measurements, one can determine the initial correlation parameter C_{y} and the intrinsic beam size $\sigma_{\mathrm{y,i}}$ by either fitting the dependence on S_{y} or by analytical means. Figure 4.3 shows the measurements as well as a fit of Eq. (4.5) to the data. The calculated parameters are

$$C_{\mathrm{y}} = (0.42 \pm 0.07)\,\mathrm{\mu m/fs}, \tag{4.6a}$$
$$\sigma_{\mathrm{t}} = (207.6 \pm 3.2)\,\mathrm{fs}, \tag{4.6b}$$
$$\sigma_{\mathrm{y,i}} = 126.5\,\mathrm{\mu m}, \tag{4.6c}$$

where the errors are propagated from the measurement error on S_{y}. Since $\sigma_{\mathrm{y,i}}$ is independent of S_{y} we cannot give an error estimation on the intrinsic beam size.

Note that this analysis assumes a Gaussian longitudinal bunch profile. The fact that the actual profile might deviate from a Gaussian introduces a further error source which is not taken into account.

4.2. Resolution Limits

The finite beam size of the electron beam on the screen will impact the resolution of the measurement. The observed electron phase space distribution will be a convolution of the

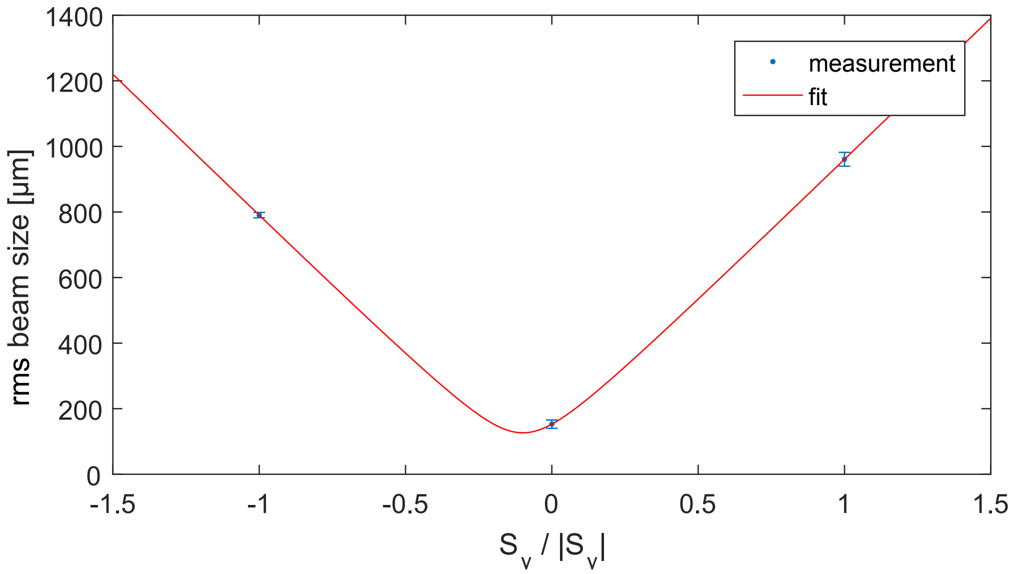

Figure 4.3.: Measurement of vertical rms beam size on observation screen for negative normalized streaking amplitude (σ_-), for positive streaking amplitude (σ_+) and without streaking voltage ($\sigma_{\mathrm{y},0}$). The red line shows a fit of Eq. (4.5).

real distribution and a Gaussian resolution function. The vertical rms resolution (corresponding to the time axis of the measurement) can be determined using the parameters calculated in the preceding section [64]

$$\mathcal{R}_{\mathrm{t,proj},\pm} = \frac{\sigma_{\mathrm{y,i}}}{|C_{\mathrm{y}} \pm |S_{\mathrm{y}}||} \tag{4.7}$$

$$\mathcal{R}_{\mathrm{t,proj},-} = 33.6\,\mathrm{fs} \qquad \mathcal{R}_{\mathrm{t,proj},+} = 27.5\,\mathrm{fs}$$

For the measurements presented during this section, the flank with the smaller resolution has been chosen. This calculation, however, uses beam size and thus projected emittance of the electron bunch to estimate the resolution in both time and energy. The local resolution is determined by the slice emittance of the bunch. The normalized projected emittance in the y-plane was measured during optics matching procedures at $\epsilon_{\mathrm{y,n}} = (3.4\pm0.2)\,\mathrm{mm\,mrad}$. As will be shown later, the slice emittance in the high-current core region of the bunch is about $\epsilon_{\mathrm{y,n}} = 1.0\,\mathrm{mm\,mrad}$. The slice beam size is thus smaller than the projected beam size by a factor of about $\sqrt{3.4/1} \approx 1.85$, assuming no mismatch along the beam because of collective effects. The local resolution of the measurements in the high-current region is thus smaller by the same factor and can be estimated to be

$$\mathcal{R}_{\mathrm{t}} \approx 14.9\,\mathrm{fs}. \tag{4.8}$$

When examining the raw data images, structures with a distance of about 15 fs can be distinguished from each other suggesting that this value is indeed closer to the actual resolution than the one given before.

The energy-resolution cannot be measured that easily and has to be estimated from the smallest structures visible on the observation screen. Under the assumption that for these structures the resolution is dominating the measurement one can estimate an upper limit. With this, the rms-resolution during the presented measurements has been estimated at

$$\mathcal{R}_{\mathrm{E}} \leq 170\,\mathrm{keV}. \tag{4.9}$$

Note that since the resolution – as well as other effects that deteriorate the measurement – are symmetric effects, the uncertainty of mean values like the mean electron energy for example, is smaller than this resolution.

4.3. Extraction of FEL Power Profile

As shown in Fig. 4.2 the FEL process has a significant impact on the longitudinal phase space distribution of the electron bunch. On average, the electrons contributing to the FEL process lose energy to the light field as can be observed in the measurement. This energy loss can be used to extract the FEL pulse profile from the longitudinal phase space distribution of the electron beam.

Note that not only the mean energy of the electron slices changes, but also the energy spread increases. While the electrons lose energy on average, some electrons still gain energy from the light field as shown in Fig. 2.1 (p. 9) and increase the slice energy spread. The FEL process, however, is not the only effect influencing the energy spread of the electron bunch. With the coherent structures that are imprinted on the electron bunch, longitudinal space charge forces will also affect the energy spread. This effect will briefly be discussed in Sec. 5.2. Thus, while the energy spread increase due to the FEL process also contains information on the pulse profile, it is difficult to filter the growth in energy spread caused by other effects.

Hence, the pulse profiles shown in this chapter will be extracted from the loss in the mean energy of the seeded electron bunch when compared to the non-seeded reference bunch. The FEL pulse profile can then be extracted from the principle of energy conservation [62, 65]:

$$P_{\mathrm{FEL}}(t) = \left(W_{\mathrm{ref}}(t) - W_{\mathrm{seed}}(t)\right) I(t)/e = \Delta W(t)\, I(t)/e, \tag{4.10}$$

where $W_{\mathrm{ref}}(t)$ is the mean slice energy of the reference bunch, $W_{\mathrm{seed}}(t)$ the mean slice energy of a seeded bunch and $I(t)$ the current profile. Unless otherwise noted, parameters that are a function of the intra-bunch coordinate t denote slice parameters during this chapter.

To obtain the reference profiles, a series of 50-150 images of unseeded electron bunches is acquired within one to two hours before the measurement. This excludes changes in the state of the machine that might have an influence on the bunch slope. The slice parameters of these shots are then averaged to obtain $W_{\mathrm{ref}}(t)$, $I(t)$, and the energy spread profile. From this averaging also the statistical errors on the slice parameters can be calculated and will be used to estimate uncertainties on derived properties.

Figure 4.4 illustrates the capabilities of the discussed single-shot analysis technique. The power profile was extracted from the measured longitudinal phase space distribution shown using Eq. (4.10). The signal that is generated in the head and the tail of the pulse is induced by instabilities in the accelerating rf and by the image processing. Thus, also negative powers can result from this evaluation. For robust data analysis, a Gaussian is

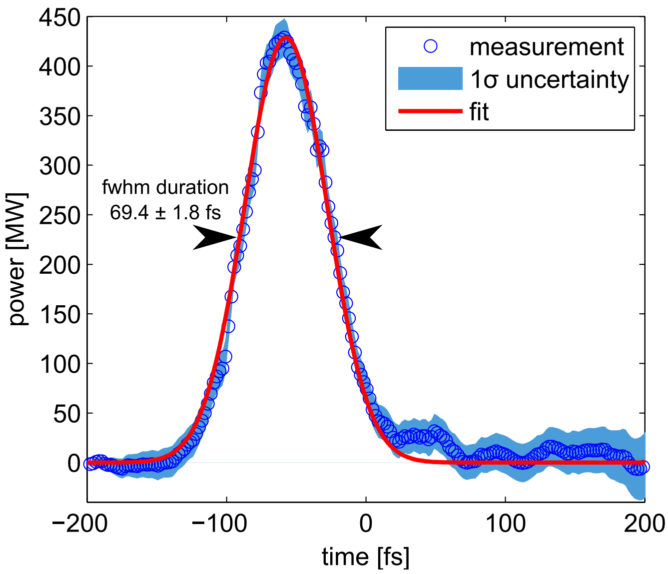

Figure 4.4.: Reconstruction of a single shot FEL pulse power profile using Eq. (4.10). The x-axis shows the time with respect to the charge center-of-mass of the lasing electron bunch. The blue circles show the reconstruction, the red curve shows a Gaussian fit with a peak power of $P_0 = 429\,\mathrm{MW}$ and a duration of $\Delta\tau = 69.4\,\mathrm{fs}$ full width at half maximum. This corresponds to a photon pulse energy of about $32\,\mu\mathrm{J}$. The shaded blue area shows the rms variation of the data derived from statistical errors of the reference bunches. Reprinted with permission by Scientific Reports under Creative Commons Attribution 4.0 International License [63].

Reason	Count	Percentage [%]
data acquisition system	71	1.9
image processing	1684	44.5
camera hardware	31	0.8
rf fluctuations	45	1.2
fitting procedure	280	7.4
total	2111	55.8

Table 4.1.: Data processing challenges with the amount of data discarded due to several issues. A detailed description of the reasons can be found in the text.

fitted to the central peak. The chosen fit function plotted in red is a Gaussian with a fixed amplitude P_0 set to the maximum of the data. The fit parameters are the rms duration σ_t and the position of the central peak μ:

$$P(t) = P_0 \exp\left(-\frac{(t-\mu)^2}{2\sigma_\mathrm{t}^2}\right). \tag{4.11}$$

In order to obtain a good fit, the full width at half maximum of the peak Δt with the maximum signal along the electron bunch has been determined. The fit was then conducted over a region of $3\Delta t$ centered around the peak signal. This approach, however, only works for power profiles with a dominant lasing feature.

As described above, this method may suffer from instabilities and image processing that can generate false features in the power profiles in the order of several tens of MW. The following analysis excludes all shots with peak powers smaller than 100 MW in order to avoid confusions of these features with a signal resulting from the seeding process.

The energy of the FEL pulse can be obtained by integrating over the longitudinal power profile. In case of the Gaussian fits the integral can be calculated analytically

$$E = \int_{-\infty}^{\infty} P(t)\mathrm{d}t = \sqrt{2\pi}\, P_0\, \sigma_\mathrm{t} = \frac{\sqrt{\pi}}{2\sqrt{\ln 2}} P_0\, \Delta\tau, \tag{4.12}$$

where $\Delta\tau = 2\sqrt{2\ln 2}\,\sigma_\mathrm{t}$ is the fwhm duration of the photon pulse.

4.3.1. Data Selection Process

For every seeded electron bunch, the observation screen of the TDS setup is imaged by a camera (see Fig. 4.1). For various reasons, however, not every image contains useful information. To illustrate this, the dataset evaluated in Sec. 4.6 (total 3784 shots) is classified into several categories. An overview can be found in Table 4.1. The following list gives a description of the encountered issues and the amount of data lost accordingly:

- During the specified data series 71 shots (1.9%) have been lost due to the performance of the data acquisition system.

- A total of 1684 (44.5%) shots have been rejected due to image processing challenges. The extracted peak power is below the threshold of 100 MW. Automatic reconstruction of the pulse profile becomes challenging, since the features cannot be distinguished from false signal induced by image processing or jitter in the accelerating rf. The amount of data in this category will strongly differ from data series to data series. Since this series is one where laser-electron timing was scanned, there are parts of the scan hitting regions of the bunch that do almost not lase, amounting to plenty of data in this category.

- Some of the images cannot be evaluated due to hardware problems with the camera imaging the observation screen. A total of 31 (0.8%) shots fall into this category.

- For 45 shots (1.2%) no central lasing feature could be found. There are features that induce a signal that is higher than the threshold of 100 MW, but features induced by jitter of the accelerating rf and cutting process are larger than the amplitude induced by the lasing process. No unique feature can be identified as the FEL feature with absolute certainty.

- A similar issue causes the Gaussian fits of the remaining shots to have a wrong baseline. A goodness-of-fit method has been applied which discards 280 (7.4%) shots out.

In the end the data series provides 1673 (44.2%) shots where the reconstruction of the FEL power profiles was successful.

4.4. Calibration of Photon Energy Detectors

A second independent measurement of the energy can be obtained by a micro-channel plate (MCP) installed in the photon diagnostic section of the sFLASH experiment. Its exponential amplification process is controlled by the so-called gain voltage. During the experiment that provided the data for the presented analysis, the MCP had to be operated at low gain voltages (down to 600V) in order to cover the complete range of generated energies. The MCP, however, was originally calibrated for gain voltages of 1000-1300 V. An extrapolation of the calibration to the used gain voltages increases the measurement error significantly. Measured energies are easily overestimated by a factor of about 10.

The extraction of FEL pulse power profiles enables to determine a calibration constant for a specific gain setting of the MCP, by correlating its raw signal with the energies extracted from the profiles.

Fig. 4.5 shows the correlation of the MCP raw signal and the energy extracted from the reconstructed FEL pulse profiles for a gain voltage of 650 V. The red curve shows a linear fit to the data, the grey area shows the 3σ uncertainty of the fit. The calibration constant was determined to be $m_{650\,\mathrm{V}} = (0.982 \pm 0.004) \cdot 10^4 \mathrm{V/J}$.

With a calibration of the MCP one has access to a bigger amount of data: The data set resulting from the TDS-based analysis does not contain information for every shot, as discussed above. The MCP, by contrast acquires data for every single bunch.

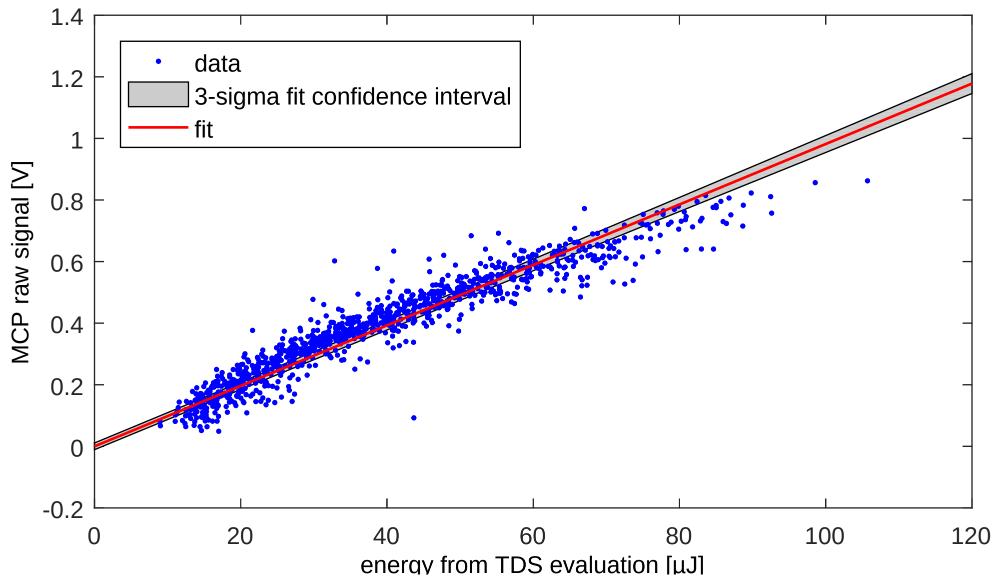

Figure 4.5.: Correlation of MCP raw signal and energy from TDS evaluation for a gain voltage of 650V. The red curve shows a fit to the blue data points. The grey area shows the 3σ uncertainty of the fit.

4.5. Extraction of Slice Emittance from Measured Energy Spread Profiles

From the measurement of the reference bunches the slice energy spread and current of the electron bunch can be measured. With a proper model of the electron beamline the influence of transverse optics and heating effects of the TDS can be studied and a slice emittance can be extracted from the measurement. The measured slice energy spread $\sigma_{\mathrm{W,m}}(t)$ is composed of three contributions [66]

$$\sigma^2_{\mathrm{W,m}}(t) = \sigma^2_{\mathrm{W,0}}(t) + \sigma^2_{\mathrm{W,g}}(t) + \sigma^2_{\mathrm{W,PW}}(t), \tag{4.13}$$

where $\sigma_{\mathrm{W,0}}(t)$ is the initial energy spread of the electron bunch, $\sigma_{\mathrm{W,g}}(t)$ the geometric contribution from the beam size on the screen, and $\sigma_{\mathrm{W,PW}}(t)$ is the increase of the energy spread due to the Panofsky-Wenzel effect. Here Gaussian contributions of the individual contributions are assumed. Errors arising from deviations of the profiles from a Gaussian will not be treated.

The initial slice energy spread is known to be a function of the slice current, since it is induced by the compression process in the bunch compressors in the linear accelerator. At FLASH the estimate for the slice energy spead is given by [67]

$$\sigma_{\mathrm{W,0}}(t) = 100\,\frac{\mathrm{keV}}{\mathrm{kA}} \cdot I_{\mathrm{peak}}. \tag{4.14}$$

This estimation is well in line with numerical simulations along the core region of the electron bunch. For high peak currents, collective effects get stronger and a deviation from this estimate will become larger. In any case one needs an estimate of the energy spread profile along the electron bunch in order to apply the method shown here.

The geometrical contribution is determined by the transverse beamsize of the electron bunch on the observation screen. We can write this contribution as

$$\sigma_{\mathrm{W,g}}(t) = A \cdot W(t) \cdot \sigma_{\mathrm{x}}(t) = A \cdot W(t) \cdot \sqrt{\frac{\epsilon_{\mathrm{x,n}}(t)\,\beta_{\mathrm{x}}}{\gamma(t)}} = A \cdot m_0 c^2 \sqrt{\epsilon_{\mathrm{x,n}}(t)\,\beta_{\mathrm{x}}\,\gamma(t)}, \quad (4.15)$$

where β_{x} is the slice beta function in the x-plane and $\epsilon_{\mathrm{x,n}}(t)$ is the slice emittance in the x-plane. The parameter A is the calibration constant of the camera image that converts transverse beam sizes to energy.

The Panofsky-Wenzel heating of the beam is given by [68, 69]

$$\sigma_{\mathrm{W,PW}}(t) = K \cdot W(t) \cdot \sigma_{\mathrm{y}}(t) = K \cdot m_0 c^2 \sqrt{\epsilon_{\mathrm{y,n}}(t)\,\beta_{\mathrm{y}}\,\gamma(t)}, \quad (4.16)$$

where $K = \frac{eV_0 k}{pc}$, k is the wave number of the deflecting rf field, p the momentum of the electrons, β_{y} is the local beta function in the y-plane and $\epsilon_{\mathrm{y,n}}(t)$ is the normalized slice emittance in the y-plane.

Assuming a symmetric beam for the moment, we can set $\epsilon_{\mathrm{x,n}}(t) = \epsilon_{\mathrm{y,n}}(t) = \epsilon_{\mathrm{n}}(t)$. A more detailed discussion of this assumption is given in Section 4.6.1. Now the last two contributions of (4.13) can be summarized

$$\sigma^2_{\mathrm{W,g}}(t) + \sigma^2_{\mathrm{W,PW}}(t) = \underbrace{(A^2\beta_{\mathrm{x}} + K^2\beta_{\mathrm{y}})\,\gamma(t)\,(m_0c^2)^2}_{\xi}\,\epsilon_{\mathrm{n}}(t) = \xi\epsilon_{\mathrm{n}}(t). \quad (4.17)$$

Note that ξ can be calculated, since A and K are known, $\gamma(t)$ can be extracted from TDS measurements and β_{x} and β_{y} can be found by simulation with the particle tracking code ELEGANT [70] using a measurement of the optics and knowledge of the magnet settings during the experiment.

To find the slice emittance we can now rearrange (4.13) and use (4.17) to end up with

$$\epsilon_{\mathrm{n}}(t) = \frac{\sigma^2_{\mathrm{W,m}}(t) - \sigma^2_{\mathrm{W,0}}(t)}{\xi}. \quad (4.18)$$

Fig. 4.6 shows the measured energy spread as well as the reconstructed emittance ϵ_{n}. The colored area shows the statistical rms uncertainty of the measurement for the energy spread and the rms uncertainty of the calculated emittance derived by Gaussian error propagation. With knowledge of the slice emittance and current profile, the projected emittance can be calculated to be $\epsilon_{\mathrm{n,proj}} = (3.0 \pm 0.3)$ mm mrad, well in line with the the value $\epsilon_{\mathrm{n,match}} = (3.4 \pm 0.2)$ mm mrad obtained during the optics matching procedure.

4.6. Longitudinal Scan of Electron Bunch

To find the longitudinal position in the bunch that is best suited for seeding and generates highest output powers, the relative seed laser electron timing is scanned. Fig. 4.7 shows a histogram of the correlation of the laser pulse position with respect to the charge center-of-mass and the peak power of the FEL pulse. The distribution shows a total of 1979 shots and is smoothed by a Gaussian with an rms width of one pixel. As described above,

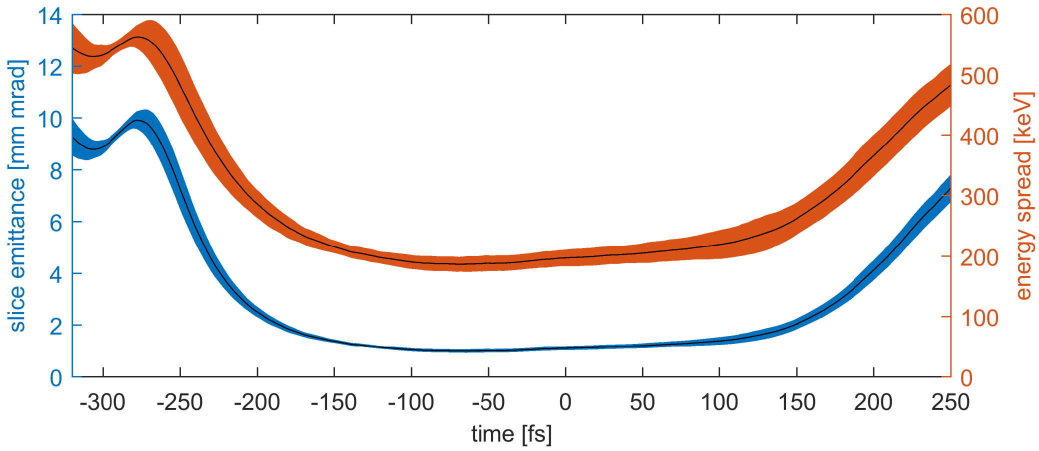

Figure 4.6.: Measured slice energy spread of non-seeded reference bunches (orange) and reconstructed slice emittance profile (blue). The colored areas indicate the rms uncertainties of the corresponding parameter. Reprinted with permission by Scientific Reports under Creative Commons Attribution 4.0 International License [63].

the evaluation disregards shots with peak powers below 100 MW. The jitter of the laser-electron timing strongly benefits this method, since the longitudinal scan is much more fine. If the fluctuations would vanish, there were only the discrete laser-electron timing steps of the scan, while the jitter increases the longitudinal range that a single scan step can cover.

The red line in Fig. 4.7 shows an average for every time bin. It is important to note that the center of mass of the tails of the distribution is subject to systematic errors: As described above, the evaluation disregards shots with small output powers, so the average power values in these bins might be too high.

The extraction of the slice parameters presented in the preceding section now enables the calculation of the FEL performance for each slice of the bunch. For this prediction, the one-dimensional FEL theory is extended by the universal Ming Xie scaling function to determine the three-dimensional gain length L_{g}, Pierce parameter ρ, and saturation power P_{sat} as described in Sec. 2.3. The gain curve can then be described by the solution of the third-order differential equation of the FEL with an initial current modulation given in Eq. (3.9) (p. 23). In the presented experiment the undulator parmeter was tuned so the FEL process radiates at the 7th harmonic of the seed laser. Thus, the peak power of the FEL pulse expected after a certain undulator length is thus a function of ρ, L_{g}, the beam power P_{beam}, and the initial bunching b_7. The first three parameters can be calculated from experimental data, while the bunching factor will be a fit parameter for the model.

By varying the initial bunching b_7 this analytical estimation has been fitted to the average of each timing bin of Fig. 4.7 using a χ^2-fit. The uncertainties of the data points are only statistical errors and do not include any systematic errors, e.g. from calibration of the longitudinal phase space measurement. The scan shown in Fig. 4.7 was binned to 31 time bins, the central 21 of which have been used for the fitting procedure (-125 to

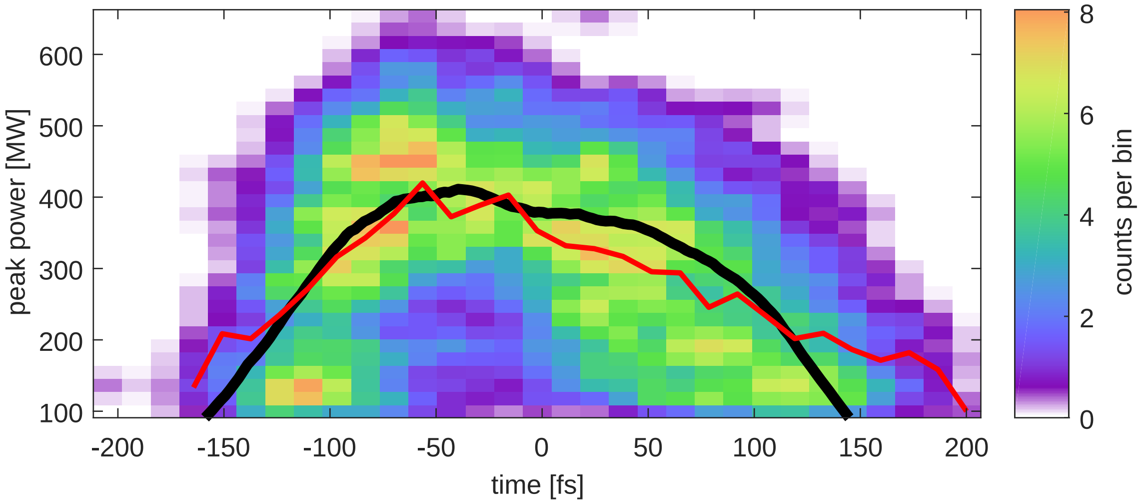

Figure 4.7.: 2-dimensional histogram of laser-electron timing scan smoothed by a Gaussian with an rms width of one pixel. The y-axis shows the peak power of the shots, the x-axis the position of the Gaussian peak. The red line shows the mean of every time bin, the black line shows the prediction of the analytic FEL model discussed in the text. Reprinted with permission by Scientific Reports under Creative Commons Attribution 4.0 International License [63].

+125 fs). The reduced χ^2 of the fit is about 3.8, indicating a possible underestimation of the error bars.

The result of the fit is indicated as a black line in Fig 4.7, showing the prediction for FEL peak powers after 6.4 m of effective undulator length and a modulation amplitude of $\Delta\gamma = 0.777 \pm 0.001$, corresponding to an initial bunching factor of $b_7 = (3.22 \pm 0.03) \cdot 10^{-2}$, determind by a χ^2 fit over the core region. The effective undulator length used here is smaller than the 10 m undulator available. The reason for this is discussed in the next chapter.

Using this method, the performance of the seeded FEL can be predicted from the measurements of unseeded reference bunches, and the laser-electron timing for optimum FEL performance can be found without a time scan.

4.6.1. Uncertainties on Emittance Prediction

The Ming-Xie formalism used to estimate the FEL performance takes the normalized one-dimensional emittance as a parameter. An upper estimate for this emittance is the geometric mean of the transverse emittances $\epsilon_{\mathrm{mx}}(t) = \sqrt{\epsilon_{\mathrm{n,x}}(t)\epsilon_{\mathrm{n,y}}(t)}$ [71]. The previous sections only gave statistical errors on $\epsilon_{\mathrm{n}}(t)$ derived from the measured energy spread and demanding that both transverse emittances are the same. This section focuses on uncertainties arising if the transverse emittances are not equal or if the electrons experience strong collective effects introducing mismatches along the bunch.

To allow the emittances in both planes to deviate from one another, we will introduce the scaling parameter u and define the emittances for an arbitrary slice in both transverse

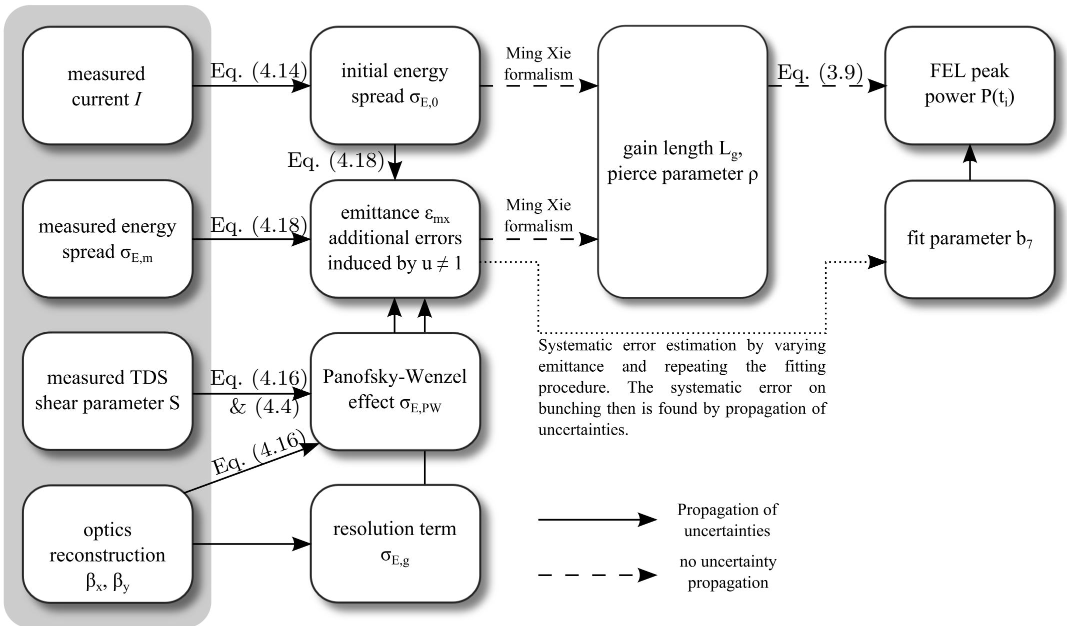

Figure 4.8.: Calculations and propagations of uncertainties for the different stages of the model. The notes above the arrows give information about calculation of parameters, the line style of the arrows shows if an uncertainty is propagated. The grey shaded area groups the measurements.

planes as

$$\epsilon_{\mathrm{x,n}} = \epsilon_{\mathrm{n}} \text{ and } \epsilon_{\mathrm{y,n}} = u\epsilon_{\mathrm{n}}, \tag{4.19}$$

leading to

$$\xi = (K^2\beta_{\mathrm{y}}u + A^2\beta_{\mathrm{x}})\gamma m_0^2 c^4. \tag{4.20}$$

To identify parameters that are affected by uncertainties we have to analyze the full expression for the one-dimensional emittance using Eq. (4.18)

$$\epsilon_{\mathrm{mx}}(t_i) = \epsilon_{\mathrm{n}}\sqrt{u} = \frac{\sigma_{\mathrm{W,m}}^2 - \sigma_{\mathrm{W,0}}^2}{(K^2\beta_{\mathrm{y}}u + A^2\beta_{\mathrm{x}})\gamma m_0^2 c^4}\sqrt{u}. \tag{4.21}$$

The parameters that are subject to statistical measurement errors are the measured slice energy spread $\sigma_{\mathrm{W,m}}$, the initial energy spread $\sigma_{\mathrm{W,0}}$ (from the current measurement), and the rf deflector kick parameter K. As discussed above, u can deviate from 1, if the transverse emittances are not equal, and β_{x} and β_{y} can differ from the optical functions of the accelerator. An overview of the measured parameters, the calculations and the error propagation of the model can be found in Fig. 4.8.

The combined uncertainty on $\epsilon_{\mathrm{mx}}(t)$ is found by propagation of the uncertainties of all six uncertain parameters. For a more convenient notation we will drop the (t) from the emittance terms and introduce for this section only $\Sigma^2 := (\sigma_{\mathrm{W,m}}^2 - \sigma_{\mathrm{W,0}}^2)$.

$$\begin{aligned}
\sigma_{\epsilon_{\mathrm{mx}}}^2 = & \left(\frac{\partial\epsilon_{\mathrm{mx}}}{\partial\sigma_{\mathrm{W,m}}}\right)^2 \mathrm{Var}(\sigma_{\mathrm{W,m}}) + \left(\frac{\partial\epsilon_{\mathrm{mx}}}{\partial\sigma_{\mathrm{W,0}}}\right)^2 \mathrm{Var}(\sigma_{\mathrm{W,0}}) \\
& + \left(\frac{\partial\epsilon_{\mathrm{mx}}}{\partial\beta_{\mathrm{x}}}\right)^2 \mathrm{Var}(\beta_{\mathrm{x}}) + \left(\frac{\partial\epsilon_{\mathrm{mx}}}{\partial\beta_{\mathrm{y}}}\right)^2 \mathrm{Var}(\beta_{\mathrm{y}}) \\
& + \left(\frac{\partial\epsilon_{\mathrm{mx}}}{\partial u}\right)^2 \mathrm{Var}(u) + \left(\frac{\partial\epsilon_{\mathrm{mx}}}{\partial K}\right)^2 \mathrm{Var}(K)
\end{aligned} \tag{4.22}$$

The partial derivatives are calculated to be:

$$\frac{\partial\epsilon_{\mathrm{mx}}}{\partial\sigma_{\mathrm{W,m}}} = \frac{1}{\gamma m_0^2 c^4}\frac{2\sqrt{u}}{A^2\beta_{\mathrm{x}} + K^2\beta_{\mathrm{y}}u}\sigma_{\mathrm{W,m}} = 6.2851 \cdot 10^{-17}\,\tfrac{\mathrm{m}}{\mathrm{eV}^2} \cdot \sigma_{\mathrm{W,m}} \tag{4.23a}$$

$$\frac{\partial\epsilon_{\mathrm{mx}}}{\partial\sigma_{\mathrm{W,0}}} = -\frac{1}{\gamma m_0^2 c^4}\frac{2\sqrt{u}}{A^2\beta_{\mathrm{x}} + K^2\beta_{\mathrm{y}}u}\sigma_{\mathrm{W,0}} = -6.2851 \cdot 10^{-17}\,\tfrac{\mathrm{m}}{\mathrm{eV}^2} \cdot \sigma_{\mathrm{W,0}} \tag{4.23b}$$

$$\frac{\partial\epsilon_{\mathrm{mx}}}{\partial\beta_{\mathrm{x}}} = -\frac{1}{\gamma m_0^2 c^4}\frac{A^2\sqrt{u}}{(A^2\beta_{\mathrm{x}} + K^2\beta_{\mathrm{y}}u)^2}\Sigma^2 = -0.0428 \cdot 10^{-17}\,\tfrac{1}{\mathrm{eV}^2} \cdot \Sigma^2 \tag{4.23c}$$

$$\frac{\partial\epsilon_{\mathrm{mx}}}{\partial\beta_{\mathrm{y}}} = -\frac{1}{\gamma m_0^2 c^4}\frac{K^2\sqrt{u}}{(A^2\beta_{\mathrm{x}} + K^2\beta_{\mathrm{y}}u)^2}\Sigma^2 = -0.0371 \cdot 10^{-17}\,\tfrac{1}{\mathrm{eV}^2} \cdot \Sigma^2 \tag{4.23d}$$

$$\begin{aligned}
\frac{\partial\epsilon_{\mathrm{mx}}}{\partial u} &= \frac{1}{\gamma m_0^2 c^4}\left(-\frac{\beta_{\mathrm{y}}K^2\sqrt{u}}{(A^2\beta_{\mathrm{x}} + K^2\beta_{\mathrm{y}}u)^2} + \frac{1}{2\sqrt{u}(A^2\beta_{\mathrm{x}} + K^2\beta_{\mathrm{y}}u)}\right)\Sigma^2 \\
&= -0.8856 \cdot 10^{-17}\,\tfrac{\mathrm{m}}{\mathrm{eV}^2}\Sigma^2
\end{aligned} \tag{4.23e}$$

$$\frac{\partial\epsilon_{\mathrm{mx}}}{\partial K} = -\frac{1}{\gamma m_0^2 c^4}\frac{2\beta_{\mathrm{y}}K\sqrt{u^3}}{(A^2\beta_{\mathrm{x}} + K^2\beta_{\mathrm{y}}u)^2}\Sigma^2 = -1.3427 \cdot 10^{-17}\,\tfrac{\mathrm{m}^2}{\mathrm{eV}^2}\Sigma^2 \tag{4.23f}$$

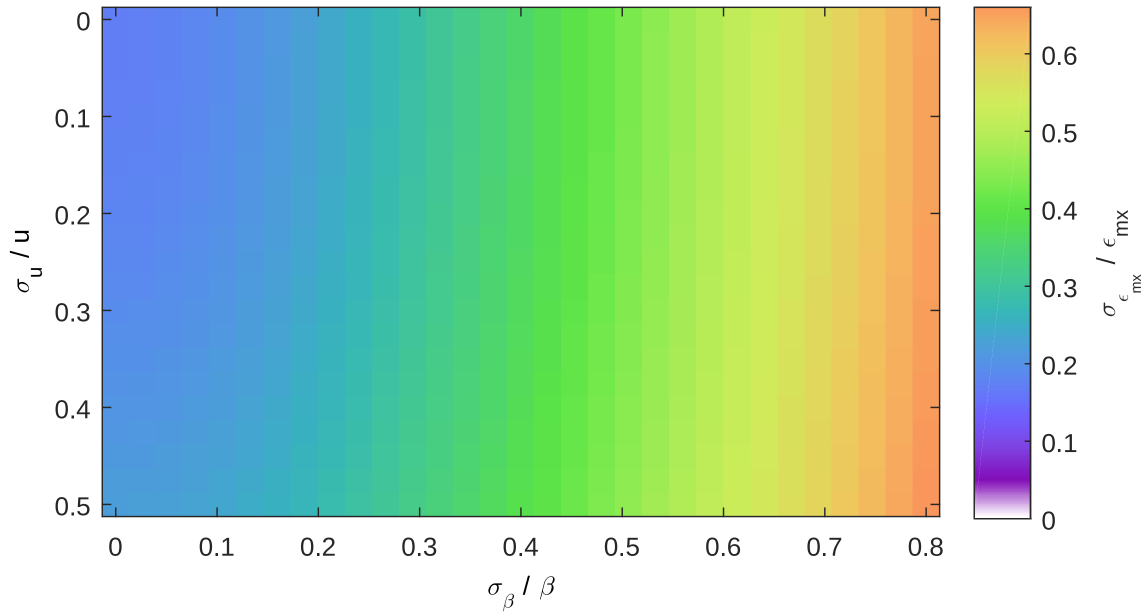

Figure 4.9.: Estimated error on calculated emittance ϵ_{mx} (color coded) as a function of the error on u and β_{x}, β_{y}.

While the uncertainties of $\sigma_{\mathrm{W,m}}$, $\sigma_{\mathrm{W,0}}$ and K are known from the statistical uncertainties from the measurements, the uncertainties of the β-functions and u have to be estimated, since single-shot TDS measurements do not give access to these values and dedicated measurements have not been performed. Start-to-end simulations of similar bunches have shown that the emittances in the transverse planes are equal down to a few percent. Also the mismatch due to collective effects is below $\sigma_\beta/\beta < 0.1$ within the central regions of the bunch for both planes. Figure 4.9 shows the relative emittance error as a function of σ_β/β and σ_{u}/u.

The propagation shows, that the relative error of ϵ_{mx} is about 17% if the initial assumptions about the emittances and optical functions are correct ($\sigma_{\mathrm{u}} = 0$ and $\sigma_\beta = 0$). Since both quantities can only be estimated from numerical simulations, we will use a conservative estimation of $\sigma_{\epsilon_{\mathrm{mx}}}/\epsilon_{\mathrm{mx}} = 0.3$ in the following.

4.6.2. Error Discussion of Performance Prediction

As discussed above the emittance is used to predict the FEL performance. The initial modulation amplitude or bunching factor is the free parameter of the model and is used to fit the prediction to the data. An uncertainty of the emittance will change the prediction of the model only little. If the emittance would be slightly different, another modulation amplitude would yield a similar prediction for the FEL power. An uncertainty in the emittance can thus be treated as a systematic error on the fit parameter [72].

To estimate the error, the fit procedure described earlier was done for different emittance values within ±15% of the emittance derived in Sec. 4.5. The resulting best-fit values for the modulation amplitude then show a function of emittance. The systematic error on the modulation amplitude is found by propagation of uncertainties to be

$$\sigma^2_{\Delta\gamma,\mathrm{sys}} = \left(\frac{\partial \Delta\gamma}{\partial \epsilon_{\mathrm{mx}}}\right)^2 \sigma^2_{\epsilon_{\mathrm{mx}}}. \tag{4.24}$$

With a relative emittance error of 30%, as estimated in the preceding section, the systematic errors on the modulation amplitude and bunching are $\sigma_{\Delta\gamma,\mathrm{sys}} = 0.154$ and $\sigma_{\mathrm{b,sys}} = 1.70$, respectively. In summary, with the fit parameters given above:

$$\Delta\gamma = 0.777 \pm 0.001_{\mathrm{stat}} \pm 0.154_{\mathrm{sys}}, \tag{4.25}$$

$$b_7 = (3.22 \pm 0.03_{\mathrm{stat}} \pm 1.70_{\mathrm{sys}}) \cdot 10^{-2}. \tag{4.26}$$

The uncertainties discussed in the last two sections arise, since the mismatch along the bunch as well as the differences in transverse emittances were not known during the experimental campaign. A dedicated measurement of the emittance, e.g. using a quadrupole in combination with the TDS can eliminate these uncertainties.

4.7. Summary

An rf deflector installed downstream of the radiator is the optimum tool to extract the FEL photon pulse profile without absorbing any of its energy. If the peak power exceeds 100 MW, the profiles can be extracted with a time-resolution of 15 fs from the drop in mean energy that is caused by the FEL radiation process.

The data set, however, is sufficient to calibrate the micro-channel plate that measures the energy of the generated photon pulses. This allows access to a higher base of energy measurements since the data sorting algorithm of thes TDS evaluation rejects between 20% and 55% of the data.

The rf deflector does not only provide information on FEL photon pulses, but also offers a simple derivation of the slice emittance under the assumption of a compression dominated electron energy spread. The derived electron slice properties can be used to determine the seeded performance as a function of the longitudinal intra-bunch coordinate. In this way HGHG seeding can be used as a local probe to verify the prediction and thus the extracted slice emittance. The fitted modulation amplitude is found to be well in line with the modulation amplitude extracted from a measurement of the uncompressed electron beam. Possible error sources have been studied and give the systematic errors on the modulation amplitude.

Though the estimation of the energy spread needed for this method and a mismatch caused by collective effects can strongly increase the uncertainty of the emittance estimation, this method is suited for the analysis of moderately compressed electron bunches used with soft x-ray FEL seeding. With software upgrades it could in principle be deployed as a single-shot on-line diagnostic for the preparation of the electron bunch for optimum FEL output.

Though the setup of the rf deflector measurement has been conducted thoroughly, a smaller beta function could increase the temporal resolution of the measurement by a factor of 2-3. This could be achieved with a FODO channel along the sFLASH radiator, in contrast to the special optics used during the experiments, where these quadrupoles where shut off. The photon pulses that can be measured with this method have to exceed the temporal resolution of the measurement. Thus, a further optimization of the experimental setup could decrease the minimum pulse length required for the measurement.

5. Characterization of the HGHG Process at sFLASH

After the hardware setup of the HGHG experiment was described in the previous chapter, this section mainly focuses on the presentation and discussion of the experimental results. The measurements presented were primarily taken during an experimental campaign in January 2016 unless noted otherwise in the specific sections.

The characteristics that have to be known in order to understand and discuss the results of the seeding experiment, are the kinetic energy W_0 of the electron bunch, its current profile, the optical functions of the accelerator and the transverse beam sizes of the seed laser along the beam propagation direction.

The electron energy was measured with standard techniques using the position of the electron beam on a beam position monitor within a dispersive section of the beamline. It was determined to be $W_0 = 685\,\mathrm{MeV}$. Errors on this measurement have been briefly discussed in Sec. 3.7. The beam current profile as shown in Fig. 5.1 has been measured using the transverse deflector described in chapter 4.

The laser beam size cannot be measured at the point of interaction, but only on the two Ce:YAG screens in front and after the modulating undulator. The measured beam sizes are given in Table 5.1. The laser spot on the 6ORS screen shows a secondary laser spot alongside its main spot, that carries a significant amount of the power. This leads to the high uncertainty of the measurements. Since most theoretical models assume a symmetrical and round laser beam, we will use the average $\sigma_\mathrm{l} = (262 \pm 24)\,\mathrm{\mu m}$ of the measured beamsizes on both screens for these purposes.

The electron beam optical functions have been measured with a four-screen-method. In this method, the electron beam sizes are measured on four screens in the region of the sFLASH radiator. Since the emittance stays constant, the optical functions as well as a projected emittance can be derived from these measurements [73]. Table 5.2 gives an overview over the reconstructed optics and measured projected emittance at 10ORS. The given errors are uncertainties of the fitting procedure. Fig. 5.2 shows the reconstructed optics along the beamline. For the purposes of the analysis these optical functions can be used to reconstruct the optics throughout the complete sFLASH section.

screen	$\sigma_{\mathrm{x,l}}$ [µm]	$\sigma_{\mathrm{y,l}}$ [µm]
6ORS	428 ± 87	251 ± 36
10ORS	181 ± 5	187 ± 6

Table 5.1.: Seed laser rms beam sizes on Ce:YAG screens. The mean rms sizes and standard deviations for 1305 shots are given.

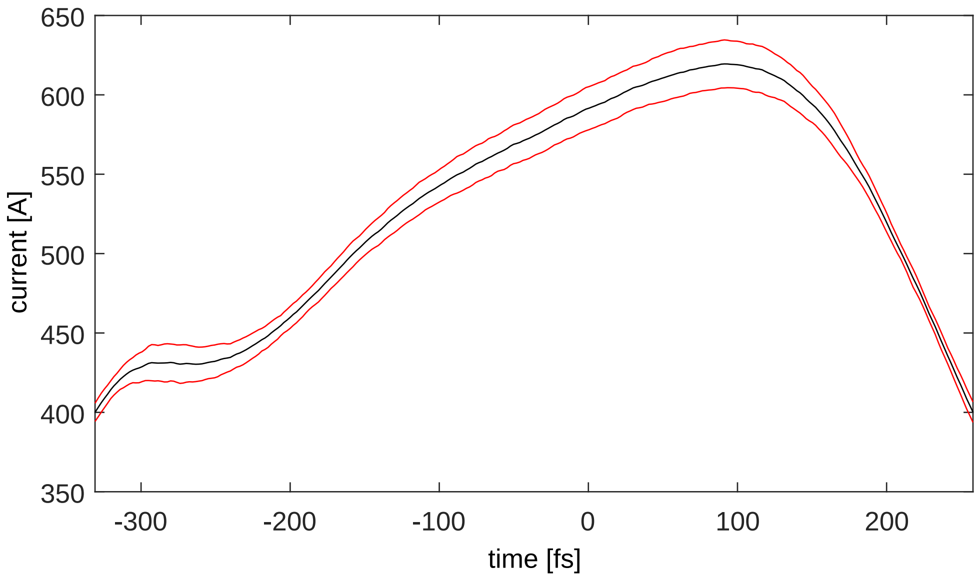

Figure 5.1.: The mean current of the electron bunch averaged over 150 shots is shown in black. The red lines show the 1σ uncertainties derived from the statistical fluctuations of the 150 shots.

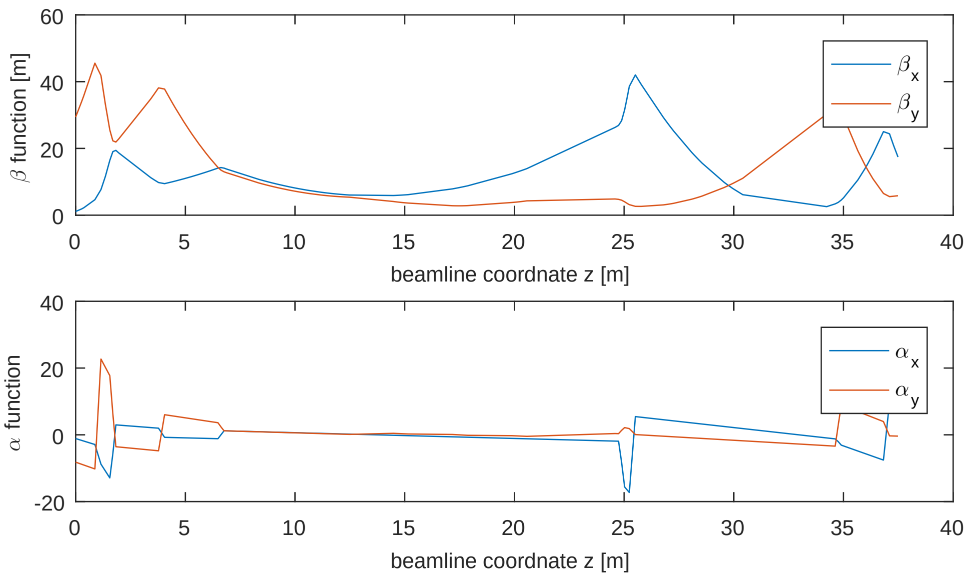

Figure 5.2.: Reconstruction of the electron beam optics.

plane	β [m]	α	ϵ_n [µm]
x	6.4 ± 0.3	0.84 ± 0.09	3.8 ± 0.2
y	14.8 ± 0.8	1.32 ± 0.10	3.1 ± 0.2

Table 5.2.: Reconstructed electron beam optics at the position of the 10ORS screen.

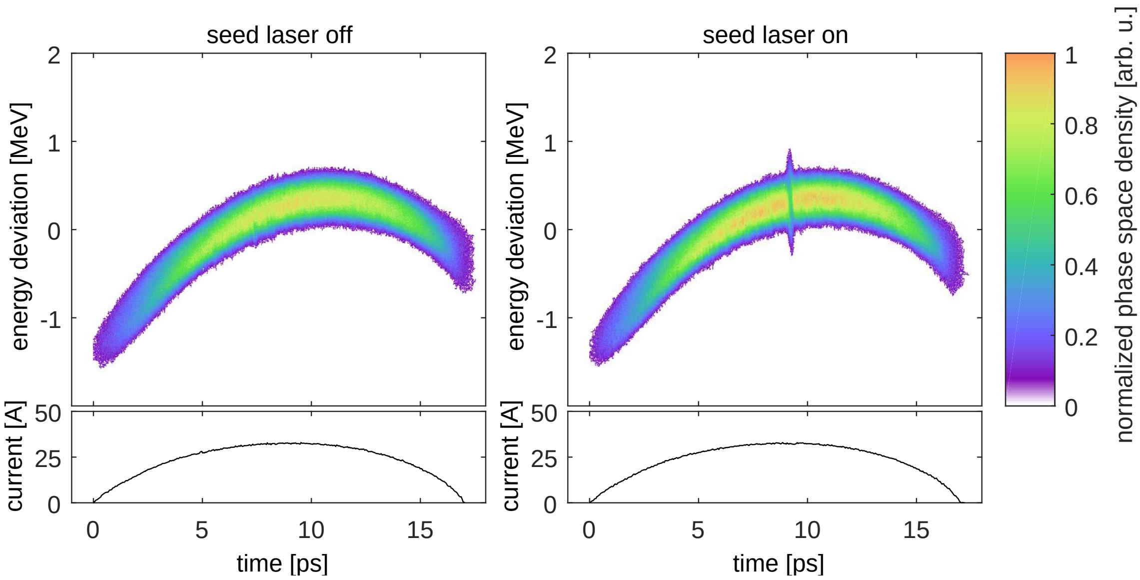

Figure 5.3.: The longitudinal phase space and current of uncompressed electron bunches. The left column shows the plots for an unmodulated electron bunch, the right one shows a modulated phase space and the corresponding current.

5.1. Modulation Amplitude

A first measurement of the longitudinal phase space of the uncompressed electron bunch can give an estimation of the induced energy modulation. To extract the induced energy modulation, the measured energy spread of a modulated and unmodulated bunch are compared. The difference is the seed laser induced energy modulation $\Delta\gamma$. With Eq. (3.3) we can quickly derive

$$\Delta\gamma = \sqrt{2\left(\sigma^2_{\mathrm{W,seed}} - \sigma^2_{\mathrm{W,ref}}\right)}, \tag{5.1}$$

where $\sigma_{\mathrm{W,seed}}$ is the measured rms energy spread of the modulated electron bunch and $\sigma_{\mathrm{W,ref}}$ is the one for the unmodulated reference bunch. Using the example of two typical longitudinal phase space distributions as shown in Fig. 5.3, the laser induced modulation amplitude can be extracted and is shown in Fig. 5.4. Because of the limitations of peak calculations imposed by the low signal-to-noise ration, a Gaussian fit is used to extract the peak modulation amplitude. From a data series of 1091 shots the peak modulation amplitude can on average be estimated to be

$$\Delta\gamma_{\mathrm{peak}} = 0.79 \pm 0.09. \tag{5.2}$$

The given error is the statistical uncertainty. Since the evaluation process includes an algorithm that cuts parts of the longitudinal phase space distribution with very small densities to compensate for camera noise, the modulation amplitude above rather specifies a lower limit and the full energy modulation can be even larger.

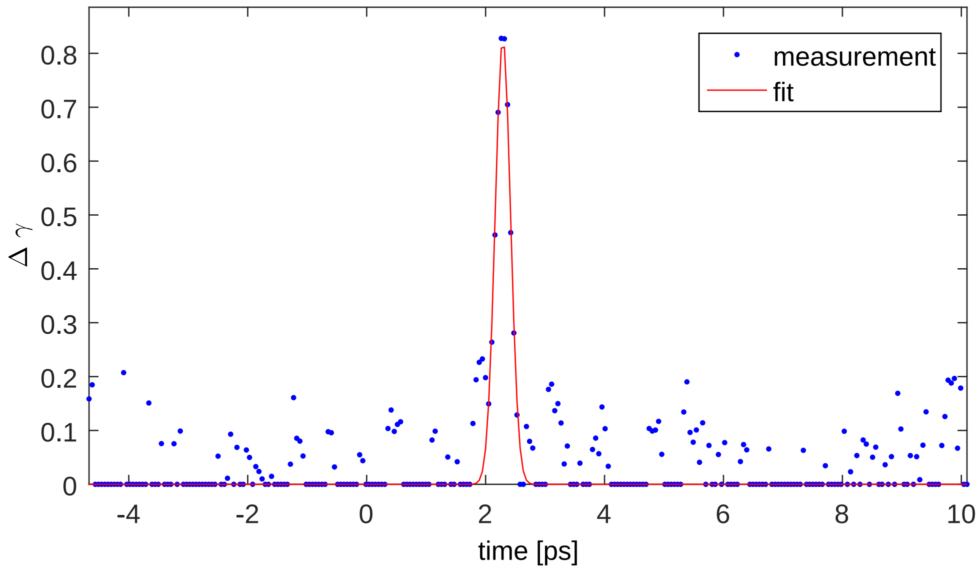

Figure 5.4.: Single shot measurement of the induced modulation amplitude calculated with Eq. (5.1). Even though the signal-to-noise ratio is low, the height of the central peak can easily be extracted by a Gaussian fit. Note, that the time coordinate in this plot is given with respect to the leftmost particle.

5.2. FEL Gain Curve

In order to analyze the FEL process and to find the characterizing pierce parameter ρ, an energy gain curve of the FEL has been measured. Since the sFLASH radiator is comprised of four independent undulator modules, the energy of the FEL pulse after 2 m, 4 m, 6 m and 10 m of active undulator length can be assessed. The energy measurements have been conducted with the installed MCP and the transverse deflector as described in chapter 4.

Figure 5.5 shows the gain curve for different seed laser powers. The seed laser power which is denoted in the captions of the figure is not directly measured but derived from the modulation amplitude that was fitted in section 4.6 and the measured seed laser beam size using Eq. (3.2). The blue data points are measured using the MCP that was calibrated using rf deflector data as described in section 4.4. The red data points show MCP measurements for a different gain voltage (800 V). Here, peak powers are well below 100 MW and a direct calibration with the TDS is not possible. Instead the measurements for 4 m active undulator length at 100 MW input seed power has been conducted with 2 different gain voltages (650 V, 800 V) and a comparison of the both data series gives the calibration of the red data points. The given errors on the points are the standard deviations from averaging over several hundreds of shots. For all data points the highest and lowest 10% of the data points have been disregarded, since the variation of the signal is mainly attributed to jitter of the modulating laser power. The exclusion of these outliers reduces the standard deviation of the data points significantly by a factor of 2-3 while the mean of the measurement is unaffected. An exponential function has been fitted to the 2, 4 and 6 m data points in order to extract the gain length.

In all three gain length measurements, the measurement after the fourth undulator does

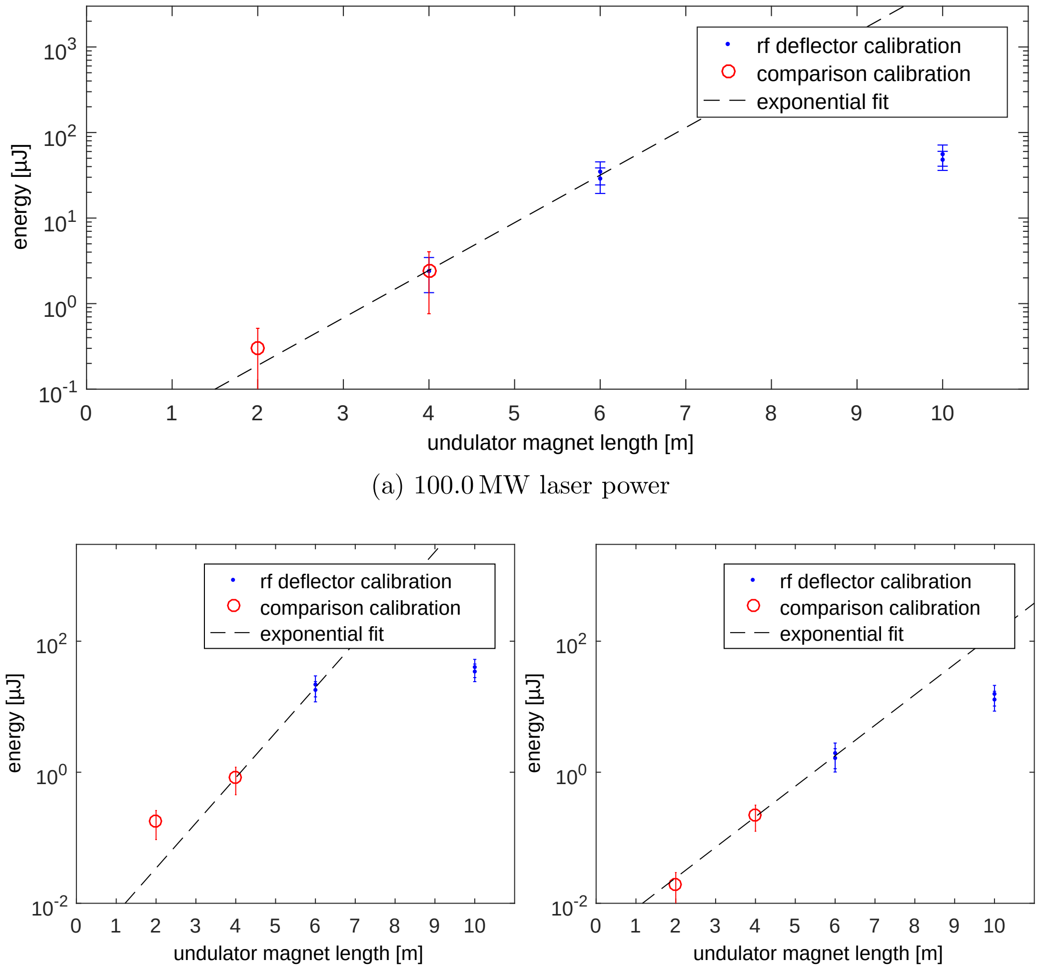

(a) 100.0 MW laser power

(b) 81.5 MW laser power

(c) 64.5 MW laser power

Figure 5.5.: Gain curve measurements for different seed laser powers. The dashed lines shows an exponential fit to the first three data points.

laser power	L_{g} [m]	ρ $[10^{-3}]$	L_4/L_{g}
100.0 MW	0.78 ± 0.12	1.85 ± 0.28	0.49 ± 0.29
81.5 MW	0.63 ± 0.25	2.29 ± 0.91	0.63 ± 0.33
64.5 MW	0.93 ± 0.21	1.55 ± 0.35	2.07 ± 0.37

Table 5.3.: Fitted gain length for the gain curves measured with different seed laser powers.

not coincide with the fitted gain curve anymore. With only one gain curve measurement this could be interpreted as a saturation effect. However, the disagreement between the last measured data point and the exponential gain curve persists through measurements with less initial laser power and hence less initial bunching. According to the model one expects in such cases the last data point to be much closer to the exponential gain curve. The fact that it does not, strongly indicates another effect taking place that inhibits further gain. Another argument against a saturation effect is the Gaussian shape of the longitudinal power profile of the photon pulse that can be observed by the rf deflector in chapter 4. A deeply saturated seeded FEL photon pulse is likely to show a plateau in its temporal center where more and more slices reach saturation.

To further investigate this effect we will, as a first step, calculate the apparent length L_4 of the last radiator segment in which the FEL process still exponentially gains power in terms of gain lengths:

$$\frac{L_4}{L_{\mathrm{g}}} = \ln\left(\frac{P_4}{P_3}\right) = \ln\left(\frac{E_4}{E_3}\right), \tag{5.3}$$

where P_{n} is the power generated after n radiator modules and E_{n} is the corresponding energy. The second equal sign assumes that the last radiator segment does not change the photon pulse duration significantly as verified by TDS measurements.

Table 5.3 summarizes the gain lengths from the fits in Fig. 5.5. Though the fit for 81.5 MW shows large errors, the fits for the other two cases agree within their 1σ error intervals. The last column shows the amount of gain lengths traversed in the last undulator segment L_4/L_{g}, where the errors are propagated from the energy measurements E_3 and E_4.

Thus, from the measurement of the gain curve, two questions arise: Why does the last undulator not contribute as expected and does not drive the FEL process into saturation? And: Why does the amount of gain length traversed in the last undulator depend on the initial seed laser amplitude?

The answer to both questions can be found in longitudinal space-charge (LSC) forces of the coherent structures imprinted by the laser-electron interaction and the dispersive strength $R_{56} = -50\,\mu\mathrm{m}$ of the chicane. The fundamental process works very similar to the physics driving microbunching instabilities as described in [75, 76, 77]. As discussed earlier, this setup point did not reach optimum bunching of the electrons. Instead, when considering one period of modulation, the distribution is left in a state where the maximum of the sinusoidal energy modulation slope trails the current spike, while the minimum is upfront as depicted in Fig. 5.6a. The longitudinal space-charge forces push electrons away from the current spike. Trailing electrons lose energy while leading ones gain energy. Due to this evolution, the energy spread reaches a minimum as shown in Fig. 5.6b a

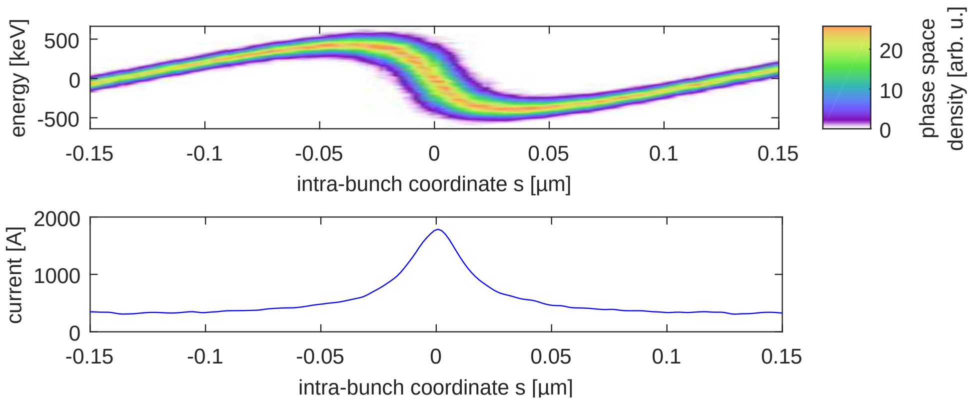

(a) Longitudinal phase space distribution after the chicane. The longitudinal space-charge forces start to decrease the energy spread: Because of the central current peak, trailing electrons lose energy and leading electrons gain energy.

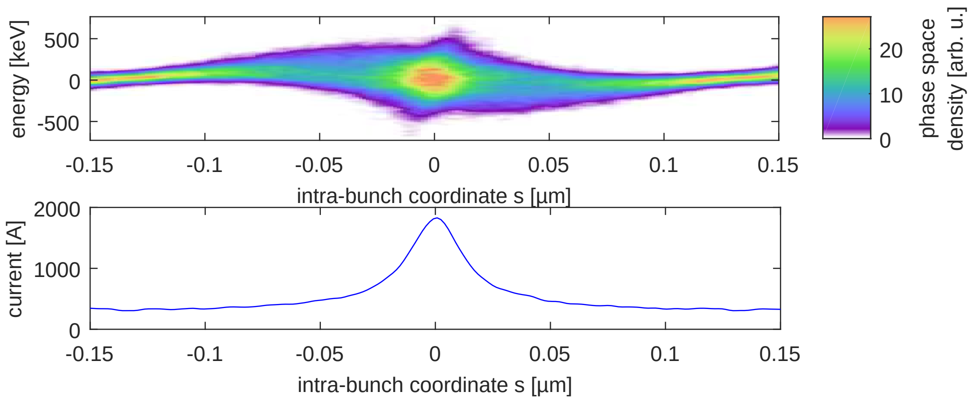

(b) Longitudinal phase space distribution at the position of minimum energy spread.

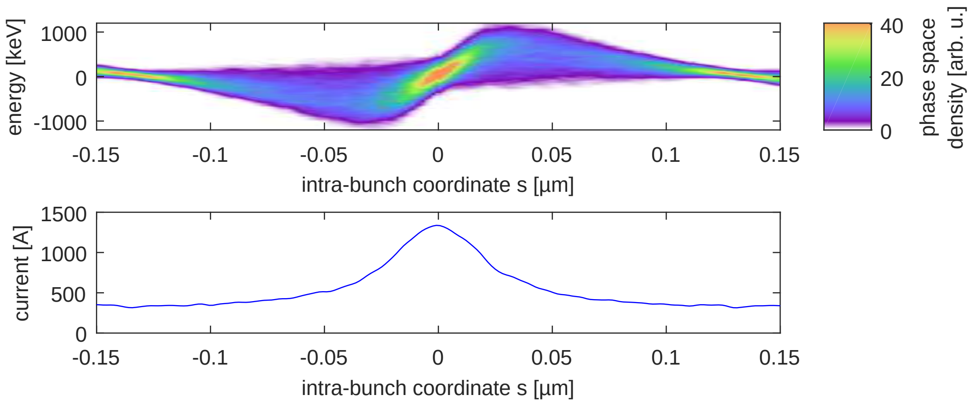

(c) Longitudinal phase space distribution after 20 m of evolution. The total energy spread has increased again and exceeds the modulation amplitude imprinted by the HGHG process.

Figure 5.6.: Evolution of the longitudinal phase space distribution of the electron bunch under the influence of longitudinal space-charge forces for a modulation amplitude of $\Delta\gamma = 0.8$ at different positions along a drift space (see Fig. 5.7): *(a)* after the chicane. *(b)* at the position where the energy spread reaches its minimum, and *(c)* 20 m after the chicane. The direction of motion of the electron bunch is from left to right. This simulation has been conducted with QFIELD (see text).

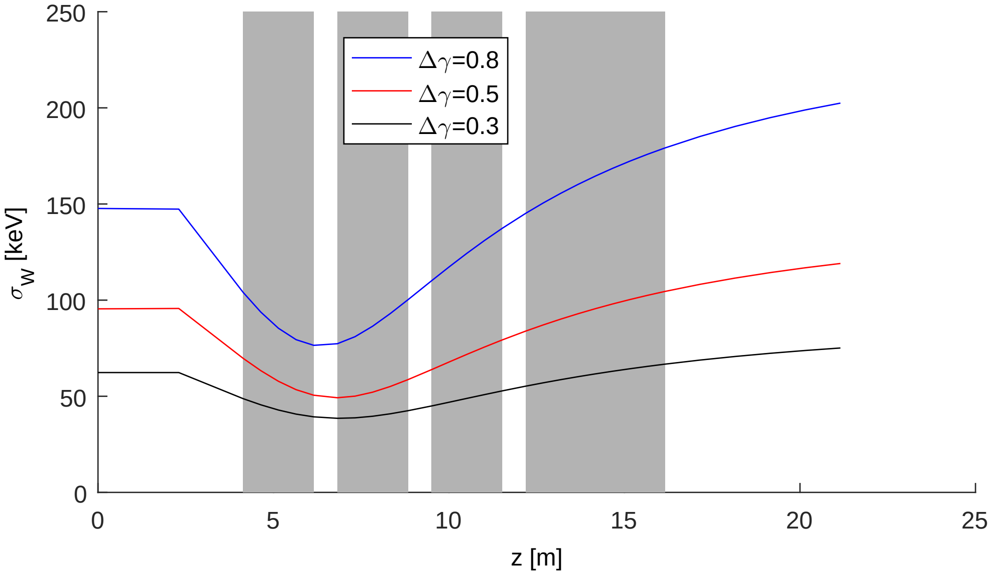

Figure 5.7.: Evolution of rms slice energy spread σ_W of the modulated electron bunch along a drift space for different modulation amplitudes [74]. The simulation has been conducted with QFIELD and tracks one modulation period under the assumption of periodic continuation. Though there is no undulator incorporated into the simulations, the grey boxes indicate the positions of the sFLASH undulator segments.

couple of meters after the chicane. Since there still is a strong maximum in the current distribution, the the longitudinal space-charge fields still act on the electrons and the evolution continues. The energy spread increases again. Fig. 5.6c shows the longitudinal phase space distribution 20,m after the chicane.

Figure 5.7 shows a simulation of the evolution of the rms slice energy spread σ_W of the electron beam along a drift space. The simulation has been conducted with the three-dimensional periodic space charge solver QFIELD [78]. This code tracks one period of modulation under the assumption of periodic continuation. Thus, the energy spread given in the figure is averaged over one period of modulation. The chicane, implemented by a transfer matrix, at about 2.3 m converts the sinusoidal energy modulation into a density modulation. The LSC-driven evolution of the longitudinal phase space sets in. In Fig. 5.7, the change of the rms slice energy spread is more rapid for higher modulation amplitudes. Its final value is larger for larger initial modulation amplitudes. It should be noted that the longitudinal space-charge fields are stronger when the electron bunch traverses the undulator compared to a drift space and the evolution of the energy spread is expected to be faster [79]. However, a full-scale simulation of the electron bunch traversing the undulator is challenging and beyond the scope of this thesis.

While the LSC effects decrease the energy spread for the first undulator segments the effect on the FEL process is only small, because it is mainly dominated by the emittance in this regime. In the last segment, it becomes high enough to decrease the gain and may even lead to a premature saturation effect. This effect will not be studied any further

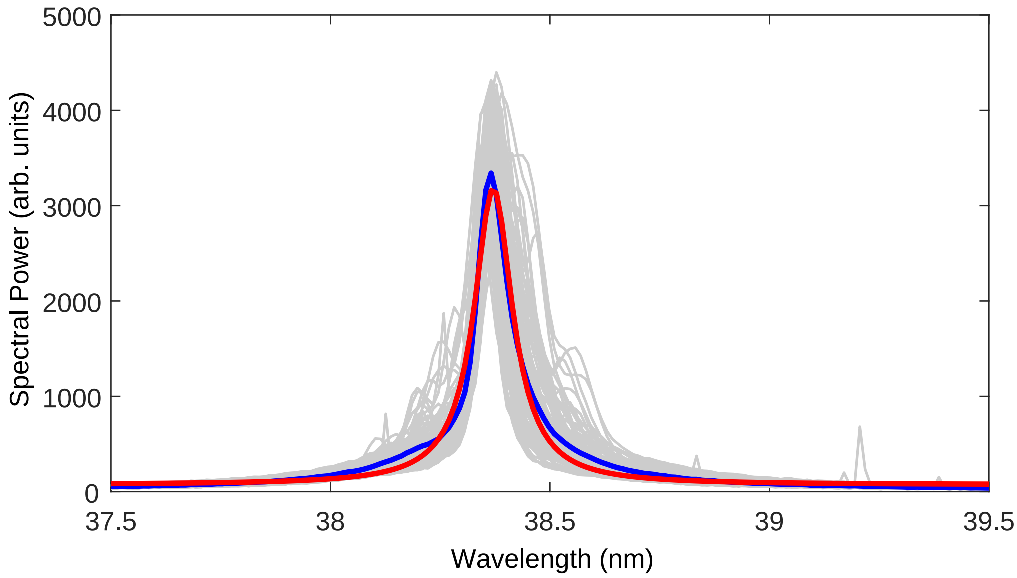

Figure 5.8.: The single-shot spectra of 270 FEL pulses are shown in grey. The blue line shows an averaged spectrum of these shots, the red line a Lorentzian fitted to the averaged curve.

in this thesis, but instead all gain curves and pulse power properties predicted by the Ming-Xie model or numerical simulations will be evaluated after an undulator length of

$$z_{\mathrm{p}} = 6\,\mathrm{m} + \left(\frac{L_4}{L_{\mathrm{g}}}\right) L_{\mathrm{g}}, \tag{5.4}$$

where 6 m is the total magnetic length of the first three modules. Note that this is only the distance traversed in the undulator. Numerical simulations usually include drift spaces between undulators and z_{p} has to be adapted.

5.3. Spectrum of FEL Pulse

The spectra of the FEL photon pulses have been taken using a commercially available spectrometer[1] with a slit width of 30 µm. Figure 5.8 shows 270 single-shot spectra as well as an averaged spectrum of 2300 consecutive shots. The averaged spectrum does not resemble a Gaussian, but shows the wider base of a Lorentz distribution. The resolving power R of the spectrometer as given by the data sheet is

$$R = \left(\frac{\lambda}{\Delta\lambda}\right)_{\mathrm{res}} \approx 642. \tag{5.5}$$

Fig. 5.9 shows a histogram of the inverse relative width of Lorentzian fits to 3260 consecutive single-shot spectra. The red line shows a Gaussian fit to the histogram with its center at $\left(\frac{\lambda}{\Delta\lambda}\right)_{\mathrm{meas}} \approx 400$. The inverse spectral width $\left(\frac{\lambda}{\Delta\lambda}\right)_{\mathrm{th}}$ expected from numerical

[1] McPherson, Model 248/310 UHV

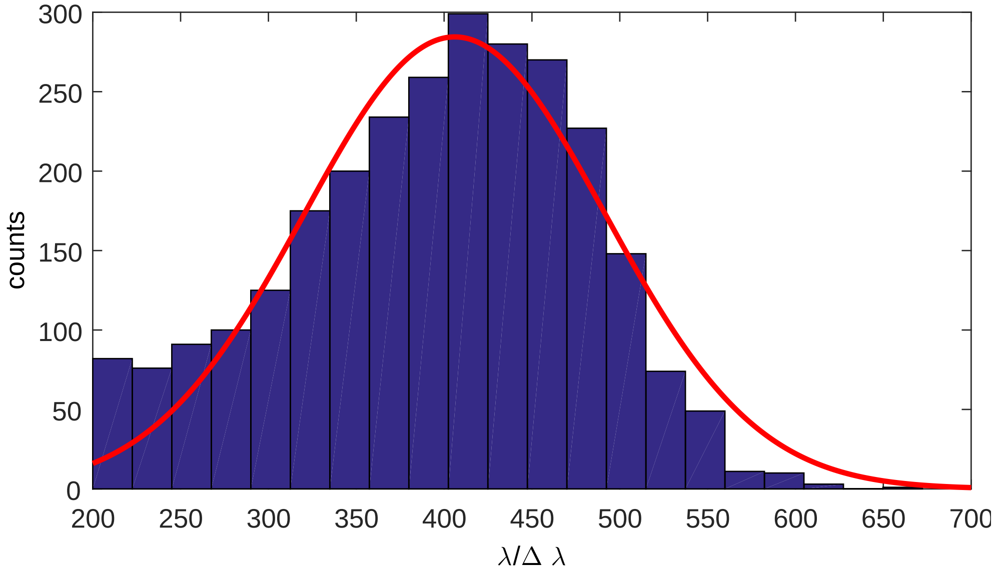

Figure 5.9.: Histogram of inverse relative spectral width of 3260 shots. The red line shows a Gaussian fit to the data with its peak at 400. The theoretical resolving power of the spectrometer is $R \approx 640$.

simulation is about 1300 as discussed in Section 5.5. Given this expected width, $\left(\frac{\lambda}{\Delta\lambda}\right)_{\mathrm{meas}}$ should be in the range of 550, close to its resolution limit.

Thus, the measured spectral width and the expected theoretical width are not compatible with the resolving power given before. Since the spectrometer was not aligned during the shift, it is, however, likely that the resolving power is worse than measured before its installation. In this case, a lot of the measurements are limited by resolving power of the spectrometer and only an upper limit rather than the precise spectral width can be extracted from the measurements. The upper limit is derived from the center of a Gaussian fit to the histogram and amounts to

$$\left(\frac{\Delta\lambda}{\lambda}\right)_{\mathrm{meas}} \leq 2.5 \cdot 10^{-3}. \tag{5.6}$$

5.4. Pulse Length Measurement

An analysis of uncompressed electron bunches that were modulated does not only allow the extraction of the peak modulation amplitude, but also contains information on the seed laser pulse duration. As described in chapter 3, the modulation amplitude $\Delta\gamma$ is proportional to the electrical field of the seed laser. The seed pulse duration, however, is defined as the rms duration of the pulse power profile. Since the seed laser power $P_{\mathrm{L}} \propto E^2$, the duration of the electrical field $\sigma_{\mathrm{t,E}}$ (and thus modulation amplitude envelope) and $\sigma_{\mathrm{t,l}}$ are related by:

$$\sigma_{\mathrm{t,l}} = \sigma_{\mathrm{t,E}}/\sqrt{2}. \tag{5.7}$$

The duration of the modulation amplitude envelope can easily be extracted from the evaluation of the modulation amplitude shown in Section 5.1. Figure 5.10 shows a histogram

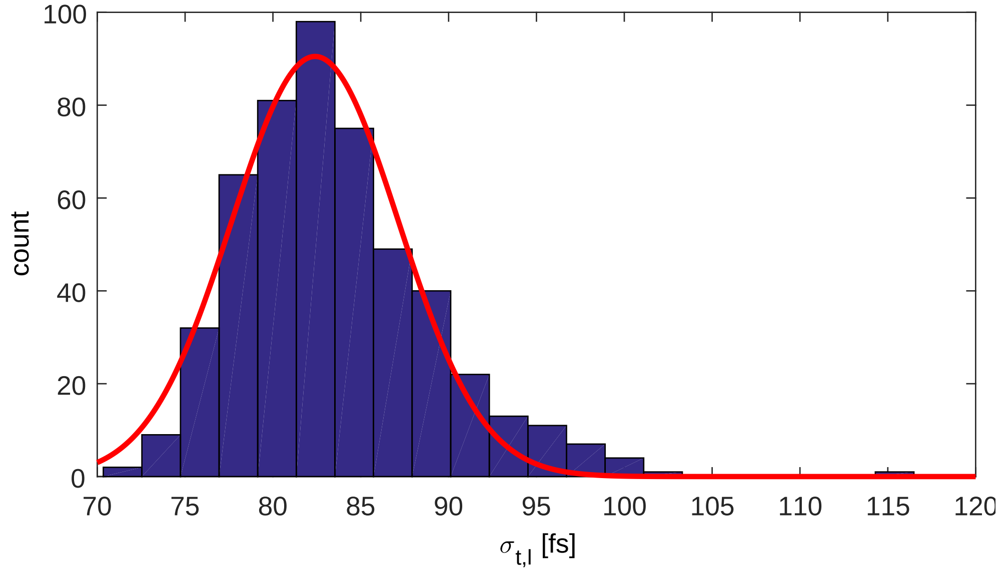

Figure 5.10.: Histogram of seed laser pulse durations extracted from 590 consecutive shots. The red line shows a Gaussian fit to the histogram.

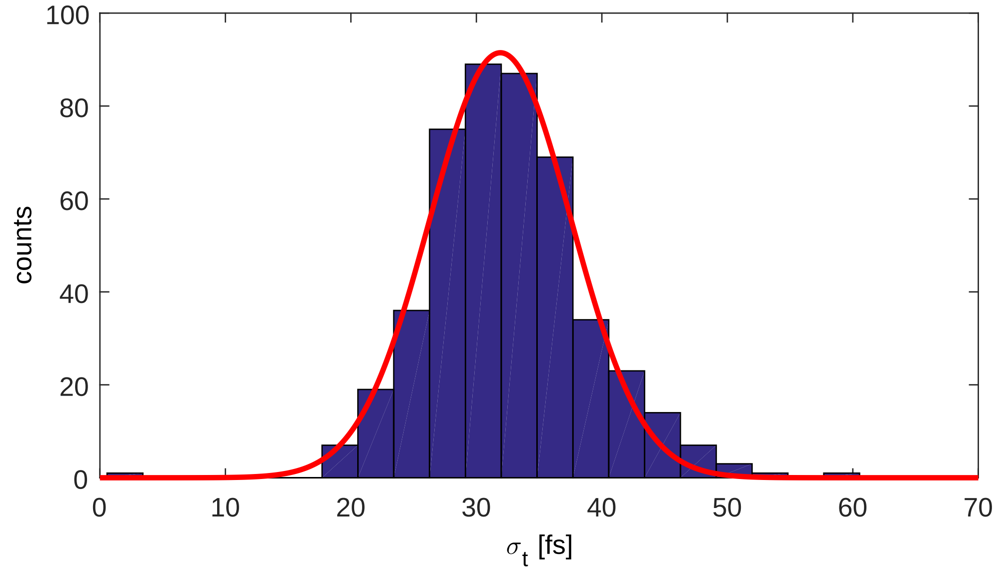

Figure 5.11.: Histogram of FEL pulse durations extracted from 1300 consecutive shots. The red line shows a Gaussian fit to the histogram.

of the seed laser pulse length extracted from the evaluation of 590 consecutive shots. The mean of a Gaussian fit provides an estimation of the laser pulse duration, the rms width an estimation of the error:

$$\sigma_{\mathrm{t,l}} = (82.6 \pm 6.0)\,\mathrm{fs}. \tag{5.8}$$

The pulse duration of the FEL pulse can be extracted from the power profile reconstruction described in Chapter 4. Figure 5.11 shows the corresponding histogram for 1300 consecutive FEL shots taken at optimum performance with maximum seed laser intensity. The mean of the Gaussian fit provides estimation of the pulse duration, the rms width an estimation of the error:

$$\sigma_{\mathrm{t}} = (33.0 \pm 3.9)\,\mathrm{fs}. \tag{5.9}$$

This is approximately what can be expected by the rule of thumb that relates the length of an HGHG generated photon pulse to the seed laser pulse length [80, 81]:

$$\sigma_{\mathrm{t}} \approx \frac{\sigma_{\mathrm{t,l}}}{\sqrt[3]{n}}, \tag{5.10}$$

where n is the harmonic number. In case on the presented experimental data $n = 7$ and the FEL pulse length should be $\sigma_{\mathrm{t}} \approx 43\,\mathrm{fs}$. The derivation of this rule of thumb, however, assumes the dispersive strength optimized for maximum bunching. In the experiment presented, the dispersive strength was not tuned to this maximum, but had a lower value, leading to a shorter longitudinal region that was significantly bunched to radiate. As we will see, Eq. (5.10) no longer holds for smaller laser amplitudes, where the $R_{56} = -50\,\mu\mathrm{m}$ is away from optimum bunching.

5.5. GENESIS 1.3 Simulation of Working Point

With the extraction of the slice emittance and the fit of the modulation amplitude, all the necessary information is known to conduct a full numerical simulation of the FEL process. The simulation is conducted with GENESIS 1.3 v2 [82] in two separate simulation runs, one for the modulation and a second one for the radiation process. This section describes the results of a working point simulation that corresponds to a laser-electron timing for the high-performance region of the time scan described in section 4.6 at about -50 fs.

The slice parameters used for this simulations can be found from the measurements in Chapter 4 and are $I = 570\,\mathrm{A}$, $\sigma_{\mathrm{W},0} = 62\,\mathrm{keV}$ and $\epsilon_{\mathrm{n}} = 1.015\,\mathrm{mm\,mrad}$. The beam generated with GENESIS 1.3 has constant energy spread and emittance along the bunch. The current profile is a Gaussian with the peak current mentioned before. These simplifications can be applied since within the resulting FEL pulse duration of about 34 fs the variation of these parameters is small (e.g. the variation of the current is below 5%).

The transverse profile of the seed laser has been modeled according to the measurements given at the beginning of this chapter. Using Eq. (3.2), the peak power of 100 MW has been chosen to generate the modulation amplitude as predicted in chapter 4. Its longitudinal power profile is a Gaussian with an rms duration of $\sigma_{\mathrm{t,l}} = 70\,\mathrm{fs}$. This duration has been chosen to correspond not only to the peak power observed in the experiment, but also to the generated energy and FEL pulse length. It is well in line with the pulse duration extracted from the modulation amplitude measurements in Section 5.4.

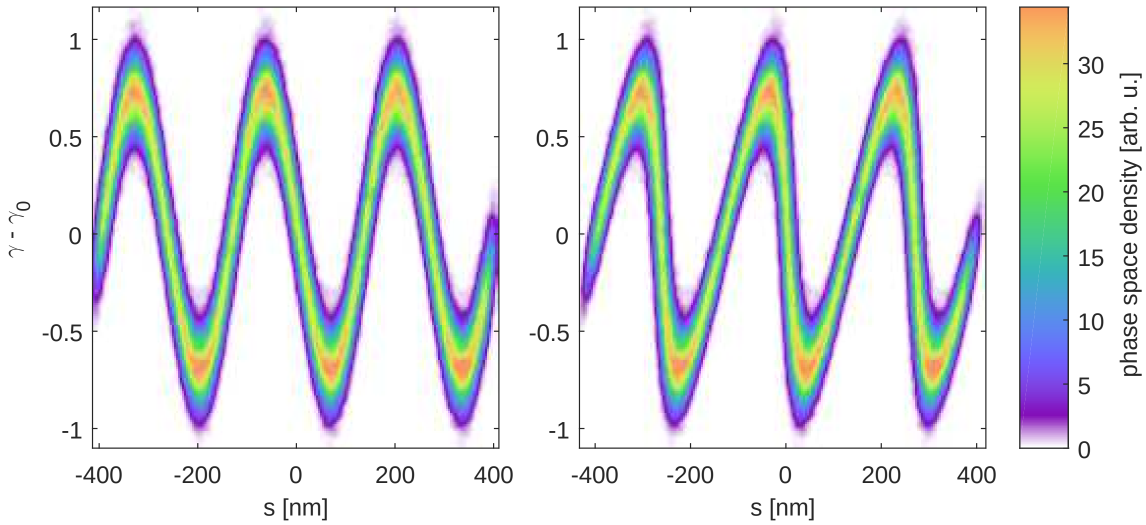

Figure 5.12.: Three-period-part of the longtitudinal phase space distribution of the central part of electron bunch. The left panel shows the energy modulated electron bunch, the right panel shows the electron bunch after traversing the chicane with a dispersive strength of $R_{56} = 50\,\mu\text{m}$. As can be seen, the electrons experienced a longitudinal displacement as a function of their energy and the sinusoidal energy modulation was converted to a sawtooth distribution.

Figure 5.12 shows a small section of the longitudinal phase distribution for the experimental settings. Using Eq. (3.3) the induced modulation amplitude within the core region is $\Delta\gamma = 0.79$. The induced bunching with a longitudinal dispersion of $R_{56} = -50\,\mu\text{m}$ at the start of the undulator is 3.1%. The chicane is treated by the transfer matrix formalism GENESIS 1.3 offers and thus does not include any collective effects. Table 5.4 summarizes the most important input parameters for the numerical simulation.

The radiators of the second stage are all tuned to the resonance of the 7th harmonic of the 266 nm seed laser. It should be noted that this is a difference to the setup of the experiment where the undulators are tuned for maximum energy output. If the FEL runs into saturation this could make a difference, since the last undulator could then be tapered to gain more output power. However, since the last undulator only contributes half a gain length and the process does not run into saturation, this effect is not significant.

Figure 5.13 shows the gain curve generated by the numerical simulations. The position at which the photon pulse ceases to gain energy for the 100 MW case is at $z_\text{p} = 8.56\,\text{m}$ in this figure, since GENESIS 1.3 also simulates drift spaces between undulator modules. This corresponds to the $z_\text{p} = 6.4\,\text{m}$ of total undulator length mentioned before, without drift spaces. In the region in the fourth undulator module ($z > 7.8\,\text{m}$) both models agree quite well, though the Ming-Xie formalism predicts a smaller gain length, while the numerical simulations start the lasing from the initial bunching more efficiently. A significant difference between both models appears in saturation. The Ming-Xie model predicts a saturation power almost 40% higher than the numerical simulations. Both differences can be attributed to the special optics used in seeded operation, where the

Modulator	
number of undulator modules	1
undulator period λ_u	20 cm
undulator parameter K	2.75
undulator model length L_u	1 m
number of periods per module N_u	5
Laser Pulse	
wavelength λ_seed	266 nm
peak power P_L	100 MW
rms duration $\sigma_\mathrm{t,l}$	70 fs
energy E_L	16.5 µJ
Rayleigh length z_R	3.25 m
M^2	1
Radiator	
number of undulator modules	3+1
undulator period λ_u	31.4 mm
undulator parameter K	2.588
undulator model length L_u	10 m
number of periods per module N_u	60 (120)
length of drift space between modules L_drift	0.72 m
Electron Bunch	
peak current I_peak	570 A
bunch duration $\sigma_\mathrm{t,e}$	200 fs
electron energy W_0	685 MeV
energy spread $\sigma_\mathrm{W,0}$	62 keV
normalized emittance ϵ_n	1.01 mm mrad

Table 5.4.: Input parameters for GENESIS 1.3 simulations. The slice parameters have been taken for the region of maximum performance as evaluated in chapter 4 at -50 fs with respect to the charge center-of-mass as indicated in Fig. 4.2 (p. 41).

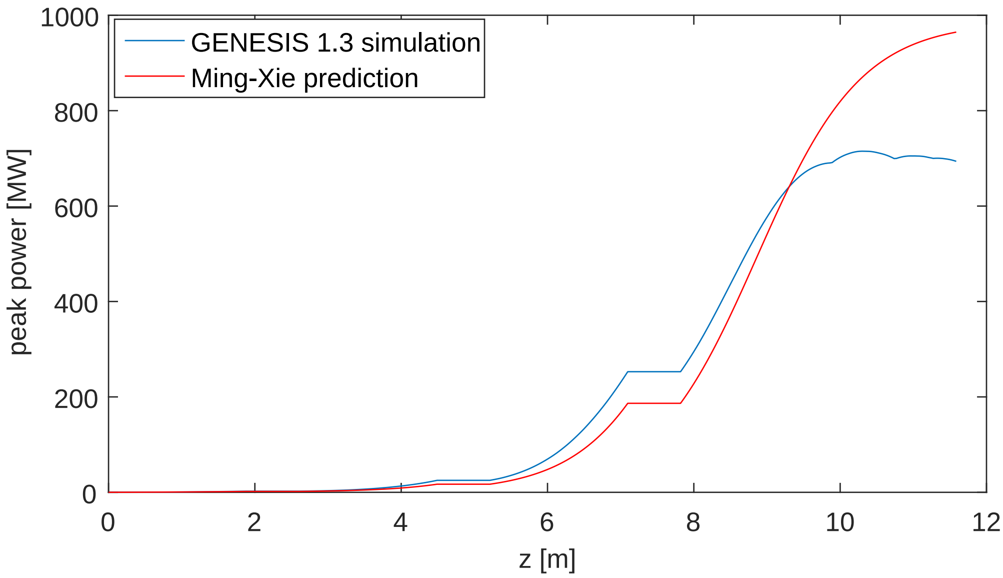

Figure 5.13.: Gain Curve generated by GENESIS 1.3 simulations. For comparison the gain curve of the Ming-Xie predicitons from chapter 4 has been added.

quadrupoles within the radiator are deactivated. While GENESIS 1.3 can account for this effect and can simulate a small beamsize in the first radiator modules (efficient start) and a large beamsize in the last radiator module (no gain at $z > 9\,\mathrm{m}$) where the electron phase space density is just too small to generate further gain, the Ming-Xie model does not account for this effect, but uses an average gain length over the whole radiating section.

The numerical simulations have the advantage over analytical calculations that they can predict the longitudinal power profile of the FEL photon pulse. Figure 5.14 shows the FEL power profiles for all three seed laser power settings at z_p. From the rf deflector measurement the pulse durations for the two higher laser power settings can be extracted. The FEL peak power from the measurements with 64.5 MW seed laser power is below 100 MW and is thus disregarded in the evaluations. The measured FEL pulse duration during gain curve measurements for 100 MW seed laser power is $\sigma_\mathrm{t} = (35.0 \pm 2.1)\,\mathrm{fs}$ and for 81.5 MW seed laser power $\sigma_\mathrm{t} = (27.5 \pm 4.3)\,\mathrm{fs}$. While the seed laser duration in the simulations was chosen to fit the high power case, also the lower power FEL pulse duration agrees with the numerical simulations within its errors.

Figure 5.15 shows the spectra at z_p for the three different seed laser pulse energies. The relative width of the spectra is about the same in all three cases and is below the spectral resolution of the installed spectrometer. The resolving power of the spectrometer has to be $\frac{\lambda}{\Delta\lambda} > 1350$ to resolve the expected spectral width.

5.6. Analysis of FEL Power Fluctuations

The analysis presented up to this point concerns mean values only. As can be seen from measurements of photon pulse energies or peak powers, the variation of these quantities are quite extensive. Relative 1σ fluctuations amount to over 30%. Since the slice parameters

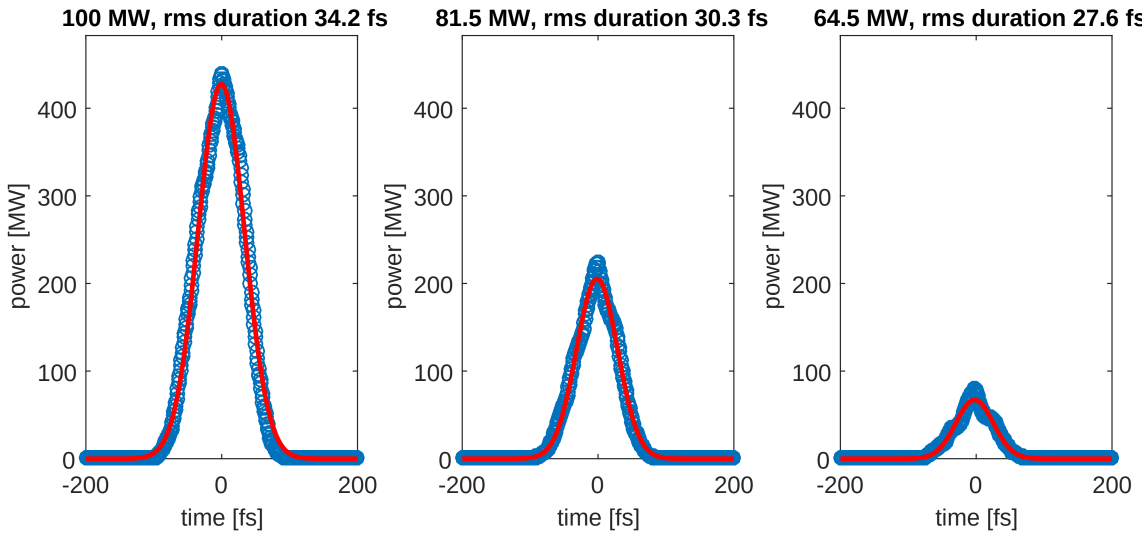

Figure 5.14.: Numerically simulated FEL power profiles (blue lines) at z_p with a Gaussien fit (red lines). The rms pulse durations from the fit are given in the title of each figure.

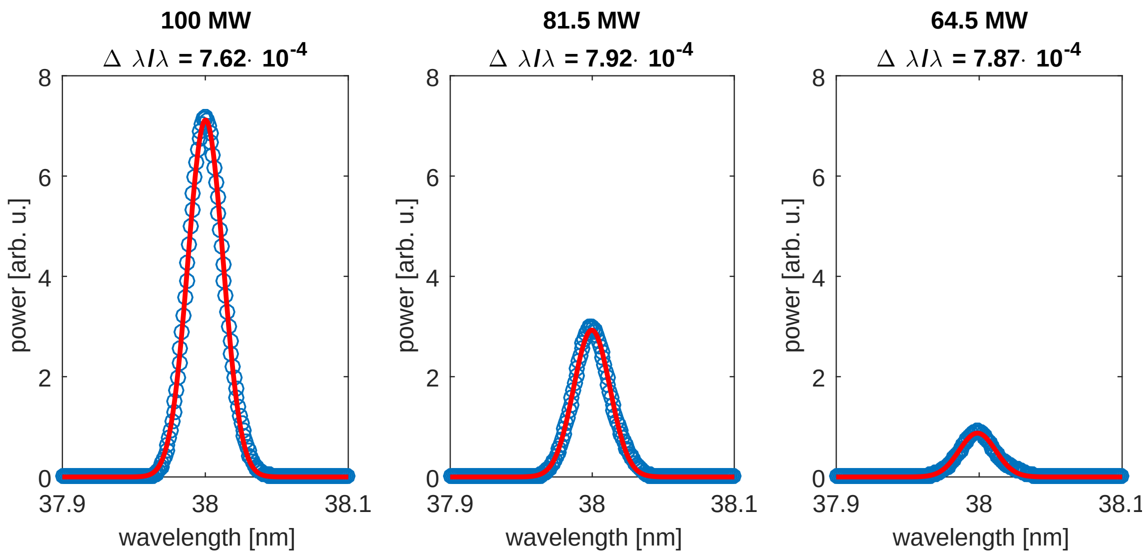

Figure 5.15.: Numerically simulated FEL power spectra (blue circles) at z_p with a Gaussien fit (red lines). The relative fwhm widths are given in the title of each figure.

do not fluctuate significantly from shot to shot (e.g. the current only fluctuates 2% in rf deflector measurements), the reason for the observed fluctuations is found in seed laser pulse variations. There are two main properties of the seed laser that are important for the seeding process and that experience strong fluctuations:

- **Laser-electron timing variations** can induce changes of output power of the seeded FEL. When the position of the modulation within the electron bunch differs from shot to shot, the slice energy spread and slice emittance of the seeded portion of the electron bunch might change. While the slice energy spread determines the induced bunching, the power gain of the FEL process is determined by both slice energy spread and slice emittance.
- **Laser intensity variations** cause the modulation amplitude and thus the bunching to be different from shot to shot. While this certainly influences the final power of the FEL, the induced energy spread from the seed laser will also determine the final energy spread of the electron bunch, again influencing the power gain of the process. There are two contributions to the effective laser intensity variations:
  - The laser intensity fluctuates on a magnitude of several tens of percent. While the laser energy in the infra-red oscillator pulse only fluctuates maximum by 2 % (rms), the UV energy variations are expected to be higher due to the non-linear conversion process.
  - A second source for laser intensity variations is a changing position of the laser profile at the point of interaction with the electrons. Since the transverse laser profile is a Gaussian with a width of several hundred micrometer, the local intensity within the electron bunch will change when the position of the beam fluctuates.

In the following we will try to estimate the variations of the longitudinal timing δ_{t}, of the laser intensity δ_{I}, and of the transverse beam position $\delta_{\mathrm{x}}/\delta_{\mathrm{y}}$. Using the Ming Xie formalism the effect on the resulting peak power will be studied in more detail.

5.6.1. Laser-Electron Timing Fluctuations

The effect of the longitudinal fluctuations of the laser-electron-timing depends on the compression scheme used, since this determines the longitudinal profile of slice energy spread, slice emittance, and current profile. The timing variations, however, can be identified independently of these slice properties by analyzing the laser timing scan shown in Sec. 4.6. As discussed above, the laser-electron timing has been changed in discrete steps during the measurements. While the TDS analysis allowed sorting the data by the longitudinal position of the extracted energy, we are now interested to extract the amount of the jitter of this position within one scan step. Thus in Fig. 5.16 we leave this data unsorted and show the standard deviation of the laser-electron timing fluctuations within each scan step of the laser-electron timing scan.

The fluctuations in the flanks of the distribution seems to be smaller than in the core region of the bunch. When comparing with the ability to lase derived in Sec. 4.6 it can be seen, that the regions of the bunch with small fluctuations are the ones that are closer

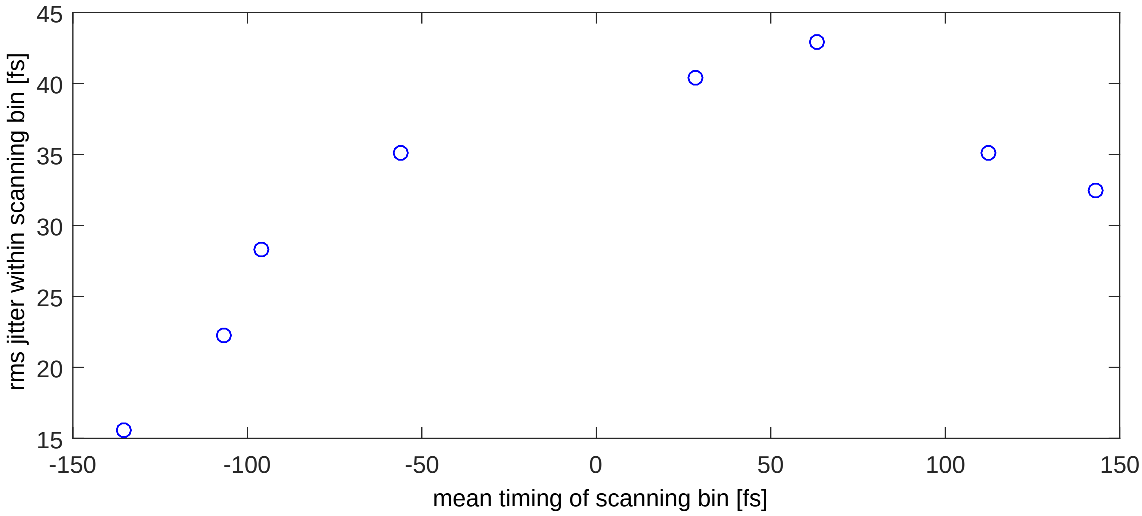

Figure 5.16.: Measured laser timing fluctuations within scan steps of the laser timing scan. The x-axis shows the mean of the laser position in each bin. Here, we refrained from giving uncertainties, since the data points will be analyzed in more detail and there is no additional benefit from error bars.

to the non-lasing flanks of the bunch. Though bunching is generated to start the FEL process in these regions, for many shots the gain is too small to generate a feature in the longitudinal phase-space distribution of the electron bunch measurable with the help of the rf deflector as described in Chapter 4. For the scan step at -135 fs this would mean that most shots with a more negative timing will preferentially be absent from the data series.

To illustrate this, Fig. 5.17 shows an example for an underlying laser-electron timing distribution for one timing step as a blue histogram. The red dashed line shows an approximation of the outer left wing of the mean power curve shown in Fig. 4.7. It thus represents the ability of certain regions of the electron bunch to show FEL gain when hit by the seed laser. The red histogram is the product of the underlying laser-electron timing distribution and the red power gain profile and represents the measurement of the rf deflector. On the leftmost bin of the blue histogram no shot can be amplified to powers that can be detected by the rf deflector, thus the red histogram shows no counts here. On the rightmost bin, the every shot shows enough gain and the counts remain the same as in the underlying laser-electron timing distribution. In essence, the resulting red histogram and the underlying blue distribution show a different mean and variance. In the example shown here, this decreases the jitter of the measured red distribution when compared to the real fluctuations of the underlying distribution. In a real data set, the jitter of the initial seed laser power further impedes the extraction of the real laser-electron timing fluctuations from the data.

In order to further analyze the problem, Fig. 5.18 shows histograms of the measured data sets leading to the data points in Fig. 5.16. To identify the real laser fluctuations we want to find the histogram that is not influenced by the filter function, and thus the one closest to a normal distribution. To do this, each histogram has been analyzed with the

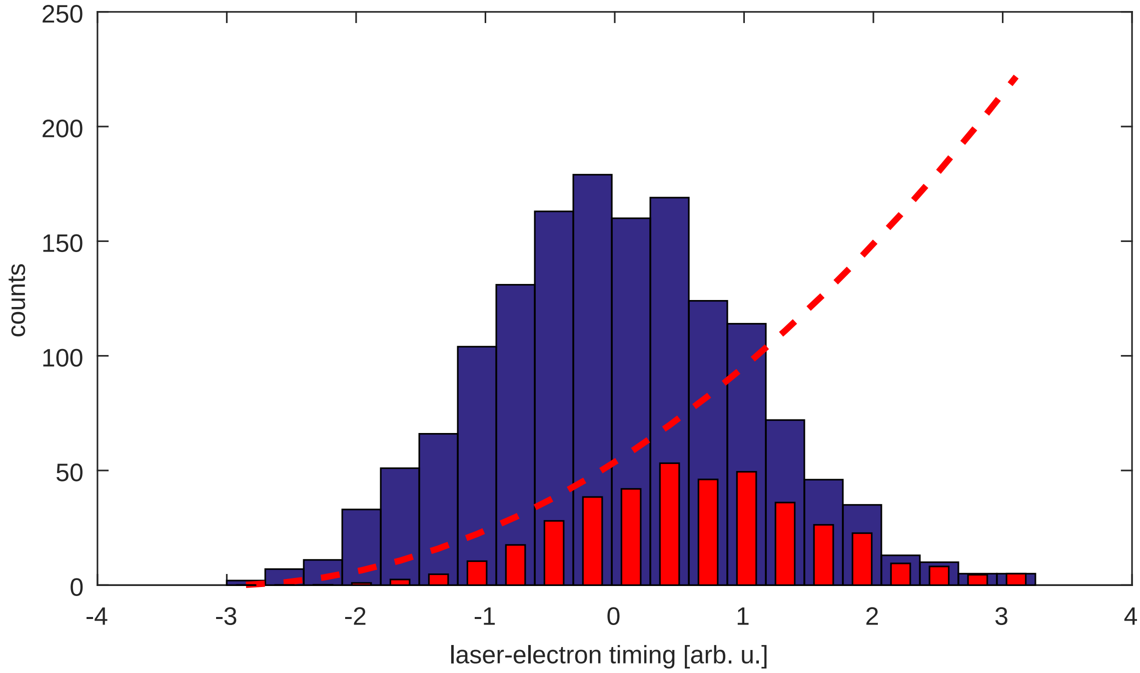

Figure 5.17.: Sketch of a laser-electron timing jitter histogram (blue bars) that is influenced by a filter function (red dashed line). The red bars show the resulting distribution with a different μ and σ.

Lilliefors test [83] that tests if a distribution comes from a normal probability function. A brief description of the test has been given in the Appendix A. The result of this test is a p-value for every histogram. If this value is smaller than a significance α, the test rejects the null hypothesis and the distribution does not originate from a normal distribution. Thus, the higher the p-value the higher is the mathematical similarity to a normal distribution. For the test we chose $\alpha = 5\%$.

The gray colored histograms in Fig. 5.18 have failed the test; the first and the last histogram have a sample size that is too small to reject the hypothesis. The remaining samples ($\mu = 25\,\mathrm{fs}$, $\mu = 63\,\mathrm{fs}$ and $\mu = 112\,\mathrm{fs}$) pass this test. However, the distribution that has the highest probability to originate from the normal distribution is the one with $\mu = 25\,\mathrm{fs}$. A Gaussian fit to the data gives the rms timing fluctuations of the laser-electron overlap:

$$\delta_{\mathrm{t}} = (39.7 \pm 1.7)\,\mathrm{fs} \tag{5.11}$$

An additional feature can be observed for the distributions with $N > 50$: Distributions that are at the front of the bunch ($\mu \gtrsim 50\,\mathrm{fs}$) look like normal distributions that are cut on the right by the filter described above. The same is given for the distributions in the tail ($\mu \lesssim -50\,\mathrm{fs}$) that are cut on the left.

5.6.2. Laser Intensity Variations

The intensity fluctuations of the seed laser at the point of interaction cannot be measured directly. The only accessible data can be taken by the two YAG screens *6ORS* and *10ORS*

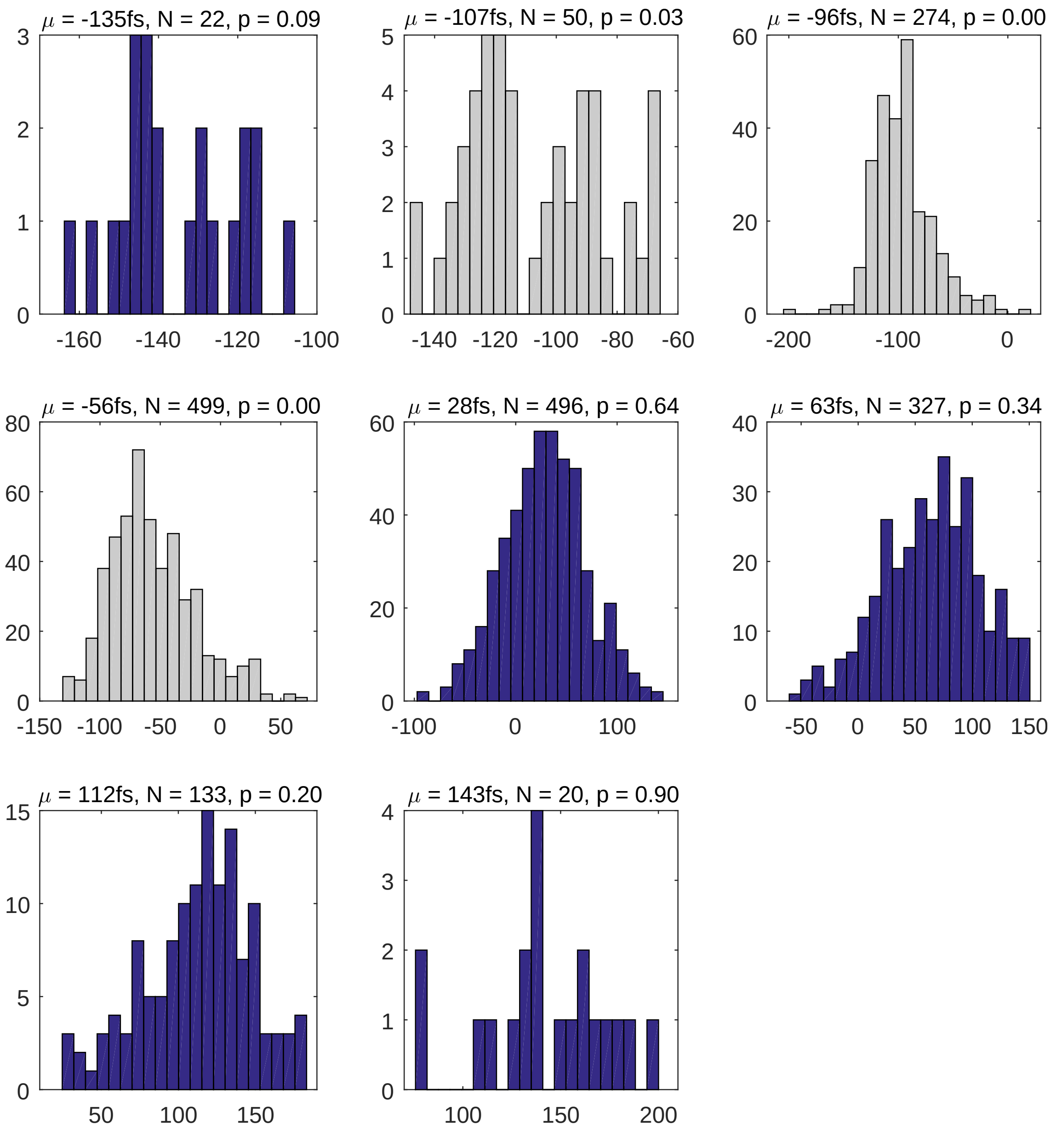

Figure 5.18.: Histograms of data points from Fig. 5.16. Each histogram is titled with the corresponding mean μ showing where the point can be found in Fig. 5.16 and the total number of data points within the series. The Lilliefors tests on the histograms with gray face color rejected the null hypothesis to originate from normal distributions.

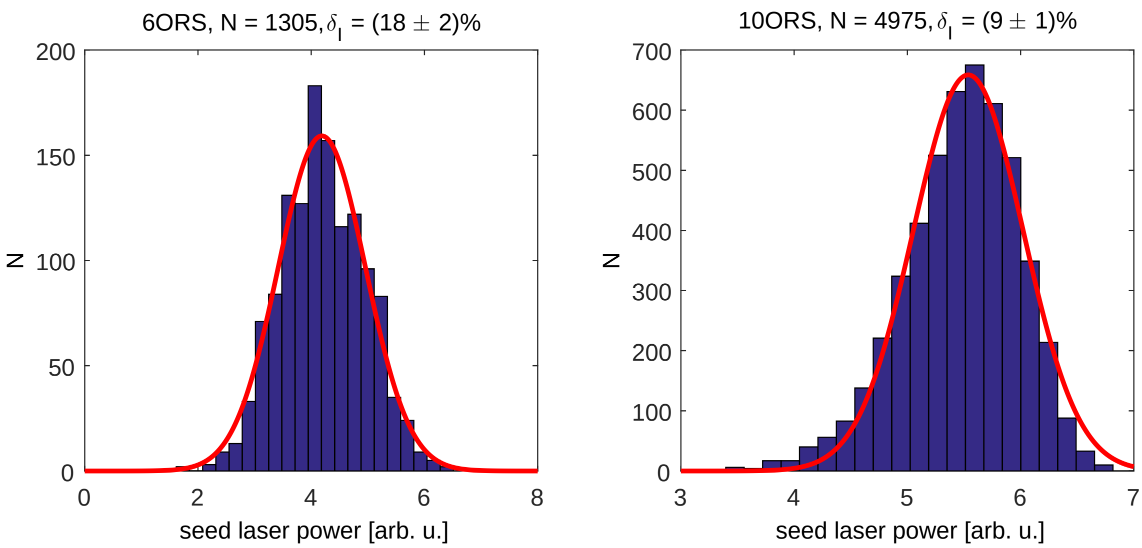

(a) Energy of the full laser beam.

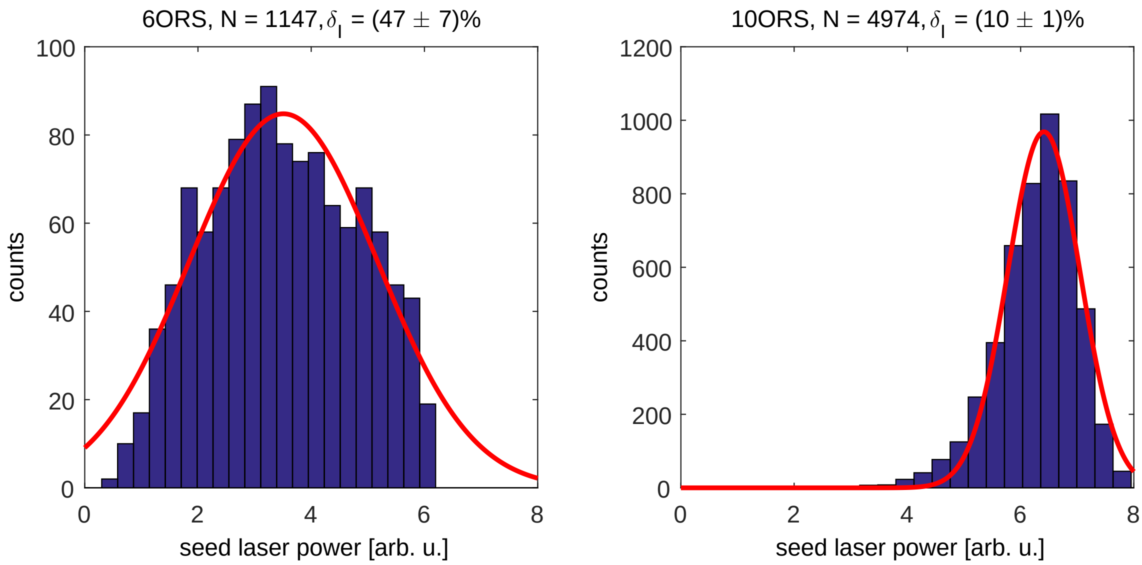

(b) Energy of fraction of the laser beam in overlap with the electron beam.

Figure 5.19.: Laser energy histograms on YAG screen *6ORS* and *10ORS*. The upper panel *(a)* shows the energy histograms for the full laser beam. The lower panel *(b)* shows energy histograms of fraction of the laser beam in overlap with the electron beam.

	Measurement	Simulation
laser-electron timing δ_t	40.2 fs	39.7 fs
laser power δ_I	11.0%	11.0%
modulation amplitude	none	5.5%
bunching factor	none	29.8%
FEL peak power	33%	34.7%

Table 5.5.: Comparison of measured and calculated fluctuations. The measured fluctuations of δ_t and δ_I serve as input parameters for the normal distributions of the Monte-Carlo studies. The resulting FEL peak power jitter is well in line with its measurement.

that are located in front and behind the modulating undulator. The corresponding energy fluctuations of the laser can be found in Fig. 5.19a. As described earlier, the laser intensity variations at the point of interaction is composed of laser position variations and intrinsic laser intensity fluctuations. The important quantity for the modulation process, however, is the laser power within the area occupied by the electron bunch. Figure 5.19b shows histograms of the laser energy within the 1σ beamsize area of the electron beam for both YAG screens.

As can be seen from the histograms, the energy fluctuations strongly differ from screen to screen. Other detectors like a CCD chip that detectors the leakage of one of the injection mirrors measure about 10% total energy fluctuations which is more in line with the variations seen on the *10ORS* screen. Thus the subsequent analysis will use the values measured with *10ORS*.

5.6.3. Monte-Carlo Simulation of FEL Power Fluctuations

Once the fluctuation sources have been identified, the impact of these sources on the final FEL performance can be studied. The input parameters that are subject to variations are the laser energy (and thus modulation amplitude) and the laser-electron-timing (and thus slice parameters). A set of 10000 pairs of laser energies and laser-electron is generated from normal probability distributions that have the parameters derived in the last two subsections. For each pair, the FEL performance is then estimated using the Ming-Xie-model. The resulting gain curves are calculated with the equation for FEL power evolution when started from an initial density modulation as given in Eq. (3.9) (p. 23).

Figure 5.20 shows an overview of the simulations. The input parameters for the longitudinal laser position and the laser power fluctuations have been chosen according to the previous two subsections. Table 5.5 summarizes the standard deviations of the Gaussian fits in Fig. 5.20 and thus the variations on several parameters. The predicted fluctuations of the FEL peak power is thus about 35%, well in line with the measured fluctuations of 33%.

The analysis presented here has been conducted with a mean laser-electron timing of -50 fs. The longitudinal position variations will only slightly change the slice parameters (as shown in Fig. 4.6 on p. 50) at this position and thus the gain length of the FEL process.

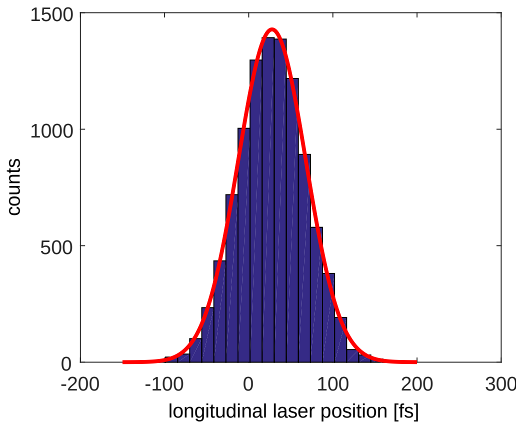

(a) longitudinal laser position fluctuations, $\sigma = 40.2\,\mathrm{fs}$

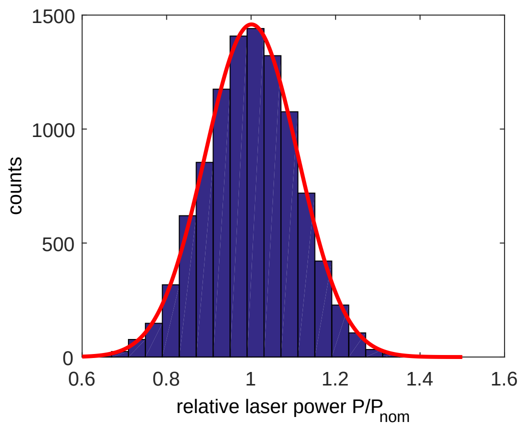

(b) laser power fluctuations, $\sigma = 11.0\%$

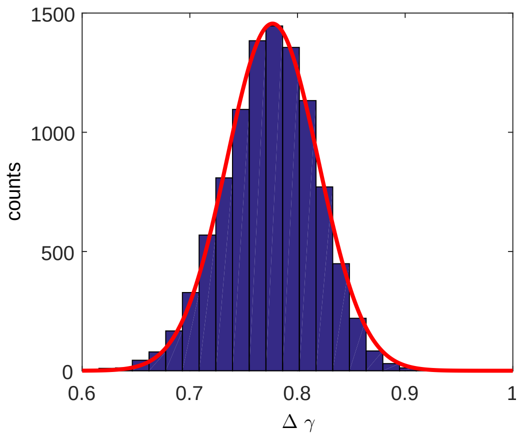

(c) modulation amplitude fluctuations, $\sigma = 5.5\%$

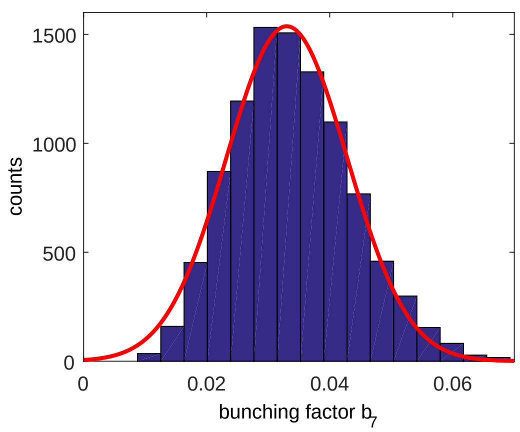

(d) bunching factor fluctuations on 7th harmonic, $\sigma = 29.8\%$

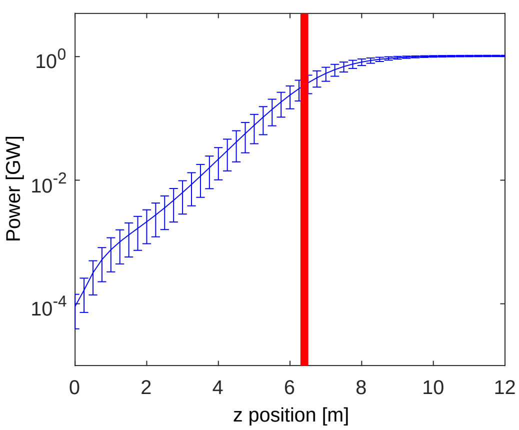

(e) mean and standard deviation of calculated gain curves, the red line is drawn at $z_\mathrm{p} = 6.4\,\mathrm{m}$

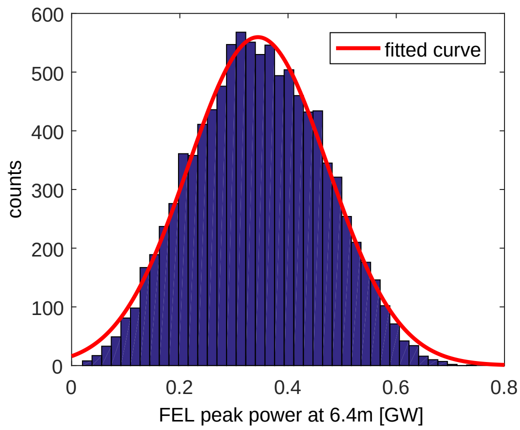

(f) FEL power fluctuations at $z_\mathrm{p} = 6.4\,\mathrm{m}$, $\sigma = 34.7\%$

Figure 5.20.: Monte-Carlo fluctuations analysis using the Ming-Xie model. The parameter σ given in the figure captions denotes the rms width of the Gaussian fit. Panels *(a)* and *(b)* show the distribution of the input parameters, panels *(c)* and *(d)* give calculated fluctuations on modulation amplitude and bunching factor, and panels *(e)* and *(f)* give the results obtained from the Ming-Xie model.

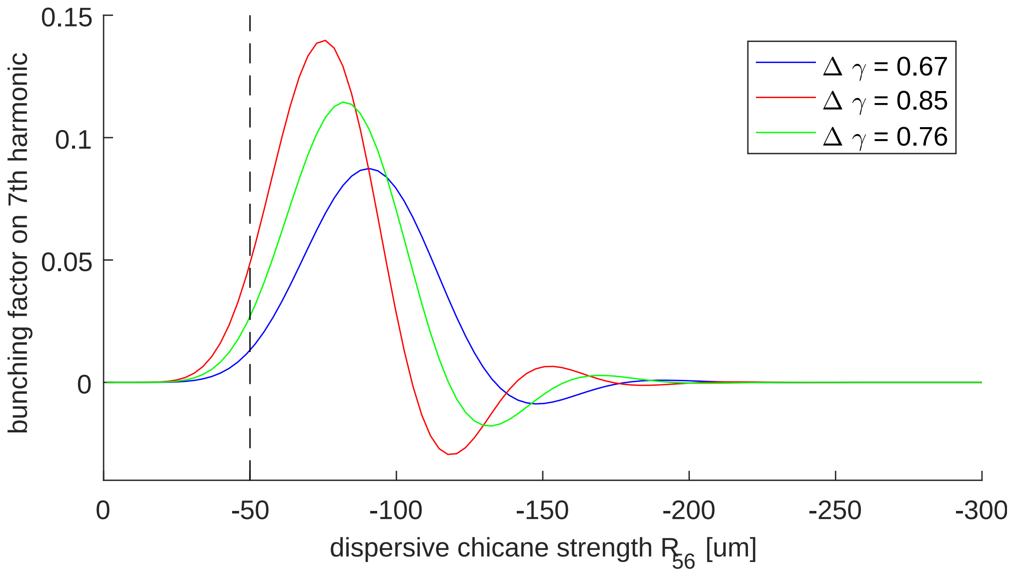

Figure 5.21.: Bunching factor on 7th harmonic as a function of dispersive strength R_{56}. The colored curves show the bunching for different modulation amplitudes $\Delta\gamma$. The dispersive strength during the experiment has been tuned to $R_{56} = -50\,\mu\text{m}$ shown as a vertical black dashed line in the plot.

The FEL power variations caused by these fluctuations only account for about 3%, the remaining 30% result from the laser power variations.

5.6.4. Discussion on HGHG Performance Stability

As discussed above the main reason for the FEL power variations is the fluctuation of the seed laser energy. Thus, the stability of the FEL power can be optimized by either decreasing the laser energy jitter or finding a more stable point of operation for the accelerator. While an optimization of the laser energy stability is the favorable solution, residual fluctuation will always remain, since they are intrinsic to the laser system. This section will focus on the issue of what can be done on the accelerator side to enhance the FEL power stability.

The relation between seed laser power and FEL power variations is a function of the longitudinal dispersion R_{56}. During the data series presented here, the chosen $R_{56} = -50\,\mu\text{m}$ was not in favor of good FEL power output stability. Figure 5.21 shows the bunching factor on the 7th harmonic as a function of dispersive strength for different modulation amplitudes. The variation of the bunching for a given change in $\Delta\gamma$ is higher at $R_{56} = -50\,\mu\text{m}$ than at an R_{56}^{opt} for optimum bunching. The most stable R_{56}^{stable} setting, however, is slightly higher than the optimum R_{56}.

To find R_{56}^{stable} we want to find the R_{56} for which the variation for the bunching for different $\Delta\gamma$ is small or even zero. Thus we derive Eq. (3.7) with respect to $\Delta\gamma$ and find the R_{56} for which the derivative vanishes:

$$\frac{\mathrm{d}b_\mathrm{n}}{\mathrm{d}\Delta\gamma}(R_{56}, \Delta\gamma) = 0\,\Big|_{\mathrm{R}_{56}^{\mathrm{stable}}}\,. \tag{5.12}$$

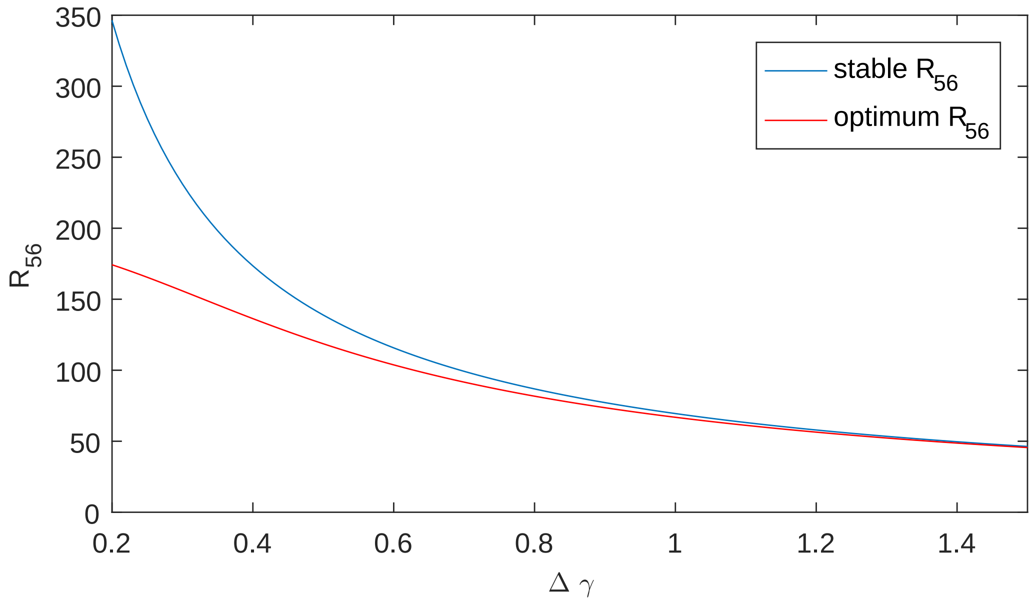

(a) Optimum and stable R_{56} value for different modulation amplitudes. For higher modulation amplitudes the difference between both gets smaller.

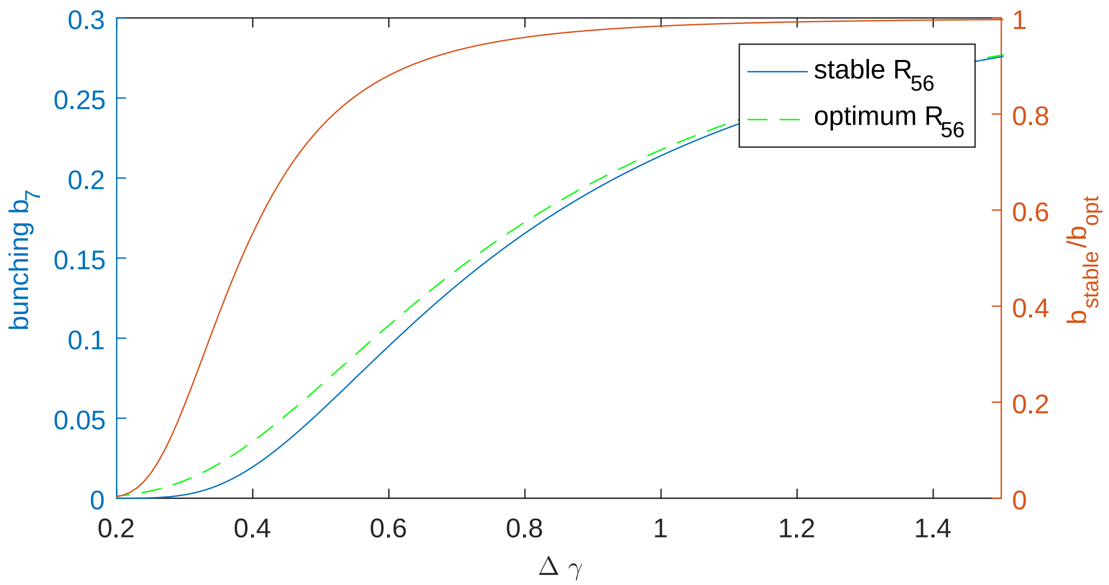

(b) Bunching factor on 7th harmonic for optimum and stable R_{56} values. The *orange* line shows the ratio between the bunching factors with stable and optimum R_{56}.

Figure 5.22.: Optimum and Stable R_{56}

The derivative takes the form

$$\frac{\mathrm{d}b_{\mathrm{n}}}{\mathrm{d}\Delta\gamma}(R_{56},\Delta\gamma) = \kappa(R_{56}) \cdot \exp^{-\nu(R_{56})} \cdot (J_{\mathrm{n}-1}(\xi(R_{56}\cdot\Delta\gamma)) - J_{\mathrm{n}+1}(\xi(R_{56}\cdot\Delta\gamma))), \quad (5.13)$$

where

$$\begin{aligned}
\kappa(R_{56}) &= n\pi R_{56} m_{\mathrm{e}} c^2/(W_0\lambda_{\mathrm{seed}}), \\
\nu(R_{56}) &= 2n^2\pi^2 R_{56}^2 \sigma_W/(W_0^2\lambda_{\mathrm{seed}}^2), \text{ and} \\
\xi(R_{56}\cdot\Delta\gamma) &= 2n\pi\Delta\gamma R_{56} m_{\mathrm{e}} c^2/(W_0\lambda_{\mathrm{seed}}).
\end{aligned}$$

The product of the three factors in Eq. (5.13) is 0, if one of them is 0 and thus the three terms can be treated separately. $\kappa(R_{56})$ only vanishes for the trivial solution $R_{56} = 0$, and the value of the exponential factor never reaches 0. The interesting factor is the one comprised of the Bessel functions. The two parameters $\Delta\gamma$ and R_{56} only appear as a product. Therefore, R_{56}^{stable} will be a hyperbolical function of $\Delta\gamma$:

$$R_{56}^{\mathrm{stable}} = \mathrm{const}/\Delta\gamma, \quad (5.14)$$

where the constant can be found via numerical solution of Eq. (5.12). For the data series presented here the dispersive strength for stable FEL operation is

$$R_{56}^{\mathrm{stable}} = 69.55\,\mu\mathrm{m}/\Delta\gamma, \quad (5.15)$$

It is seen that R_{56}^{stable} only solves the condition in Eq. (5.12) locally for $\Delta\gamma$. Thus the three curves in Fig. 5.21 do not intersect in one point with a reasonable bunching and we cannot completely eliminate the bunching jitter caused by variations in the seed laser power.

To compare with the Monte-Carlo simulations shown before, a set of $\Delta\gamma = 0.44$ and $R_{56}^{\mathrm{stable}} = -158\,\mu\mathrm{m}$ has been used that results in the same bunching as in the simulation shown in Fig. 5.20. While the influence of the longitudinal laser position jitter stays the same, the relative FEL power jitter can be reduced to 8.5%.

Figure 5.22a shows the optimum and stable R_{56} for different modulation amplitudes. Both, the absolute and relative difference between both decrease with higher modulation amplitude $\Delta\gamma$. Figure 5.22b gives an idea of the amount of bunching sacrificed, when choosing R_{56}^{stable} as an operation point. If a modulation amplitude of $\Delta\gamma \geq 0.5$ is achieved the bunching generated with the stable longitudinal dispersion is more than 80% of the optimum bunching and choosing this R_{56} might be a good option to stabilize the energy output. If the modulation amplitude can be increased to $\Delta\gamma \geq 1.0$, the difference between stable and optimum R_{56} becomes very small, the two operation points basically become the same and there is no trade-off between stability and bunching anymore. Thus, whenever possible, the laser power should be chosen to generate a modulation amplitude $\Delta\gamma \geq 1.0$.

From Fig. 5.22a it can also be seen, that $R_{56}^{\mathrm{stable}} \geq R_{56}^{\mathrm{opt}}$. This means that the stable operation point slightly overcompresses the modulated part of the bunch with the highest modulation amplitude. For a seed laser beam with a Gaussian longitudinal profile this means that a longer part of the bunch gets higher bunching and the photon pulses will get longer. A GENESIS 1.3 simulation has shown that, for the same initial parameters, the photon pulse duration is increased from 35 fs to 45 fs rms. The shape of the longitudinal power profile of the FEL pulse will also strongly deviate from a Gaussian with a plateau at its maximum. These imperfections also get smaller for higher modulation amplitudes.

Thus, if the modulation amplitude is smaller than 1, the choice of the longitudinal dispersion generated in the chicane is a trade-off between short Gaussian FEL pulses and a more stable operation in terms of output energy.

5.7. Summary

The sFLASH experiment has successfully demonstrated HGHG seeded FEL operation close to saturation at 38 nm, the 7th harmonic of the seed laser wavelength. After the six-dimensional overlap between electron and seed laser has been established, an rf deflector measurement on the uncompressed electron bunch enables estimations for the induced modulation amplitude and seed laser pulse duration.

As a next step, the electron bunches have been compressed to peak currents of 620 A to start the FEL process in the radiator. The gain curves for different seed laser energies were measured and are well in line with numerical simulations conducted with GENESIS 1.3. The electron bunch characteristics used during these simulations have been derived from rf deflector measurements. The laser properties have been derived by the fitting method shown in chapter 4. Electron optics have been modeled according to the optics measurement during the experimental setup.

The gain curve measurements show less gain than expected in the last undulator segment. The amount of gain depends on the initial modulation amplitude. A likely explanation is the evolution of the energy spread due to longitudinal space charge forces action on the coherent structures imprinted on the electron beam by the HGHG process. In this thesis only a qualitative explanation of the process has been given. Further analysis has to be conducted in order to predict the evolution of the energy spread when traversing an undulator. Once this is achieved, the data set can be evaluated again by analyzing the energy spread measured with the rf deflector. In the future a dedicated experiment can be prepared to study these effects, where not only different modulation amplitudes, but also a set of dispersive strengths can be studied in order to study the impact of these LSC forces on the FEL gain.

Though the FEL pulse power observed was on the order of 400 MW, the signal is subject to strong jitter of over 30%. An Analysis of the jitter sources showed that the seed laser intensity fluctations at the point of interaction with the electron beam is dominating the FEL pulse energy fluctuations. Though there have been improvements on the seed laser system, the variations of its energy cannot be eliminated completely. A condition on the longitudinal dipsersion has been derived that minimizes the impact of the laser jitter on the FEL pulse energy on the expense of longer photon pulses. A dedicated experiment to test this condition has not been done, yet, but should be one of the steps towards a seeded FLASH2 beamline for user experiments. The method presented on jitter analysis also enables the theoretical study of different compression schemes for the electron bunch and their sensitivity to laser-electron timing jitter.

After the successful demonstration of high-gain harmonic generation the focus of the sFLASH experiment can be shifted to controlling the characteristics of the photon pulse (e.g. the chirp) and preparing for more advanced seeding schemes such as echo-enabled harmonic generation.

6. Theoretical Considerations on FLASH2 Seeding

With the experimental experience and results obtained from the sFLASH experiment, this chapter focuses on numerical studies for the FLASH2 beamline. A full description of the current layout of the FLASH2 hardware has been given in Sec. 2.5.4. Since a possible seeding upgrade should maintain the capability of the beamline to lase in SASE mode, no undulator module can be removed. With the 12 undulator modules installed in 6 FODO cells, there are 4 FODO cells available for seeding hardware.

To decide on the best suited seeding scheme for the beamline, two options have been studied. The first part of this chapter focuses on the discussion of self-seeding, a scheme where the light of a first radiator stage traverses a monochromator and serves as direct seed for a second undulator beamline. The second part of the chapter addresses an HGHG scheme similar to the sFLASH experiment that should serve as a first step to make FLASH2 ready for more advanced phase-space manipulating seeding schemes like EEHG.

A cascaded HGHG setup for FLASH2 has been conceptually designed and proposed by A. Meseck [84]. Here, a first HGHG stage generates a light pulse that is used for the modulation process of a second HGHG stage [39]. This scheme, however, did not maintain the beamline's capability of generating radiation in SASE mode and thus a single-stage setup is proposed.

6.1. Self-Seeding at FLASH2

Self-seeding is a seeding scheme that does not require an external light source and thus offers some experimental advantages over the already described HGHG seeding that will be discussed below. Self-seeding was first proposed by Feldhaus et al. in 1997 [85] and experimentally shown at the Linac Coherent Light Source (LCLS) at Stanford Linear Accelerator Center (SLAC) in California, United States [47].

This chapter is dedicated to the question whether self-seeding is a viable upgrade option for FLASH2 seeding. Requirements the electron beam has to fulfill in order for the scheme to show a performance that significantly increases the characteristics of the final photon pulse will be discussed.

The tunability of the self-seeding scheme is quite limited, since the monochromator utilizes photon optics that diffract in an angle that is a function of the central wavelength of the photon pulse. This study focuses on a central wavelength of 5 nm. The range a final experiment can be tuned to might be about 1-2 nm without significant change of the optics in place.

6.1.1. Introduction to Self-Seeding

While external seeding schemes like HGHG use a laser source as a coherent seed for the FEL process, self-seeding, instead, uses the generated light of the FEL process itself. For this purpose, the undulator generating the light is divided into two stages by a monochromator that is used to cut out part of the spectrum of the first undulator stage to seed the second stage. Figure 6.1 shows a schematic view of such an experiment.

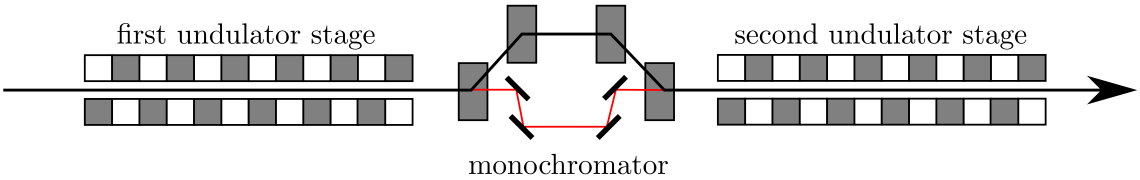

Figure 6.1.: Schematic overview of a self-seeded free-electron laser. The first undulator stage on the left generates a SASE spectrum that enters a monochromator (red line) and a fraction of the spectrum gets cut out. This part then seeds a second undulator stage. The electrons bypass the monochromator by a four dipole c-shaped chicane.

The light that seeds the second stage has to fulfill certain conditions in order to achieve best efficiency in the second stage. These conditions determine the requirements on the monochromator hardware and are necessary to derive before the monochromator design is discussed.

- The slit of the monochromator has to be reimaged to a certain point in the undulator. The position of this point as well as the image size are determined by the focussing properties of the monochromator optics. The conditions to be fulfilled for optimum coupling are discussed in section 6.1.2.
- For direct seeding of an FEL, the incoming seed has to be transversely coherent and its power has to significantly exceed the shot-noise power [85]. The coherence is intrinsically guaranteed by a high enough power-gain in the first undulator stage which is why the stage should be operated close to saturation. The power seeding the second undulator stage depends not only on the available FEL pulse power of the first stage (discussed in section 6.1.8), but also on the bandwidth of the monochromator (discussed in section 6.1.1.1).

While the light traverses the monochromator the electrons are deflected by a magnetic chicane in order to bypass the monochromato, and even more importantly, wash out any bunching that remains from the FEL process of the first undulator stage.

6.1.1.1. Monochromator Bandwidth

The available power in the second undulator stage of the experiment depends on the chosen monochromator bandwidth. We define the inverse bandwidth of the monochromator

$$R_{\mathrm{m}} = \left(\frac{\lambda}{\Delta\lambda}\right), \tag{6.1}$$

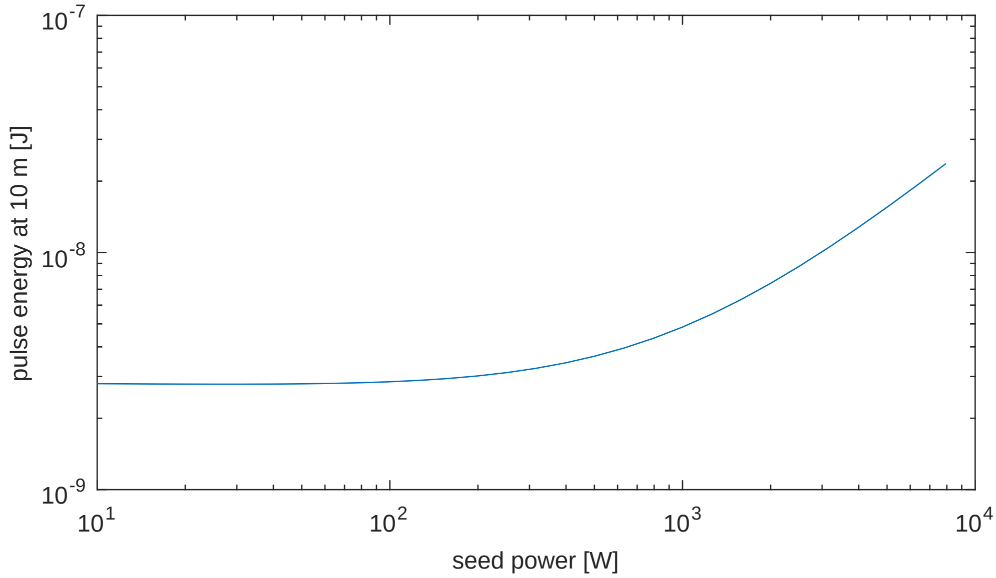

Figure 6.2.: Generated energy in the exponential gain regime after 10 m of undulator as a function of seed power.

where λ is the central wavelength of the incoming light and $\Delta\lambda$ is the full width at half maximum of the spectral part cut out by the monochromator. For the second undulator stage to be seeded the incoming power should significantly exceed the shot noise. Closely following [85], we can write this condition as

$$\frac{P_{\mathrm{in}}^{(2)}}{P_{\mathrm{shot}}} = G^{(1)} T_{\mathrm{m}} S_{\mathrm{m}} \gg 1, \tag{6.2}$$

where $P_{\mathrm{in}}^{(2)}$ is the photon pulse power going into the second undulator stage; P_{shot} denotes the relevant shot-noise equivalent power being about the same in both undulator stages. $G^{(1)}$ is the gain of the photon energy in the first undulator stage and thus is the power generated by this stage given by $P_{\mathrm{out}}^{(1)} = G^{(1)} P_{\mathrm{shot}}$. The coefficients T_{m} and S_{m} denote the loss of power due to losses on the reflective surfaces of the monochromator and losses at the exit slit, respectively. While T_{m} is a fraction that does not depend on the monochromator bandwidth, but only on λ and the properties of the optical elements, S_{m} depends on R_{m} and the bandwidth of the photon pulse of the first stage

$$S_{\mathrm{m}} = \frac{1}{R_{\mathrm{m}} (\Delta\lambda/\lambda)_{\mathrm{SASE}}} \leq 1. \tag{6.3}$$

Since there are a lot of analytical estimates for the shot-noise power that slightly deviate from each other, P_{shot} has been found by numerical simulations with GENESIS 1.3. Here a series of time-dependent simulations has been conducted and the input power of the seed laser has been varied. Figure 6.2 shows the FEL pulse energy generated by a directly seeded FEL process as a function of the power of the seed laser. The pulse power is evaluated at $z = 10\,\mathrm{m}$, where the FEL process already shows exponential power gain. The energy of the FEL pulse begins to increase, when the seed power reaches the shot noise equivalent power P_{shot}. This occurs at $P_{\mathrm{shot}} \approx 300\,\mathrm{W}$. The power of a seed for the second undulator stage has to exceed this power by a factor $10^2 - 10^3$ in order to dominate the power gain process. The monochromator setup, thus, has to be designed to provide at least $30\,\mathrm{kW}$ seed power.

By inserting Eq. (6.3) into Eq. (6.2), using the definition of $P_{\mathrm{out}}^{(1)}$ and integrating both sides of the equation over the photon pulse duration we get a similar equation for the energy, which will be used later to determine the seed energy and power available in the second stage:

$$\frac{E_{\mathrm{in}}^{(2)}}{E_{\mathrm{out}}^{(1)}} = \frac{T_{\mathrm{m}}}{R_{\mathrm{m}}(\Delta\lambda/\lambda)_{\mathrm{SASE}}}. \tag{6.4}$$

In addition to the condition in equation (6.2), the bandwidth of the monochromator must fulfill two further boundaries. First of all it obviously does not make any sense for the bandwidth to be any broader than the SASE bandwidth, which is already introduced by chosing $S_{\mathrm{m}} \leq 1$. Furthermore, we do not want to cut out less than one SASE spike, since the resulting pulse after the monochromator would get longer than the electron bunch itself and we would not only waste the energy we cut from this one mode, but also the energy in front and after the electron bunch.

Thus the boundaries on the bandwidth can be written as [17, 85]

$$\boxed{\frac{1}{(\Delta\lambda/\lambda)_{\mathrm{SASE}}} \ll R_{\mathrm{m}} \leq \sqrt{2}\pi\frac{\sigma_{\mathrm{z}}}{\lambda},} \tag{6.5}$$

or, in explicit numbers

$$450 \ll R_{\mathrm{m}} \leq 5000, \tag{6.6}$$

for an electron bunch duration of 20 fs. Note that a longer bunch duration would decrease the spectral width of one SASE mode and thus increase the upper limit of the resolving power. A higher resolving power will decrease, as will be shown later, the efficiency of the monochromator. Additionally, a longer electron bunch means more pulse energy that could damage the optical components upstream of the monochromator slit. Thus, for this case study an electron bunch duration of 20 fs will be used in order to decrease the probability to run into these restrictions. The monochromator will have a resolving power of $R_{\mathrm{m}} = 4500$ to cut out one SASE spike.

6.1.2. Optimum focussing

To design the optics of the monochromator, the optimum waist position and size for most efficient coupling in the second stage of the self-seeding setup have to be found. For this purpose a series of 319 time-independent GENESIS 1.3 simulations have been conducted. Time-independent simulations only track one slice through the undulator and assume periodicity. This means that no longitudinal information on the photon pulse can be deduced from these calculations.

Figure 6.3 shows the FEL peak power after 11 m of undulator, corresponding to about 4 gain lengths, where the seed already has coupled to the electron beam and the exponential

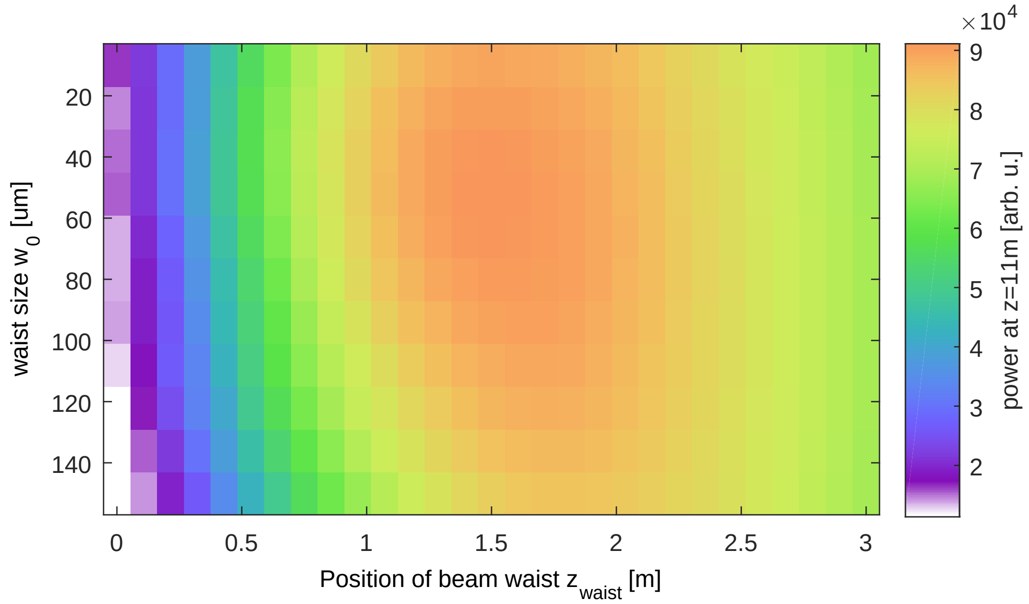

Figure 6.3.: FEL pulse peak power after 11 m of undulator as a position of waist position and size.

gain has started. The parameter combination that generates the maximum peak power is considered the one with optimum coupling efficiency for the direct seeding.

The parameters corresponding to this optimum coupling and which were used for the design of the monochromator optics are

$$w_0 = 52\,\mu\mathrm{m} \tag{6.7}$$
$$z_{\mathrm{waist}} = 1.5\,\mathrm{m}, \tag{6.8}$$

where z_{waist} gives the position of the waist with respect to the entrance of the first radiator module of the second stage. This point z_{waits} along the undulator will be called interaction point in the following.

6.1.3. The Monochromator Design

The monochromator is the most critical part of the experiment since its properties strongly determine the performance of the direct seeded undulator stage. The design presented here adapts the recent soft x-ray self-seeding (SXRSS) design for LCLS at SLAC [86] to serve the energy ranges of FLASH2. It mainly features 4 optical components: A diffraction grating to disperse the radiation and focus it onto a slit, a refocussing mirror $M2$ to focus the radiation at a proper point within the second undulator stage, and two plane mirrors $M1$ and $M3$ that are only used for reflection [86]. Figure 6.4 shows the layout of the designed monochromator system.

The grating that is used is a variable line space (VLS) grating. These gratings have a line space density that is varying with the transverse position along the grating, resulting in slightly different dispersions. The net effect of this change is a focusing of the light pulse in the dispersing plane of the grating.

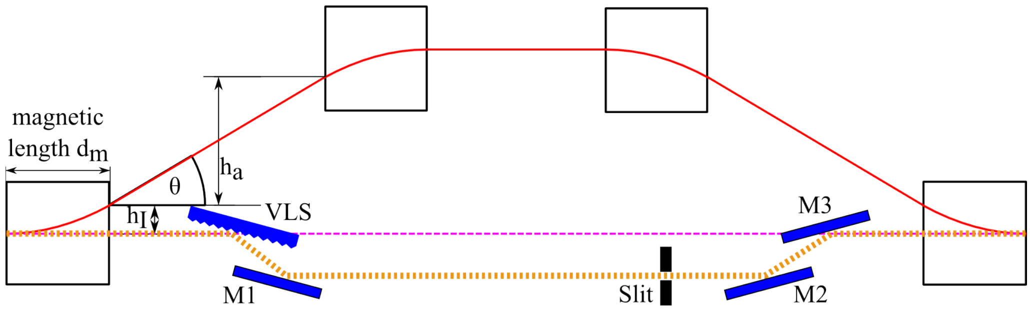

Figure 6.4.: Layout of monochromator. The blue elements are the optical elements, the dotted yellow line the photons. The red line shows the orbit of the electrons that bypasses the optical elements using dipoles shown as white squares.

The focusing properties of the monochromator have been optimized with the optical ray-tracing software ZEMAX[1]. The parameters of the optical components are given in Table 6.1 for the final monochromator design.

6.1.4. FEL Simulations – First Undulator Stage

The FEL process of the first undulator stage starts up from noise. The FEL simulations have been conducted using the FEL simulation code GENESIS 1.3. The input parameters of the Gaussian beam can be found in Table 6.3. Fifty different shot noise seeds have been used in order to obtain statistical parameters for the SASE pulse that can be used in the estimations of the photon pulse properties for the second undulator stage. The average pulse energy generated after 9 undulator modules is 3.26 µJ. An average spectrum of the fifty SASE pulses is shown in Fig. 6.5. The relative width of the spectrum is $\left(\frac{\Delta\lambda}{\lambda}\right)_{\mathrm{SASE}} = 0.22\%$.

We will later see that the number of undulator segments in the first stage is chosen to generate a couple of hundreds of kilowatts peak power for the seed in the second undulator stage. More undulator modules increase the thermal stress on the optical components and eventually exceed their damage thresholds, while less segments would lead to a seed peak power that is not sufficient anymore.

6.1.5. Choice of Grating Constant

Choosing a grating constant for the monochromator grating that introduces the necessary diffraction is a compromise between two effects. On the one hand, the grating constant should be high to ensure a high dispersion at the slit. This would relax the conditions on the focussing optics as well as damage thresholds on the optical elements. On the other hand, higher grating constants decrease the reflectivity and therefore the transmission T_{m} of the grating.

The reflectivity of the grating is the ratio between incoming power and reflected power $R_{\mathrm{g}} = P_{\mathrm{r}}/P_{\mathrm{i}}$ [87]. This characteristic is dependent on the choice of material, coating thickness, incident angle, groove depth, groove width, and spacing. Since a complete

[1]ZEMAX is an optical ray tracing code by Optima Research Ltd.

Parameter	**Value**
grating position	0.42 m
incident angle	85.3°
sagittal radiuas	734 mm
tangential radius	0 mm
line density G	2000 l/mm
line density gradient G_1	5.77 l/mm^2
mirror **M1** position	0.69 m
angle	80.7°
slit position	1.41 m
mirror **M2** position	1.79 m
angle	87.7°
sagittal radius	317 mm
tangential radius	17090 mm
mirror **M3** position	2.64 m
angle	87.7°

Table 6.1.: Parameters of optical components of the self-seeding monochromator. All positions are given along the beam path of a 5 nm beam with respect to the exit of the quadrupole after the last undulator module of the first undulator stage.

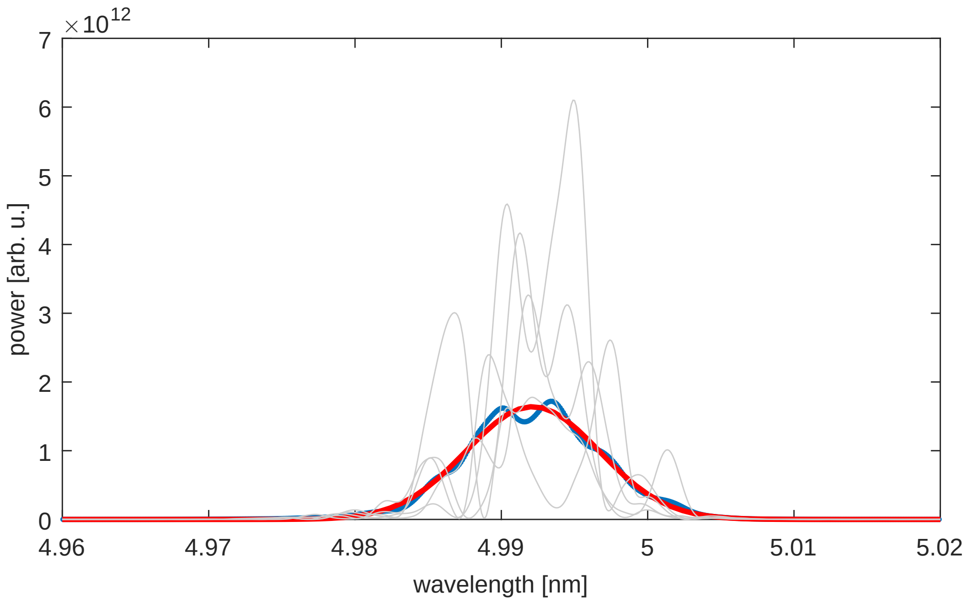

Figure 6.5.: Average spectrum of 50 SASE FEL pulses simulated with GENESIS 1.3. The blue line shows the mean spectrum of 50 different simulations with different shot-noise profiles. The red curve is a Gaussian fit to the average spectrum. The grey curves show 5 single-shot spectra.

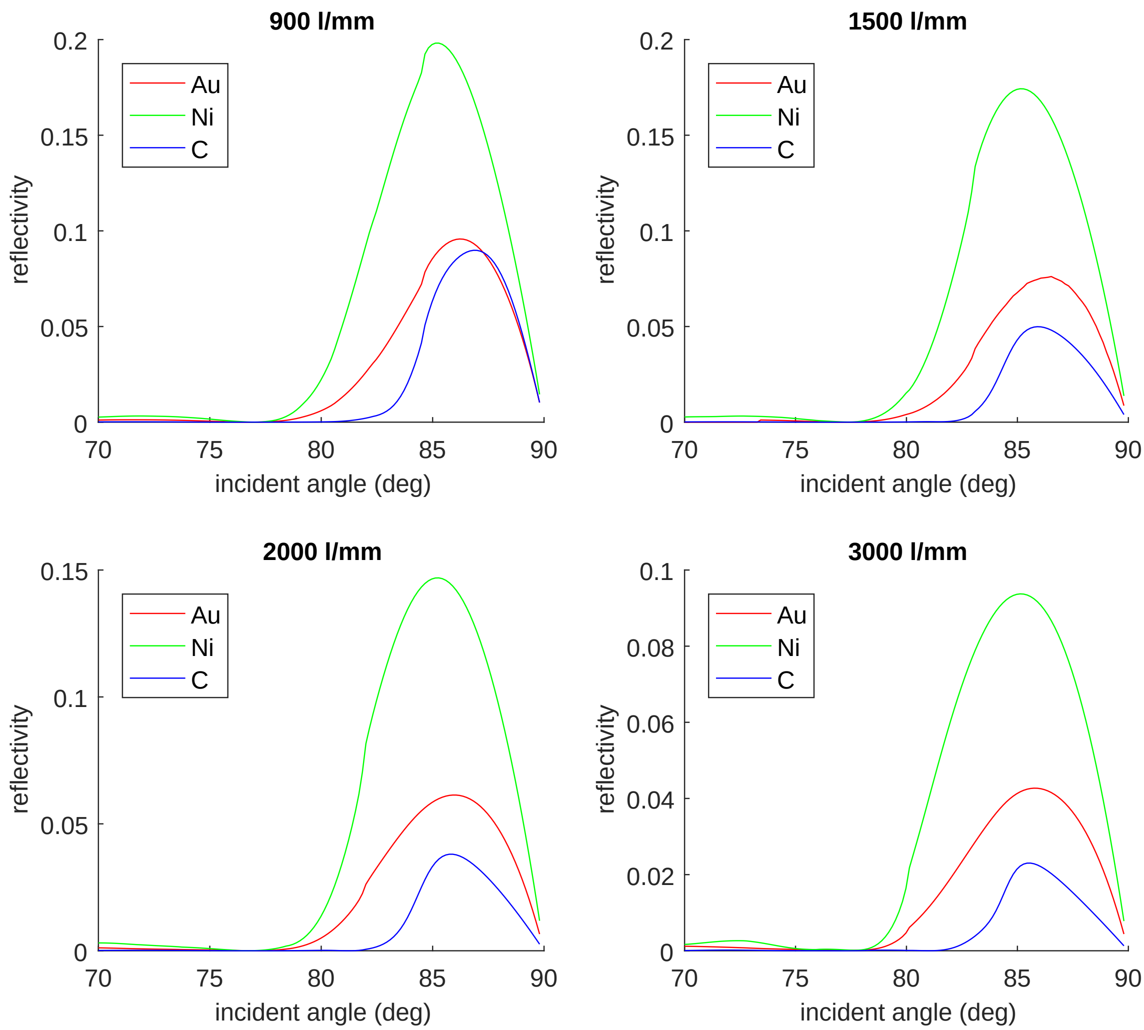

Figure 6.6.: Reflectivity for Au, Ni and C for different line densities as a function of the incident angle. Every plot shows the optimum coating thickness. The incident angle is the angle between the direction of the radiation and the surface normal of the grating.

material	900 l/mm	1500 l/mm	2000 l/mm	3000 l/mm
Gold (Au)	65	60	10	5
Nickel (Ni)	60	45	20	15
Carbon (C)	5	5	10	25

Table 6.2.: Optimum thicknesses in nm for all materials and groove densities analyzed.

multidimensional optimization of these parameters is beyond the scope of this thesis, the optimization has been conducted in two steps. In a first step, the optimum material thickness is found, and in a second step the groove depth, width, and spacing are optimized. The calculations are conducted with the code REFLEC by F. Schäfers [88].

The materials that have been studied are Gold (Au), Nickel (Ni) and Carbon (C). To limit the number of simulations that have to be conducted, the analyzed groove densities G are 900 l/mm, 1500 l/mm, 2000 l/mm and 3000 l/mm. The thickness for all materials has been scanned between 5 and 75 nm. Figure 6.6 shows the reflectivity for all materials and groove densities as a function of the incident angle for a wavelength of 5 nm. Each plot shows the reflectivity for the different materials after optimizing the layer thickness. Table 6.2 shows the optimum thicknesses for every case. The material with the best reflectivity is Nickel. As can be seen from the plots, the reflectivity decreases with higher groove density. Before we can study the impact of the groove width, depth, and spacing, a grating constant has to be chosen to reduce the calculation efforts.

As stated before, a small groove density will be a problem on the optical elements of the monochromator. In the ideal case, only one mode is cut from the spectrum. Its width corresponds to the upper limit of the resolving power given in Eq. (6.6). A small density introduces only a small amount of dispersion, the beam would have to be strongly focused at the slit and the energy of one SASE mode would hit this small area. Note that this is not only the case for the passing radiation, but especially for the radiation blocked by the slit in the monochromator. The flux of the photon pulse is defined as

$$F = \frac{E_\mathrm{p}}{2\pi\sigma_\mathrm{r}}, \tag{6.9}$$

where E_p is the energy of the photon pulse and σ_r is the rms size of the transverse profile of the photon pulse. Figure 6.7 shows the intensity of one SASE mode that is focused down onto the slit to generate a resolving power of $R_\mathrm{m} = 4500$ of the monochromator as a function of the grating constant. The energy of one SASE mode has been estimated from the highest peak in the single-shot SASE spectra to be about 1.2 µJ. The grating and mirror reflectivities are estimated at 14% and 95%, respectively. The width of the slit that is needed to cut out one SASE mode depends on the grating constant and can be found by calculation of the diffraction at the position of the slit

$$D_\mathrm{S} = \left(\frac{\Delta x}{\Delta \lambda}\right)_\mathrm{slit} \approx \frac{L_\mathrm{gs} \cdot G}{\sqrt{1 - (\sin\alpha - \lambda G)}}, \tag{6.10}$$

where L_gs is the distance between grating and slit, α is the angle of the incident photon beam with respect to the grating normal. The slit width is calculated by $\Delta x = D_\mathrm{S}\lambda/R_\mathrm{m}$.

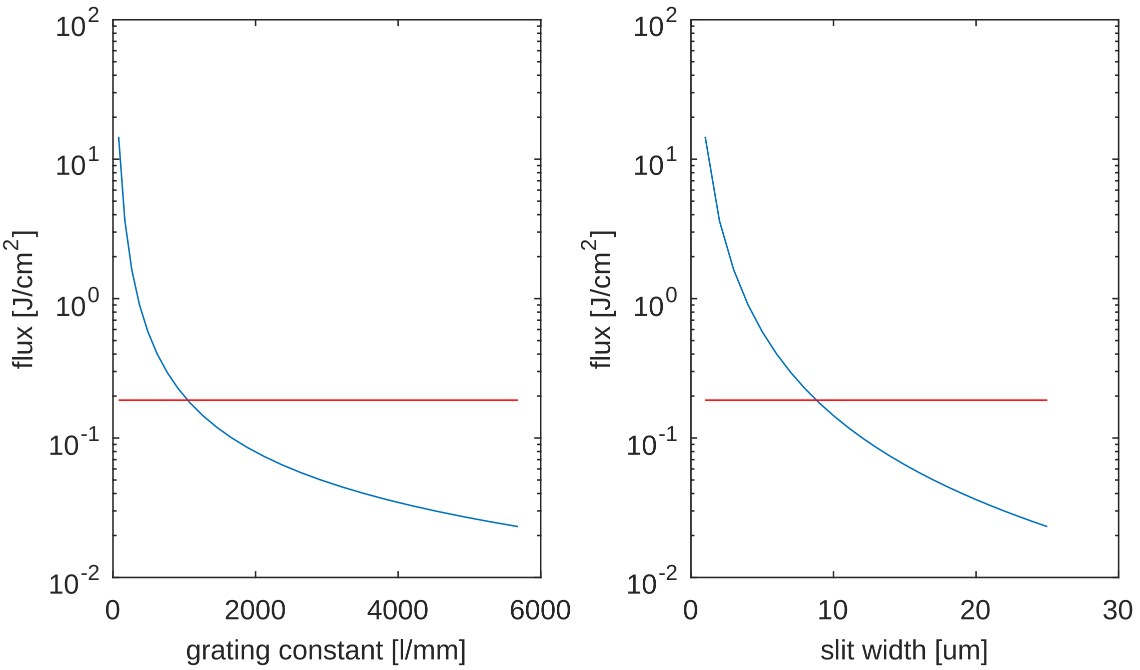

Figure 6.7.: Expected photon flux at the slit in the monochromator as a function of grating constant. The grating constant corresponds to a dispersion that determines the slit width needed for a resolving power of $R_\mathrm{m} = 4500$, see text. The red line shows the damage threshold as discussed in the text. With a proper grating constant chosen from the left panel, the corresponding slit width can be found from the right panel.

A damage threshold that can be found in the literature for optical components at 5 nm for pulses with durations of about 80 fs is $F_\mathrm{th} = (187 \pm 30)\,\frac{\mathrm{mJ}}{\mathrm{cm}^2}$ [89]. A safe choice for the grating constant is $G = 2000\mathrm{l/mm}$, since the expected flux for this grating constant is below $F = 100\,\frac{\mathrm{mJ}}{\mathrm{cm}^2}$ and thus a factor of two below the damage threshold.

With the exception of the slit which is hit parallel to its normal by the photon pulse, the grating is the component of the monochromator most prone to damage. With the chosen grating constant the optimum incidence angle is $\alpha_\mathrm{i} = 85.3°$ with respect to the grating normal. Hence, the illuminated area of the grating is an ellipse. Its semi-minor axis is the rms radius of the photon pulse $\sigma_\mathrm{r,g}$ from the first stage found by FEL simulations of the first undulator stage. The semi-major axis of the ellipse is larger by a factor of $1/\cos(\alpha_\mathrm{i})$. Thus, the beam illuminates area of $A = \pi\sigma_\mathrm{r,g}^2/\cos(\alpha_\mathrm{i}) \approx 0.86\,\mathrm{mm}^2$. Hence, the flux on the grating just is about $0.38\,\frac{\mathrm{mJ}}{\mathrm{cm}^2}$ and well below damage thresholds that can be found in the literature [89].

The optimum material for this groove density is Nickel with a thickness of 20 nm. The groove depth, width and spacing has been optimized to reflect 14.7% of the incoming photon pulse energy. With an estimated reflectivity of the mirrors of at least 95%, the optical elements in the monochromator show a total transmission through the device of $T_\mathrm{m} = 0.147 \cdot 0.95^3 = 12.6\%$

We now have defined all parameters to calculate the energy of the monochromated FEL

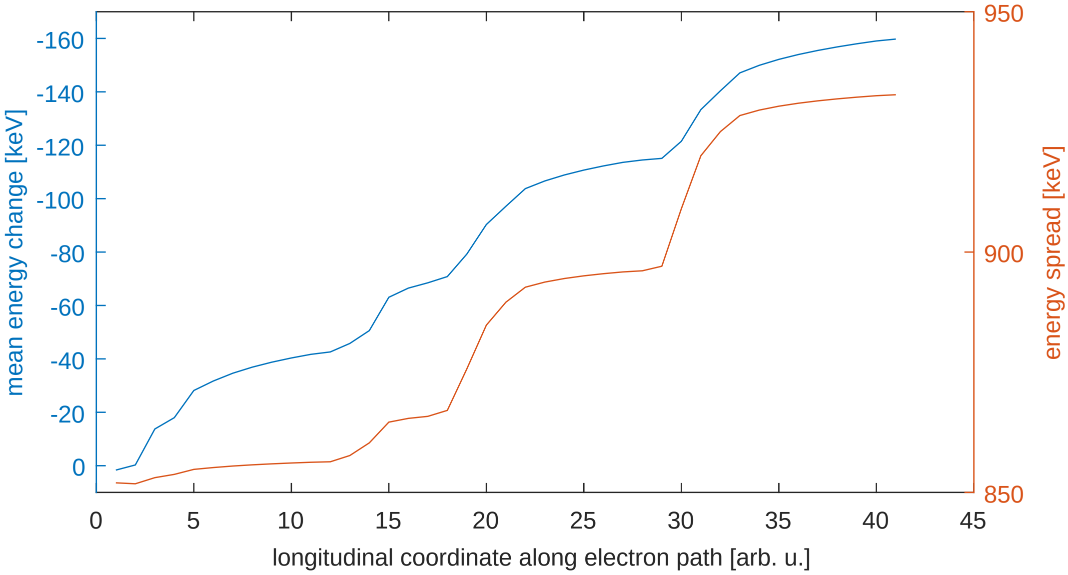

Figure 6.8.: Energy deviation and rms energy spread along the electron path in the chicane. The simulation was conducted using CSRTrack.

pulse that should start the lasing process in the second undulator stage. Using Eq. (6.4) we get

$$E_{\mathrm{in}}^{(2)} \approx 41.5\,\mathrm{nJ}. \tag{6.11}$$

To completely model the photon pulse in the second stage, information on the longitudinal profile is necessary. The mode cut out from the spectrum is longitudinally coherent. The duration of resulting pulse, is thus close to its Fourier limit of 33 fs full width at half maximum. The pulse, however, will be elongated by the diffraction process of the grating. The exit angle of this dispersive element is different from the incident angle and light diffracted by different grooves of the grating has to traverse a different path length. The photon pulse will experience a pulse front tilt and will be elongated by an amount of $\Delta T = R\lambda/c \approx 75\,\mathrm{fs}$. This results in a total pulse length of $\Delta t = 109\,\mathrm{fs}$. For the simulation of the a Gaussian laser pulse with this length, a peak power of 390 kW, corresponding to the energy after the monochromator, has been used. The effect of the pulse front tilt thus has not been incorporated completely and the result of the simulation will be an overestimation of the performance.

6.1.6. CSR Effects in Chicane and Chicane Design

A four-dipole chicane for the electron beam bypasses the monochromator setup and smears out any micro-bunching generated in the first undulator stage of the self-seeding setup. It also has to delay the electron bunch by the same time the photon pulse is delayed by the monochromator in order to ensure longitudinal overlap in the second undulator stage. Since the time difference Δt of electrons and light moving on the same path within a couple of meters is in the femtosecond range, it is sufficient to consider the path length difference $\Delta L = 2.835\,\mathrm{mm}$ of the straight electron path and the light path through the

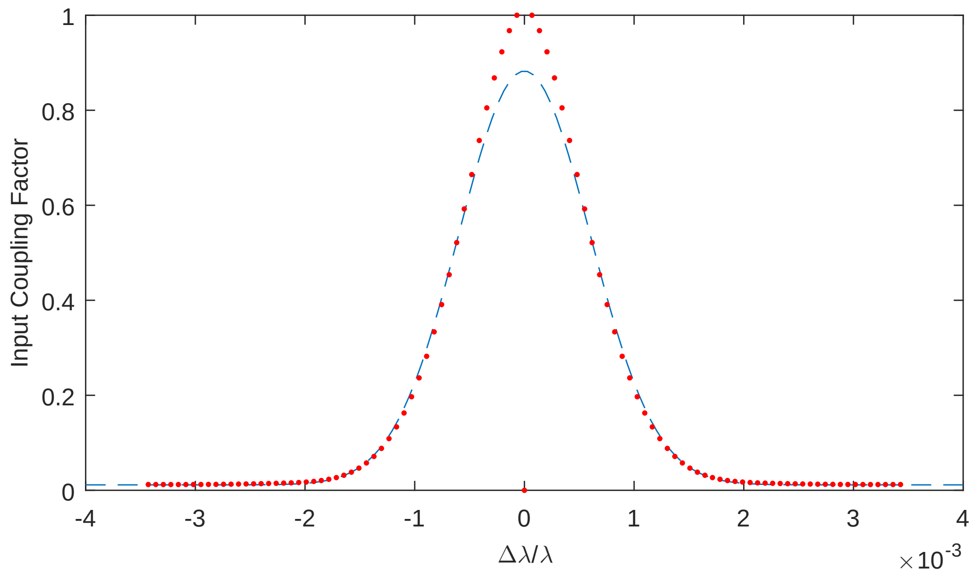

Figure 6.9.: Resolving power of monochromator setup in the absence of a slit. The red dots show the normalized power of GENESIS 1.3 simulations after 10 m of undulator corresponding to a coupling factor of the input seed pulse, the dashed blue line is a Gaussian fit to the data that is used to determine the resolving power $R_{\text{min}} = 711$.

monochromator

$$\Delta t \approx \frac{\Delta L}{c} = 9.46\,\text{ps}. \tag{6.12}$$

The chicane thus has to introduce a timing difference of Δt with respect to the straight electron path. A possible c-shaped chicane as depicted in Fig. 6.4 could introduce this timing chicane with 300-mm-long dipoles and a magnetic field strength of 0.65 T at an electron energy of 1.1 GeV. The two dispersive paths must have a length of 700 mm each, while the central path has a length of only 660 mm.

An electron bunch as short as the one used for the self-seeding setup might be subject to energy loss and energy spread blow up due to coherent synchrotron radiation [90, 91]. The electron bunch from the first undulator stage has been tracked through the chicane described above using the particle tracking code CSRTrack [92]. Figure 6.8 shows the decrease in mean energy and increase of the energy spread along the chicane. While the energy loss of only 160 keV can be neglected, the rms energy spread increase from $\sigma_{\text{W}} = 800\,\text{keV}$ after the first undulator stage to $\sigma_{\text{W}} = 930\,\text{keV}$ after the chicane has been incorporated to the electron bunch parameters used in numerical simulations of the second undulator stage.

6.1.7. Resolving Power of Electron Bunch

If the slit of the monochromator is opened to a width where the complete spectrum of the first undulator stage can traverse the monochromator, the electron bunch will act as a slit in the second stage. The grating of the monochromating setup still introduces diffraction

First stage	
number of undulator modules	9
undulator period λ_u	3.14 cm
undulator parameter K	0.98
undulator model length L_u	2.3864 m
number of periods per module N_u	76
length of drift space between modules L_{drift}	0.9106 m
Second Stage	
number of undulator modules	9
undulator period λ_u	3.14 cm
undulator parameter K	0.98
undulator model length L_u	2.3864 m
number of periods per module N_u	76
length of drift space between modules L_{drift}	0.9106 m
Electron Bunch	
peak current I_{peak}	2.5 kA
bunch duration $\sigma_{t,e}$	20 fs
electron energy W_0	1.1 GeV
energy spread (first stage) σ_E	250 keV
energy spread (second stage) σ_E	930 keV
normalized emittance ϵ_n	1.5 mm mrad

Table 6.3.: Input parameters for GENESIS 1.3 simulations.

and the size of the radiation in the second stage can be bigger than the electron bunch size. The electron bunch, however, can only interact with the radiation that is in overlap with it. This way, there is a lowest possible resolving power R_{min} of the monochromator setup that is influenced by the transverse sizes of electron and photon beam as well as the dispersion induced by the grating.

An estimate for this resolving power can be found by a set of GENESIS 1.3 simulations where the photon pulse gets a horizontal offset in the dispersing plane of the monochromator [93]. The horizontal position of the photon pulse can then be related to a wavelength by the dispersion induced by the grating. Figure 6.9 shows the result of the simulations with a Gaussian fit that is used to determine the minimum resolving power:

$$R_{min} = 711. \tag{6.13}$$

6.1.8. FEL Simulations – Second Undulator Stage

The properties of the light that serves as seed for the second undulator stage have been described above. Since it has been modeled as a Fourier-limited Gaussian photon pulse, this simulation merely serves as an optimistic estimate of the performance of the second undulator stage. The electron bunch uses the estimation of the projected slice parameters

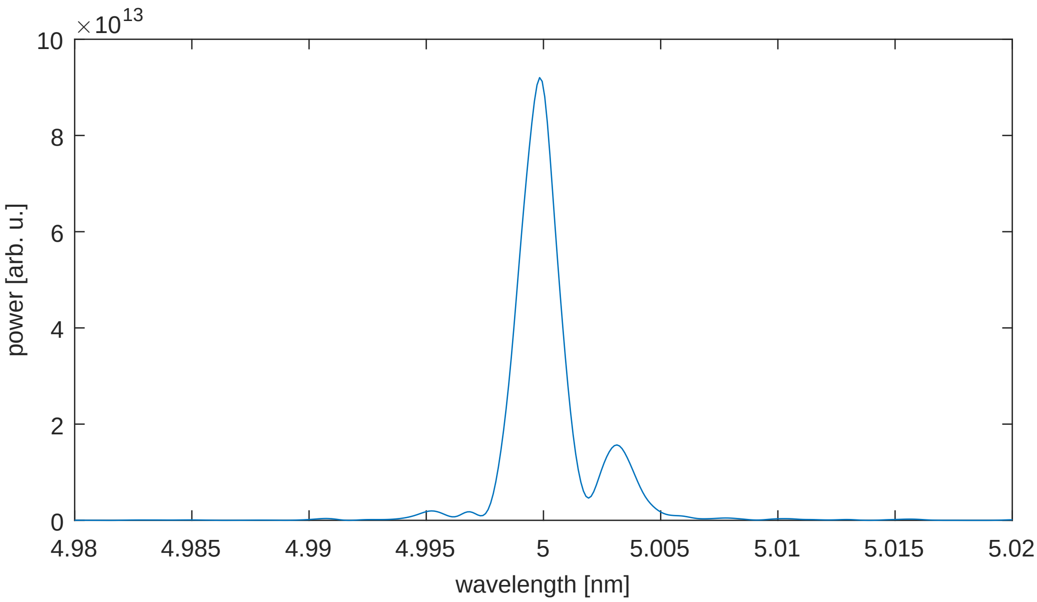

Figure 6.10.: Single-shot spectrum of final undulator stage after 9 undulators. The spectrum is very narrow compared to the SASE spectrum, since most of the generated power is confined to the self-seeded central spike.

from the CSRTrack simulation of the monochromator chicane, but is newly generated by GENESIS 1.3 at the beginning of the simulation. The parameters for the simulations are shown in Table 6.3.

Figure 6.10 shows the spectrum of the generated photon pulse from the second undulator stage after 9 undulator segments where the beam starts to saturate at a peak power of 1.5 GW. The relative spectral width of the central spike is 0.034% and thus a factor of 6.5 more narrow than in the SASE case. The central spike carries about 80% of the shot's energy. The increase in spectral brightness compared to a SASE pulse of the same energy is thus a factor of about 5. Some residual SASE background towards higher wavelength is still present that is also observed in other theoretical and experimental work [86, 47]. A proposed solution to eliminate this background is a monochromator for the FEL pulse of the second undulator stage [86].

The setup presented fills 19 out of the 20 available undulator slots. Both stages contain 9 undulator modules and the monochromator and chicane fill one slot in the center.

The calculations presented here are conducted for a photon wavelength of 5 nm. The monochromator can be built to work with wavelength that deviate about 1 nm from its central wavelength, though the efficiency might be less. A wider range of tuning might involve the motorization and even replacement of the optics.

This limited tunability certainly is not the only drawback of the self-seeding option. It should be noted, that the case shown here operates close to the single-shot damage thresholds of the optical components. An operation of these components for high repetition rates might increase the stress on the material and decrease the damage thresholds. The optical components are not the only parts of the setup which have to meet high demands. The electron bunch has a peak current of 2.5 kA which is at the limits of the capabilities of FLASH. Also the demands on slice parameters are quite high. If collective effects deteriorate the quality of the high peak current core region of the electron beam, the FEL power gain might not be sufficient anymore for the self-seeding option to work.

Though there are a few drawbacks, the setup has one benefit over the seeding schemes that involve an external seed laser. The repetition rate is only determined by the electron bunch pattern and the scheme is ready for a future quasi-cw operation.

6.2. HGHG Seeding at FLASH2

One possibility for the FLASH2 seeding upgrade is the HGHG option. In this option, the FLASH2 SASE beamline would be extended by an additional chicane and a special undulator to modulate the electron beam which then radiates in the main undulator. Since this part of the thesis was conducted in the framework of the FLASH2 Seeding Conceptual Design Report, there have been some goals defined.

The main goal of this first stage project is to define a seeding scheme that is able to deliver a seeded photon beam below 20 nm wavelength at a repetition rate of 100 kHz. For simplicity, the design chosen concentrates on a single-stage HGHG setup with one modulation and one radiation process. The scheme, however, is extendable to an EEHG setup in the future to reach lower wavelength.

Since the FLASH2 beamline is already operated in SASE mode, some additionally boundary conditions have to be fulfilled in the design. Firstly, FLASH2 has to maintain its SASE capability, thus no existing undulator modules can be excluded from the seeding design. Secondly, the energy of the electron bunch is determined by the wavelength that will be served at the parallel FLASH1 beamline and is thus not a free parameter when choosing the wavelengths. It is expected that FLASH will most frequently operate at electron energies of about 1 GeV in the future.

An HGHG setup can only lase on discrete harmonics of its seed laser wavelength. For the presented setup, where the 14th harmonic is the lowest possible one with the current FLASH2 radiator segments, there might be only a few wavelengths that can be used, since HGHG gets less efficient at higher harmonics. For a wider tuning range a tunable seed laser system has to be incorporated into the design.

6.2.1. Modulator and Conversion Scheme

The installed FLASH2 undulators have a period length of $\lambda_\mathrm{u} = 31.4\,\mathrm{mm}$ and a tunable gap to reach a maximum undulator parameter of $K_\mathrm{max} = 2.8$ [24]. Assuming a wavelength of $\lambda_\mathrm{seed} = 266\,\mathrm{nm}$ of the modulating laser light one can estimate the harmonics the radiator can be tuned to. Fig. 6.11 shows the available harmonics under the assumption that the minimum K_min of the undulator should be at least about 1 to ensure a effective FEL process. The lower end of the shown area corresponds to K_max, while the upper one corresponds to K_min. To reach below 20 nm one has to reach at least the 14th harmonic as shown by the red line in the figure. For the frequent working point of about 1 GeV of beam energy the 14th harmonic thus lies within the capabilities of the FLASH2 main undulator and is also the lowest possible harmonic.

According to Eq. (3.8), the amplitude of the induced energy spread has to exceed the uncorrelated energy spread by a factor of n to obtain a usable bunching factor on this harmonic. The expected local slice energy spread in the FLASH2 beamline is about 70 keV at the point of modulation [94], thus the induced energy modulation amplitude has to be $\geq 1.0\,\mathrm{MeV}$.

Figure 6.12 shows the energy modulation induced by a laser pulse with a power of 80 MW as a function of undulator period length and number of undulator periods. The black line represents an undulator length of $N_\mathrm{u}\lambda_\mathrm{u} = 2.5\,\mathrm{m}$, all points above the black line

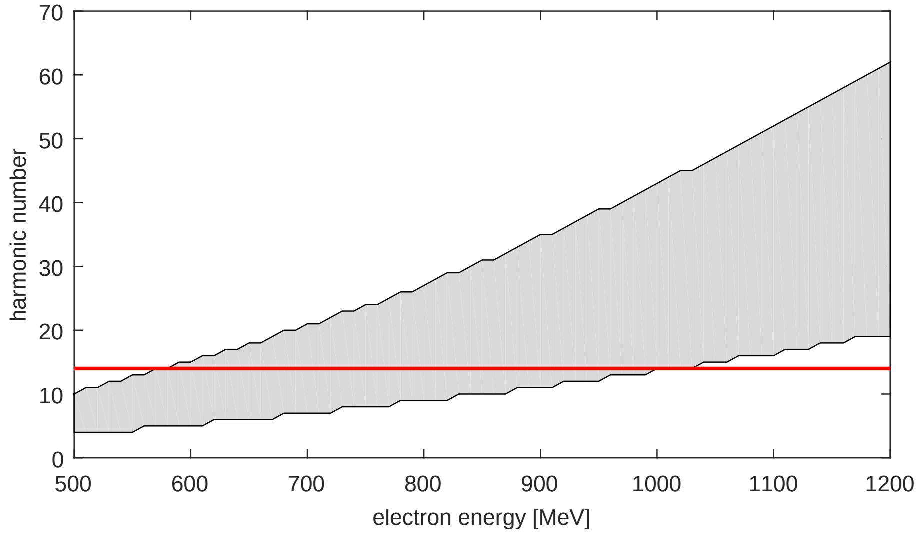

Figure 6.11.: Achievable harmonics in the radiator at FLASH2 single-stage HGHG setup. The grey area shows the achievable harmonics for a radiator undulator parameter $1 < K < 2.8$. The red solid line shows the harmonic that has to be reached to get below 20 nm with a seed laser wavelength of 266 nm.

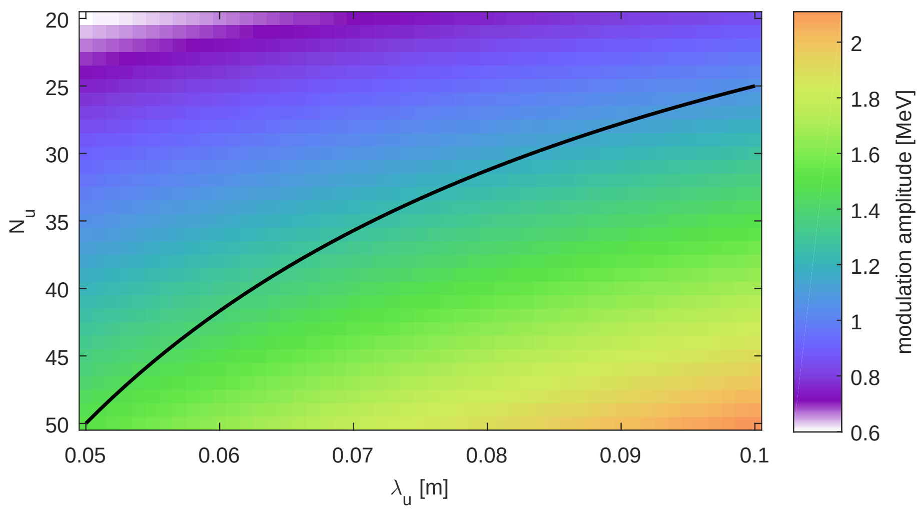

Figure 6.12.: Induced energy modulation amplitude of the electron beam after an undulator of period length λ_u and number of period N_u. To fit into the lattice of FLASH2 the undulator should not be longer than 2.5 m, which corresponds to the area above the black line.

thus represent undulators fitting into the FLASH2 FODO lattice period. For the FLASH2 modulator a period of $\lambda_\mathrm{u} = 0.075\,\mathrm{mm}$ with $N_\mathrm{u} = 30$ periods was chosen.

While the presented plot only shows the modulation amplitude for an electron energy of 1 GeV, the scheme should still work with higher energies. Choosing a smaller undulator period would allow for slightly higher modulation amplitudes, but will prevent to reach suitable undulator parameters at higher electron energies, since the maximum on-axis magnetic peak field of a state-of-the-art permanent undulator magnet structure is about 1.3 T. Thus for the experiment to remain adaptable to higher electron energies, the slightly worse modulation amplitude can be tolerated.

6.2.2. Numerical Simulations

In order to study the HGHG scheme, numerical simulations have been performed. While both, the modulator and the radiator simulations, have been conducted with GENESIS 1.3 [82] the dispersive section has been modeled using a simple linear transfer matrix formalism, which is incorporated into GENESIS 1.3.

This approach, however, neglects collective effects of the electrons in the chicane. A comparison between tracking the particles with the numerical code CSRtrack, that incorporates these collective effects, has shown that there are small differences in both transverse beamsizes as well as energy loss of the microbunched beamlets on the order of about 500 keV.

As shown in Fig. 6.13, collective effects can however be neglected. The transverse deviations occur in parts of the bunch that are not seeded and are in the order of 2-3 % and thus well below the precision that can be controlled in the experiment (see 6.2.2.1). The energy drop of the electrons due to CSR effects in the last dipole bend of the chicane were predicted to be on the order of 100 keV by CSRtrack. This is well within the FEL bandwidth and much smaller than the energy spread induced by the seeding laser and is thus neglected.

6.2.2.1. Electron Beam and Optics Matching

The electron beam that is used for the simulation was tracked through the complete accelerator and FLASH2 extraction [94]. The beam is dumped at the entrance of the modulator and all beam properties have been evaluated on a slice by slice basis. This procedure allows to generate the beam according to its statistical properties at the entrance of the modulator. This is important since the FEL process is started by noise of the longitudinal electron positions. One has to carefully generate the electron beam to avoid numerical noise that exceeds the shotnoise of a realistic beam. The generation of the particles is then done by GENESIS 1.3 according to [96] to ensure a small numerical noise up to the 14th harmonic of the laser wavelength.

While it is straight forward to match an electron beam that has a constant beam size and emittance, it is more difficult to match a realistic start-to-end beam. For the seeding process to work most efficiently it is beneficial for the central high peak current region to be matched. In an experiment, one would however match the complete electron beam when using multiple screens or quadrupole scan methods. This means that the projected

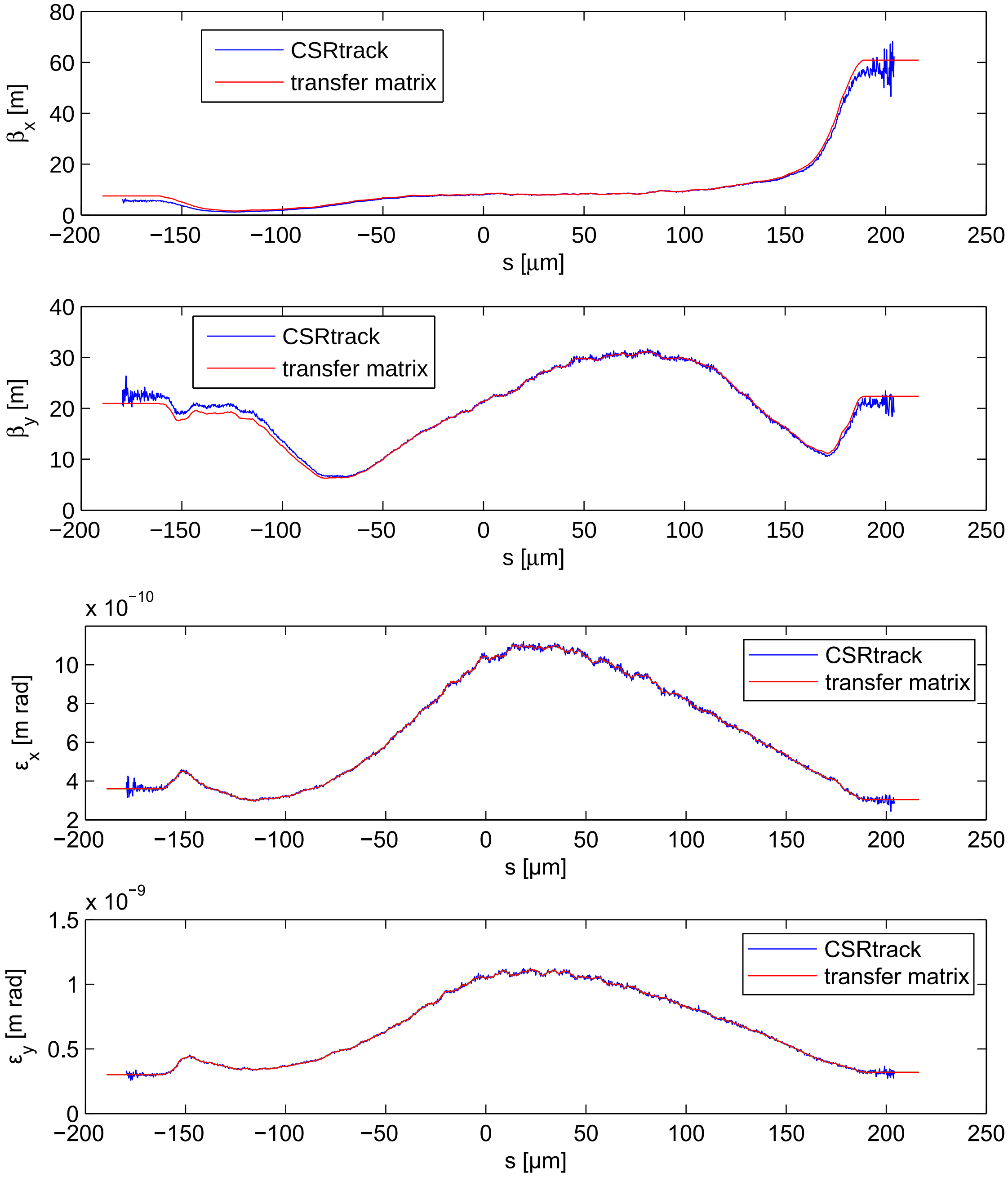

Figure 6.13.: Comparison of slice-by-slice bunch properties from propagation by transfer matrix algorithm and propagation using CSRtrack. There are no significant differences in emittance or beta function in the lasing parts of the bunch. [95]

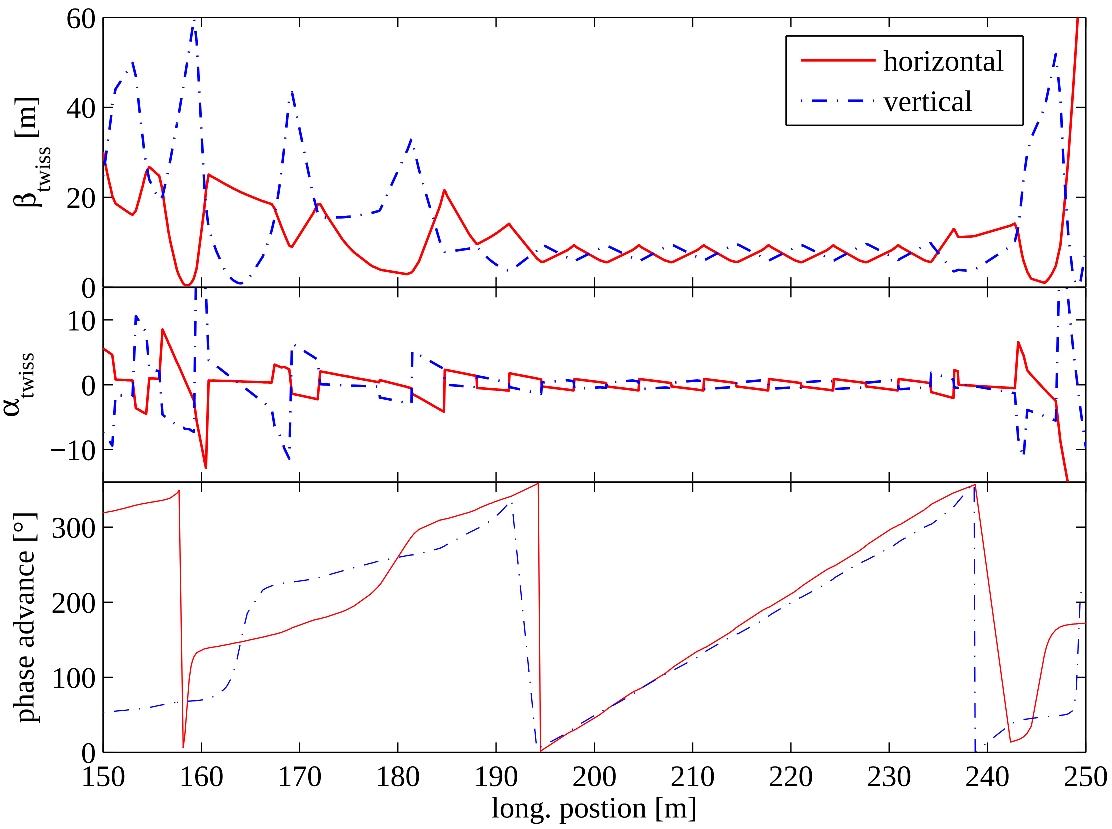

Figure 6.14.: Evolution of optical functions and phase advance along the HGHG seeding section. The SASE undulator starts at 195 m.

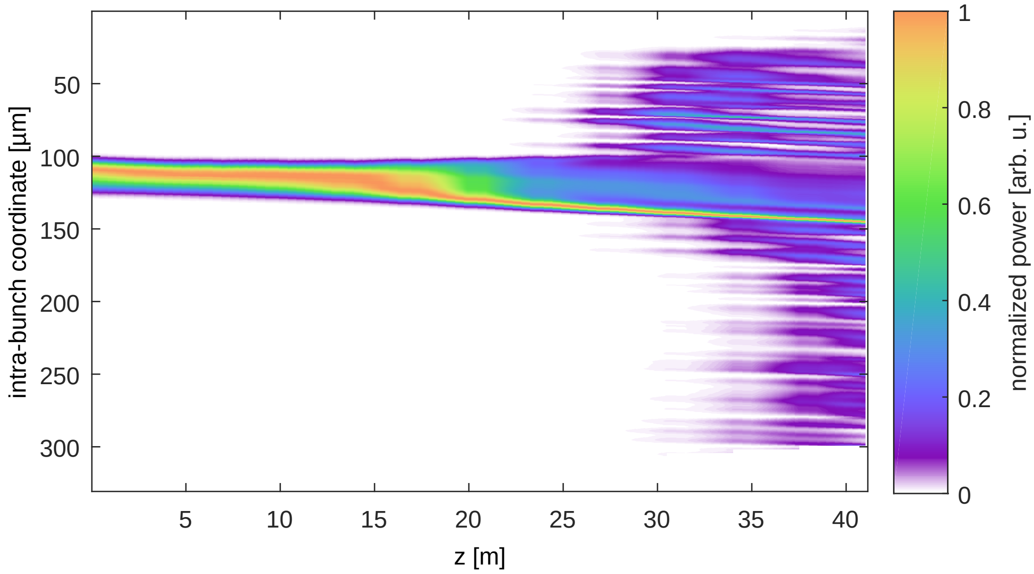

Figure 6.15.: Normalized FEL pulse power as a function of intra-bunch coordinate s and the longitudinal coordinate z. The power was normalized for each integration step.

optical functions of the complete beam are matched, while the matching of the individual slices might differ.

In the simulations shown below, the complete bunch has been matched in front of the radiator using a transfer matrix. In an experiment this will have to be done by manipulating the upstream quadrupole magnets. Figure 6.14 shows the optical functions along the FLASH2 beamline that were used during the simulations. The phase advance in the radiator has been chosen to be 60°as in standard SASE operation.

6.2.2.2. Working Point Simulation

Since the HGHG option for FLASH2 is supposed to have the potential to deliver seeded FEL pulses with a repetition rate up to 100 kHz, it is of use to choose the seeding laser power as low as possible to ease the requirements on the laser system. The GENESIS 1.3 simulation of the modulator has shown that a bunching factor on the 14th harmonic of the 266 nm seed laser of $b_{14} \approx 0.08$ can be achieved with a input seed laser power of $P_\mathrm{L} = 80\,\mathrm{MW}$ and a dispersive chicane strength of $R_{56} = -58\,\mu\mathrm{m}$.

Figure 6.15 shows the normalized FEL pulse power as a function of the longitudinal position in the undulator z as well as the intra-bunch coordinate s. The electron bunch is seeded between $s = 100\,\mu\mathrm{m}$ and $s = 150\,\mu\mathrm{m}$. Fig. 6.16 shows power and energy gain curves of the seeded and SASE part independently. Since the undulator is long enough for SASE to run into saturation in the parts of the bunch that are not seeded, the power contrast between the seeded and unseeded part is vanishing. Since the majority of the electron bunch is unseeded, it even overtakes the seeded part in pulse energy. Fig. 6.17 shows vertical cuts through the two-dimensional distribution of Fig. 6.15 that are not normalized in a logarithmic plot. It can be clearly seen how the non-seeded parts of the

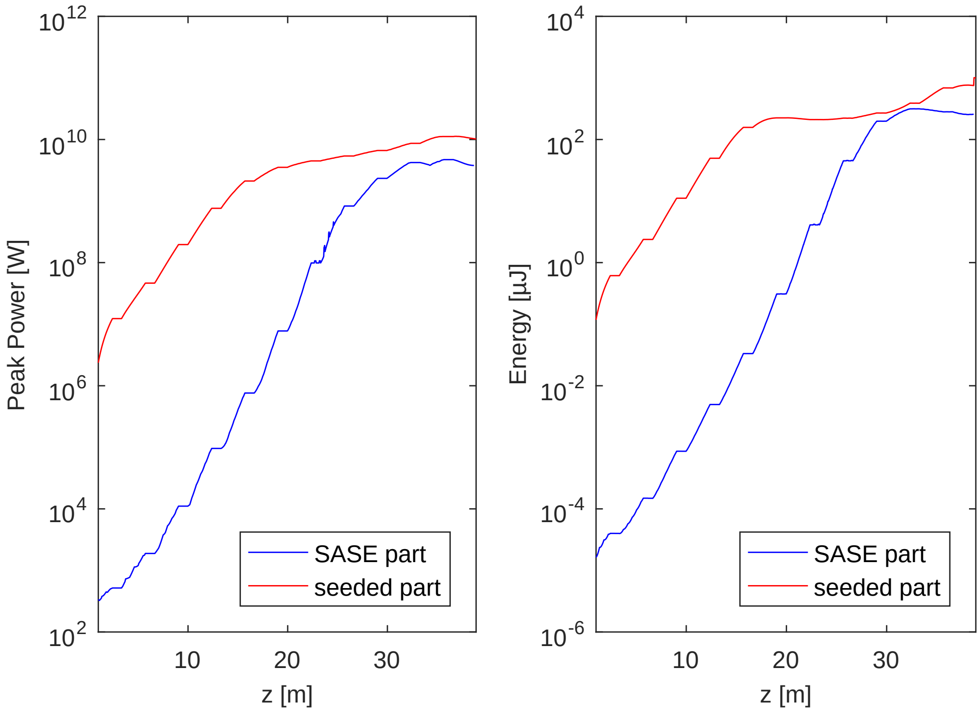

Figure 6.16.: Power *(left)* and energy *(right)* gain curves for the seeded and unseeded part of the electron bunch as a function of z.

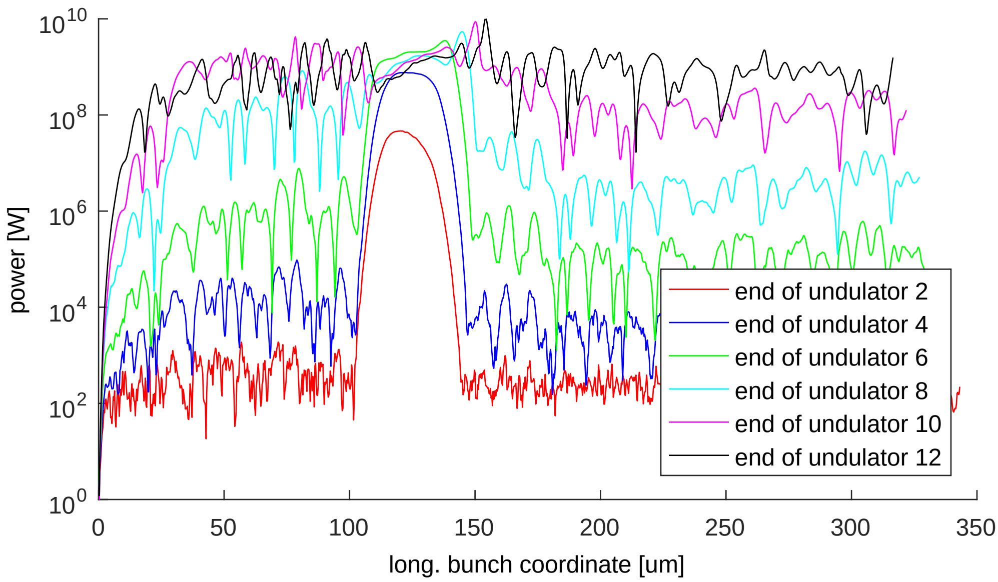

Figure 6.17.: Power of the FEL pulse as a function of s for different z after different number of undulator modules. The curves shown are vertical cuts through the two-dimensional distributions of Fig. 6.16 that are not normalized.

electron bunch catch up to the seeded part in terms of power.

Since experiments need a high power contrast, this undulator configuration is not suitable for an HGHG option. The part of the bunch that starts from shot-noise has the needed undulator length to run into saturation, since FLASH2 is built as a SASE machine. There are a couple of possibilities to face this challenge.

1. To increase the gain length of the FEL process the electron bunch peak current can be lowered to a couple of hundred Amperes. This would increase the saturation length and thus not allow SASE to saturate, while the undulator length would still be sufficient for the seeded part. In this case, the saturation power of the seeded pulse will be lower, since it strongly depends on the current ($P_{\text{sat}} \propto I^{\frac{4}{3}}$).

2. If it is possible to transport the micro-bunched beam along a drift of several meters, only the last couple of undulator modules can be used. This would allow the seeded part to generate a light pulse of a few Gigawatts power, while the SASE part is only starting. A similar option would be to close the radiator segments needed to saturate the FEL with open segments in between. This way the bunching could be preserved more effectively. This technique has been studied for HHG seeding in [97] and would be quite similar in the HGHG case.

3. Since the seeded part runs into saturation within the first half of the main undulator, the subsequent undulator modules can be tapered. When tapering and thus changing the K of the undulator the resonance condition in the SASE part is not longer fulfilled and the SASE gain will suffer.

In this thesis the third option was explored and will be described in the next section.

6.2.2.3. Undulator Tapering

From Fig. 6.16, it can be seen that the FEL process runs into saturation at about 15 m into the undulator. To sustain power gain, the subsequent undulator modules can be detuned to stay in resonance with the lasing electrons that lose energy to the light field [98]. This allows to sustain the maximum bunching over a long distance. A universal scaling function for the undulator parameter as a function of z is given by [99]

$$K(z) = K_0 \cdot \frac{a \cdot (z - z_0)^2}{1 + b \cdot (z - z_0)}, \quad \text{for } z \geq z_0. \tag{6.14}$$

Here, z_0 is the distance traversed along the undulator axis to where the tapering of the subsequent modules starts. The numerical constants a and b determine the profile of the undulator taper and are found by numerical simulations as described below.

As discussed in [99], z_0 should be chosen a few gain lengths before saturation to efficiently trap the lasing portion of the electron bunch. In the case presented here, there is another condition to the undulator tapering: The SASE background should be suppressed as early as possible. Thus, the K parameter of the undulators has to to be detuned to generate a wavelength that differs by more than one FEL bandwidth from the initial wavelength as early as possible. In the subsequent optimization it has been found that the most effective

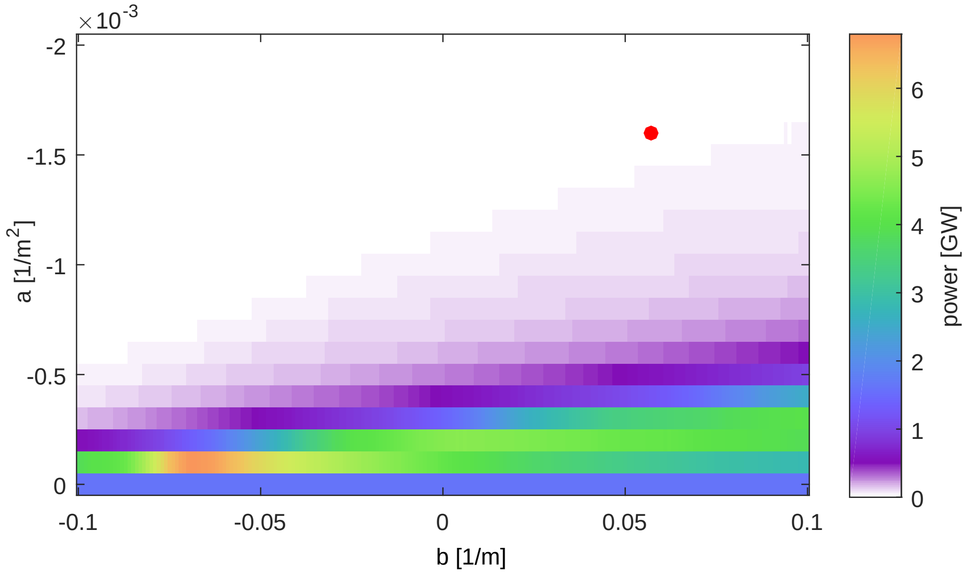

(a) The FEL is starting from noise.

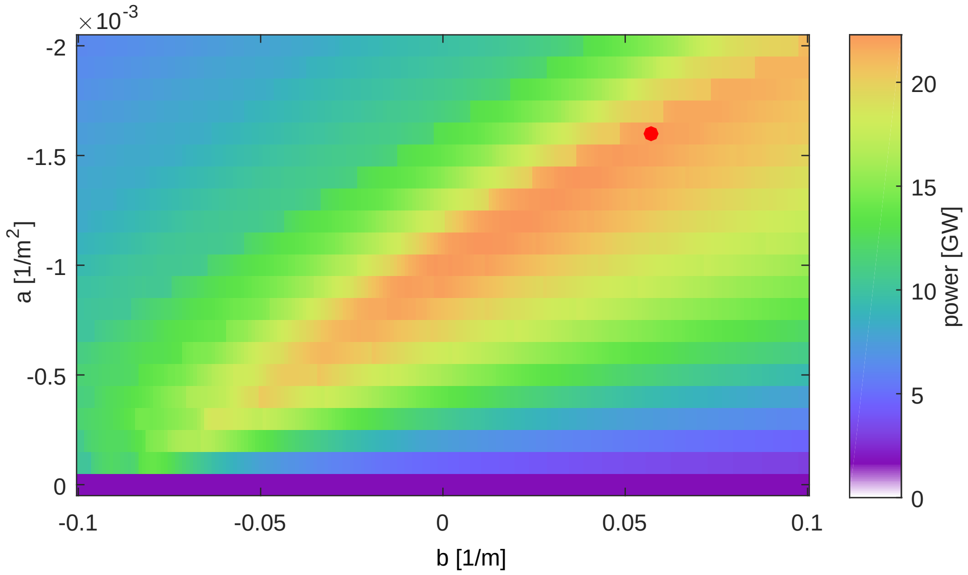

(b) The FEL is seeded as described in the working point simulations before.

Figure 6.18.: FEL power from time-independent GENESIS simulations after 12 undulator segments as a function of the taper constants a and b. The panels show *(a)* an FEL process started from noise and *(b)* the seeded FEL. The red dot in both panels shows the working point chosen for the following plots.

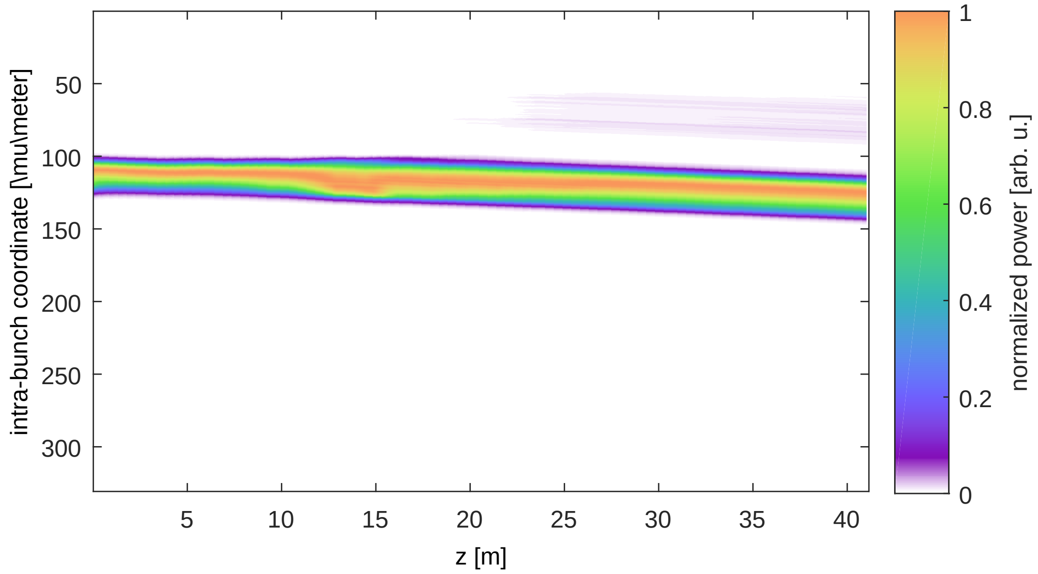

Figure 6.19.: Normalized FEL pulse power as a function of intra-bunch coordinate s and z for the tapered case. The power was normalized for each integration step.

suppression can be achieved for $z_0 = 2 \cdot \lambda_{\mathrm{FODO}}/2 = 6.6\,\mathrm{m}$, where λ_{FODO} is the length of one FODO cell at the FLASH2 beamline.

For the determination of a and b, a series of time-independent GENESIS 1.3 simulations have been conducted. Time-independent simulations assume a periodic electron bunch and thus only simulate one slice of the electron bunch. These are more efficient with respect to computing time than time-dependent simulations that give information of the longitudinal profile of the FEL pulse. Thus, no simulation results from start-to-end simulations can be used as an input for this simulation. The slice parameters used have been derived from the seeded part of the electron bunch shown in the working point simulation. The K parameters have been chosen according to Eq. (6.14) where the center of every undulator module has been chosen for the z coordinate. K_0 has been determined to give maximum power gain of the seeded portion after two undulator modules.

Figure 6.18 shows the FEL power after 12 undulator segments of the optimization for a seeded and a SASE FEL process. Note that this simulation should only show the feasibility of a tapering profile at FLASH2. The taper profile that is needed will of course depend on achieved modulation amplitude and bunching. An experimental realization would most likely be much more empiric than implementing simulated results. An exemplary point chosen for the subsequent illustrations of the method is the red dot in Fig. 6.18, where $a = -1.6 \cdot 10^{-3}/\mathrm{m}^2$ and $b = 5.7 \cdot 10^{-2}/\mathrm{m}$. According to these time-independent simulations, the seeded portion reaches a maximum power of about 21 GW, while SASE will only generate 15 MW.

For this point, a time-dependent simulation has been conducted. Here, a less optimal performance is expected, since longitudinal effects, such as slippage, are taken into account. Figure 6.19 shows the two-dimensional normalized FEL pulse power as a function of s and z. Compared to Fig. 6.15 it can be seen, that the SASE background is less dom-

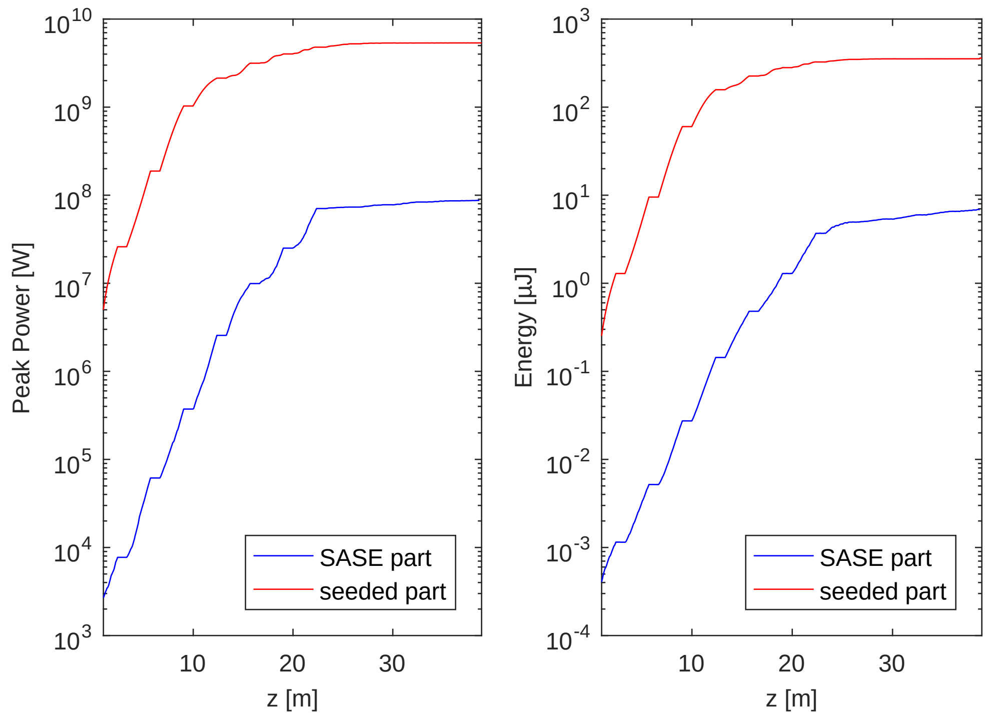

Figure 6.20.: Power *(left)* and energy *(right)* gain curves for the seeded and unseeded part of the electron bunch as a function of z for the tapered case.

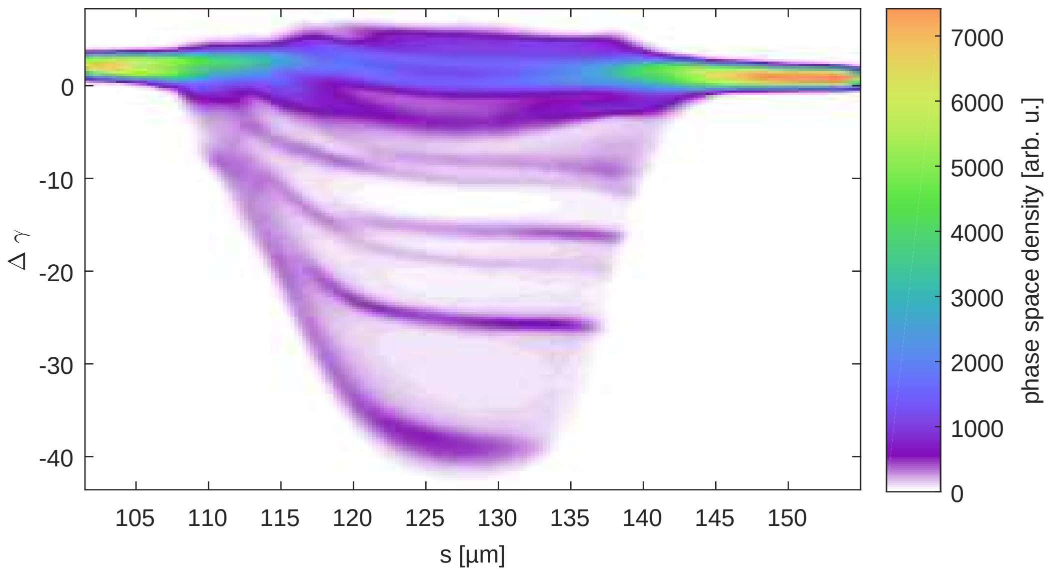

Figure 6.21.: Longitudinal phase space distribution of the seeded part of the electron bunch after 8 undulator modules. Since tapering the undulator is not able to trap all lasing electrons, horizontal stripes form in the phase space distribution.

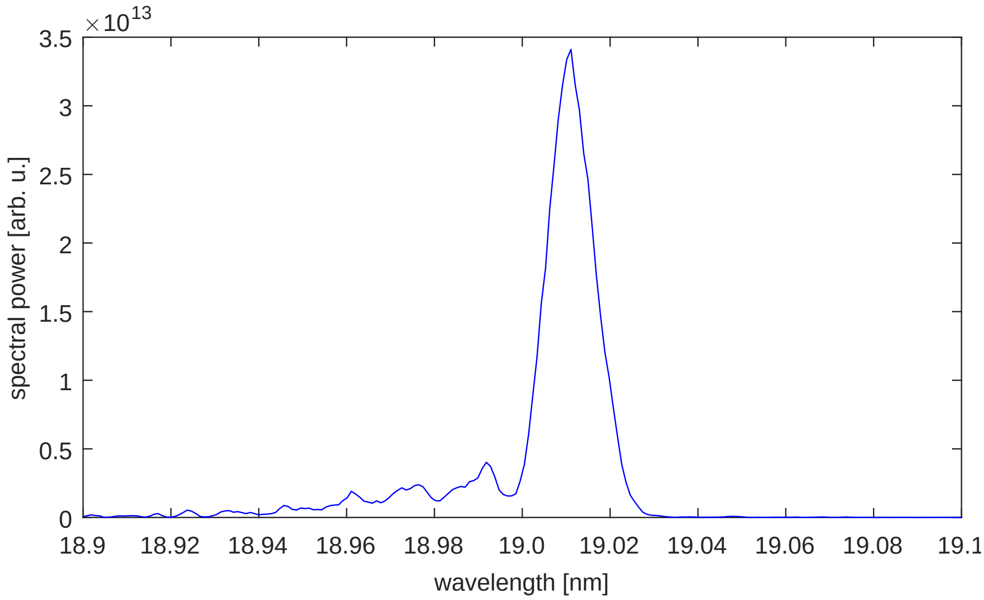

Figure 6.22.: Power spectrum after 12 undulator segments in the seeded and tapered case.

inant, though not completely suppressed. Fig. 6.20 shows the gain curves for the seeded and unseeded part of the electron bunch as a function of z. Figure 6.21 shows the longitudinal phase space distribution of the seeded part of the electron bunch after 8 undulator segments. The phase space forms horizontal stripes from the tapering of the undulator.

In this time-dependent simulation, the peak power of the seeded portion is 5.362 GW, while the SASE background shows a peak power of 87 MW. The generated energies are 360.9 µJ and 7.3 µJ, respectively. This leads to a contrast of the peak power of about 60. The relative spectral width of the seeded peak is about 0.075% and it contains 98% of the pulse energy as shown in the power spectrum after 12 undulator segments in Fig. 6.22.

An option to increase the contrast, while still tapering the undulator, is to shift the seed timing to the region where the SASE radiation is most dominant. Here, though the current is not at its maximum, the energy spread and emittance are smallest. This way the part of the bunch that is best suited for optimum FEL performance would be seeded and the SASE background should be smaller.

The electron bunch used in these simulation has a charge of about 0.9 nC to generate a high-current electron bunch long enough for a cascaded HGHG setup with the fresh bunch technique [94]. Here, the longitudinal position of the electron bunch seeded in the second stage is different from the already deteriorated part of the bunch that lased in the first stage. For this, the part of the electron bunch that is able to lase has to be longer than twice the seed laser pulse length to account for jitter. In contrast, an electron bunch optimized for single-stage HGHG operation may be shorter and show less peak current. A bunch similar to the one used for the HGHG seeding at sFLASH shows slice parameters that are more smooth in the core region of the electron bunch and less SASE background would be generated.

6.3. Summary

The FLASH2 undulator beamline is a second SASE FEL parallel to the FLASH1 main undulator served by the same linear accelerator. Two schemes have been studied to upgrade the beamline's capabilities to serve seeded radiation with higher spectral brightness than in case of a startup from noise, while maintaining the abilitiy to run in SASE mode.

The feasibility study of self-seeding showed that this scheme can increase the spectral brightness of the photon pulse by a factor of 5 compared to a SASE pulse. The restrictions on the electron bunch, however, are quite strict. To reach the necessary output powers, the peak current has to be as high as 2.5 kA while maintaining a low energy spread and the full length available at the FLASH2 beamline has to be utilized for the seeding setup. Though the setup delivers the expected beam quality in the simulations, there is no headroom in any of the parameters if something does not perform as expected.

The HGHG option adds a modulator undulator as well as a bunching chicane to the existing hardware. The FLASH2 main undulators are used as a radiator for this scheme. The electron bunch used in these simulations originates from start-to-end particle tracking and is optimized for a cascaded double-stage HGHG scheme. Though the non-seeded parts of the electron bunch create SASE background radiation, an undulator taper allows to achieve a peak power contrast of 60 of the HGHG signal. If the electron bunch is optimized for single-stage HGHG this power contrast is expected to further increase significantly.

Note that, in the ideal case, a self-seeded FEL pulse will only shows one coherent pulse, since the initial coherent signal covers the enite electron bunch. In the HGHG seeded case some parts of the electron bunch are not modulated and properly bunched. Here, a background of radiation arises that started from noise. The intensity of this background will strongly depend on the electron bunch charge and compression scheme used.

In general, the HGHG option shows better performance with less demands on the electron bunch quality and less space used along the FLASH2 beamline. Future considerations have to focus on the investigation of tolerances of misalignments and unexpected deviations from the electron bunch properties predicted by the start-to-end simulations. Additionally the opportunity of other options to suppress the SASE background have to be explored in order to identify the optimal mode of operation.

7. Summary and Outlook

Free-Electron Lasers use ultra-relativistic electron bunches to generate femtosecond photon pulses with peak powers in the gigawatt range and with wavelengths beyond the capabilities of state-of-the-art laser sources. With electron bunches at kinetic energies above 10 GeV, today's facilities are able to reach sub-nanometer wavelengths. However, when starting the FEL process from noise, the longitudinal coherence of the FEL pulses typically is limited and both, the spectrum and longitudinal profile show a characteristic spiky structure.

The coherence properties of the photon pulse can be significantly improved by starting the FEL process from an external coherent signal. The sFLASH experiment at FLASH at DESY in Hamburg is dedicated to the study of seeding schemes that involve phase-space manipulation techniques. Successful demonstration and a thorough characterization of the High-Gain Harmonic Generation process at sFLASH was presented. The unique hardware configuration at FLASH allows the extraction of slice properties of the electron bunch. The precise characterization of the energy reduction of the electron slice by the FEL process enables the world's first reconstruction of seeded FEL photon pulse profiles from single-shot measurements.

Furthermore, the extraction of the electron slice parameters facilitates the prediction of the lasing performance with a longitudinal resolution of a couple of femtoseconds. The seed laser locally initiates the FEL process, probing the FEL performance and enabling the verification of the extracted emittance profile. This technique allows to determine the initial modulation amplitude induced by the seed laser which is well in line with the measurements on an uncompressed electron bunch. Furthermore, it also demonstrates the value of a transverse deflecting cavity installed downstream of the seeded FEL. It not only gives access to the non-destructive measurements of power profiles, but also enables the study of the slice parameters of the electron bunch and could even be developed to serve as an on-line diagnostic tool. Access to these information may allow to operate a stable seeded FEL at its optimum and could lead to new strategies avoiding electron beam instabilities that prevent reliable seeded operation.

The calibration of the micro-channel plate with transverse deflecting structure data gives access to a big amount of data and eases the measurement of energy gain curves of the FEL process for different seed laser powers. Together with the measurement of FEL pulse lengths and spectra, a numerical simulation could be set up that resembles the experimental data. From these theoretical foundations, a Monte-Carlo simulation based on the Ming-Xie model has been devised that enables the analysis of the FEL power jitter. A careful analysis shows that the jitter mainly originates from laser energy fluctuations. Since a certain amount of power jitter is intrinsic to the laser, a condition on the dispersive strength of the chicane could be derived to minimize its impact on the FEL peak power. The presented analysis is an essential step towards the compatibility of experimental data and numerical simulations. It verifies the given model of the HGHG process and confirms the capabilities of the simulations tools used for sFLASH and FLASH2 seeding.

With the experience gained from the sFLASH experiment a numerical study for a seeding setup at FLASH2 has been conducted. While a self-seeding setup can deliver seeded photon pulses with a high degree of longitudinal coherence at a repetition rate that is determined by the electron accelerator, the gain in spectral brightness compared to SASE operation is merely a factor of 5. The tuning of the wavelength is technically challenging due to the involved photon optics and the setup sets high demands for the electron bunch parameters. An HGHG setup similar to the sFLASH experiment takes less space and can provide higher peak power contrasts than the self-seeded option. While the self-seeding option provides one coherent pulse, the HGHG option provides a seeded pulse with a SASE background. The intensity of this background will strongly depend on the electron bunch charge and compression scheme used. The simulations shown here are a contribution to a conceptual design report that proposes a 100 kHz laser system in its final HGHG stage.

Building on the HGHG plans, the conceptual design also proposes an EEHG scheme for FLASH2 to reach down to 4 nm wavelength. A successful demonstration of an EEHG seeded FEL in the ultra-violet to soft x-ray range, sFLASH will only need minor adjustments of the existing hardware and will underline the claims of the design.

A. Lilliefors Test

The Kolmogorov-Smirnov test is a well established standard method in statistics to determine if a sample of observational data points $x_i, i = 1, 2, ..., N$ of a random variable X is based on a continuous cumulative distribution $F_0(x)$. The drawback of this test is that one has to have precise knowledge of $F_0(x)$ without extracting any knowledge from the observed data set. In case of the laser-electron timing jitter, we test a set of measurements against a normal distribution with a mean μ and variance σ^2 that are derived from these measurements. The Kolmogorov-Smirnov test no longer holds in its classical form. Hubert Lilliefors, however, developed a method based on the classic Kolmogorov-Smirnov test that is suitable for our purposes [83].

The null-hypothesis H_0 this method tests against is

$$H_0 : F_X(x) = F_0(x), \tag{A.1}$$

where $F_X(x)$ is the underlying probability distribution of the observational sample and $F_0(x)$ is the cumulative distribution normal distribution function with $\mu = \frac{1}{N}\sum_{i=1}^{N} x_i$ and $\sigma^2 = \frac{1}{N-1}\sum_{i=1}^{N} |x_i - \mu|^2$. The test uses the cumulative empirical distribution function

$$F_n(x) = \frac{\text{number of } x_i \leq x}{N} = \frac{1}{N}\sum_{i=1}^{N} \mathbf{1}_{x_i \leq x}, \tag{A.2}$$

where $\mathbf{1}_{x_i \leq x}$ is 1, if $x_i \leq x$ and 0 otherwise. The method now constructs a test-statistic D that is given by the maximum discrepancy of the empirical distribution function $F_n(x)$ and the cumulative normal distribution function $F_0(x)$ that it tests against:

$$D = \max_x |F_0(x) - F_n(x)|. \tag{A.3}$$

If D exceeds a critical value D_{crit} the test rejects the null hypothesis. Typical values for D_{crit} for different significance levels α can be found by Monte-Carlo simulations and are available in form of tables from [83].

Figure A.1 shows the empirical cumulative distribution of an example data set with $N = 50$ and the cumulative normal distribution. The black double-arrow is the calculated $D = 0.142$. For a significance of $\alpha = 5\%$ the Lilliefors test rejects the null hypothesis that the test example data originated from a normal distribution, since D exceeds $D_{\text{crit}} = 0.125$. The significance α gives the probability that a correct null hypothesis gets rejected. Thus the chance, that a correct null hypothesis is accepted is $1 - \alpha = 95\%$.

The decision and calculation of the critical values for D is based on the calculation of a p-value that is given in the measurements for laser-electron timing jitter. This value is the probability to observe a data set given that the null hypothesis is true that is as extreme as or more extreme as the observed data set [100, 101]. In other words, it is the

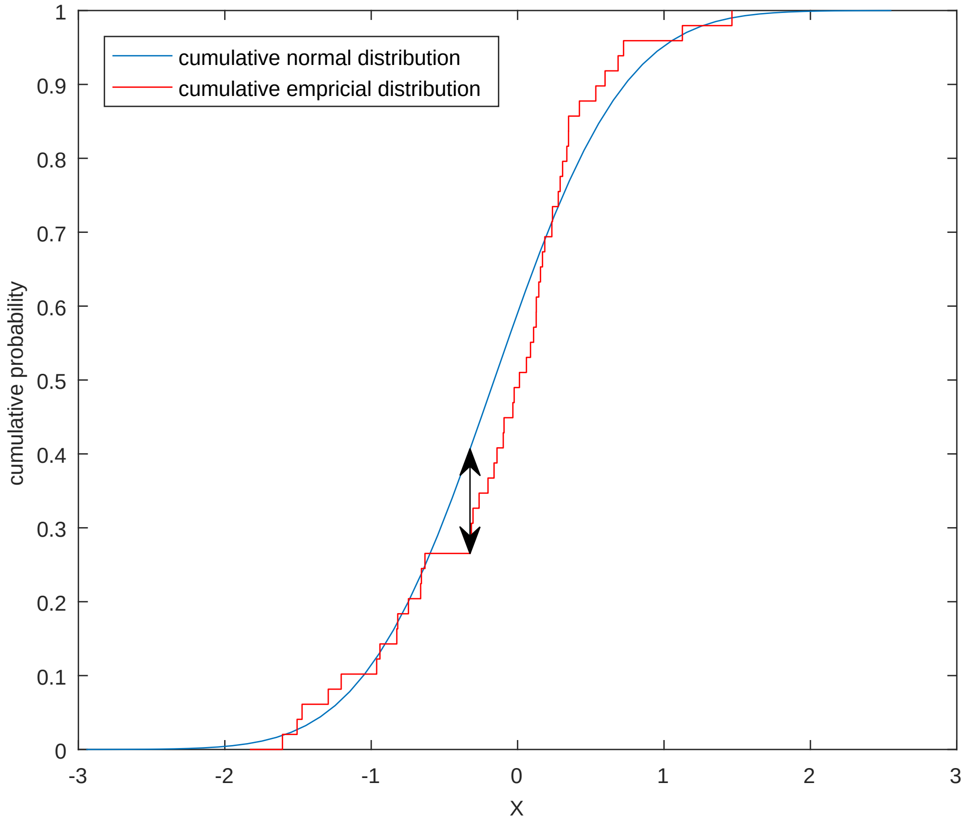

Figure A.1.: Comparison of normal and empirical cumulative distribution functions. The black double-arrow shows the calculated D of this example.

possibility to observe the measured D or a higher D given that the null hypothesis is true. Therefore, the probability to have a distribution that is closer to a normal distribution than the observed one is given by $1 - p$. The null hypothesis gets rejected in case $p \leq \alpha$.

Note once again the important fact, that comparison of D to a pre-calculated table of critical values for D and the numerical calculation of the p-value are the same procedure. In case of the Lilliefors test conducted for the laser-electron timing jitter, the function *lillietest* in *MATLAB 2013b* has been used with the option to conduct numerical Monte-Carlo simulations to calculate p.

Frequently Used Symbols

Symbol	Meaning
B	magnetic field
b_n	bunching factor on nth harmonic
β	velocity in multiples of the speed of light c
$\beta_\mathrm{x}, \beta_\mathrm{y}$	betatron function
c	speed of light
$\Delta\gamma$	modulation amplitude induced by seed laser in units of $m_\mathrm{e}c^2$
ΔW	absolute modulation amplitude induced by seed laser
E	FEL photon pulse energy; electric field
E_L	seed laser energy
ϵ_0	vacuum permittivity
ϵ_n	normalized emittance
ϵ_mx	geometrical mean of transverse emittances as used in Ming-Xie formalism
η	energy deviation
γ	Lorentz factor of electron bunch
I_A	Alfvén current $I_\mathrm{A} = 4\pi\epsilon_0 m_\mathrm{e}c^3/e \approx 17\,\mathrm{kA}$
k_l	wavenumber of FEL pulse $k_\mathrm{l} = 2\pi/\lambda_\mathrm{l}$
k_u	wavenumber of undulator $k_\mathrm{u} = 2\pi/\lambda_\mathrm{u}$
K	undulator parameter $K = \frac{eB_0}{m_\mathrm{e}ck_\mathrm{u}}$
K_JJ	corrected undulator parameter
L_g	FEL gain length
L_g0	one-dimensional FEL gain length
L_sat	saturation length of FEL process
λ_l	FEL wavelength
λ_u	undulator period
λ_seed	seed laser wavelength
M^2	beam quality factor
m_e	electron rest mass
μ	position of peak of Gaussian fit
μ_0	vacuum permeability
n	harmonic of seedlaser, $\lambda_\mathrm{n} = \lambda_\mathrm{seed}/n$
P	power
P_beam	beam power of electron beam
P_sat	saturation power of FEL process
R_ij	element of six-dimensional transfer matrix (ith row, jth column)
R_{56}	dispersive strength of bunching chicane
ρ_FEL	Pierce parameter
s	internal longitudinal bunch coordinate

S_{y}	shear parameter of transverse deflecting cavity
σ_{W}	rms energy spread of electron bunch
$\sigma_{\mathrm{x,l}}$	transverse seed laser beam size in x direction
σ_{l}	average transverse seed laser beam size
σ_{t}	rms FEL pulse duration
$\sigma_{\mathrm{t,l}}$	rms laser pulse duration
$\sigma_{\mathrm{t,e}}$	rms electron bunch duration
W_0	kinetic energy of electron bunch
ω	angular frequency $\omega = 2\pi f$
z	longitudinal beamline coordinate
z_{R}	Rayleigh length

Bibliography

[1] M. Altarelli and A. Salam, “The quest for brilliance: light source from the third to the fourth generation”, *europhysic news* (March/April 2004).

[2] H. Wiedemann, *Particle Accelerator Physics I*, Advanced Texts in Physics, Springer-Verlag Berlin Heidelberg, 2003.

[3] F. R. Elder et al., “Radiation from Electrons in a Synchrotron”, *Phys. Rev.* 71, 829–830, (1947), DOI: `10.1103/PhysRev.71.829.5`.

[4] G. v. Egan-Krieger et al., “Status of BESSY, an 800-MeV Storage Ring Dedicated to Synchrotron Radiation”, *IEEE T. Nucl. Sci.* NS-30, 3094–3096, (1993).

[5] D. Krämer, “Start of Commissioning of the High Brilliance Synchrotron Radiation Source BESSYII”, *Proc. of EPAC98*, 262–264, Stockholm, Sweden, (1998).

[6] J. M. J. Madey, “Stimulated Emission of Bremsstrahlung in a Periodic Magnetic Field”, *J. Appl. Phys.* 42, 1906–1913, (1971), DOI: `10.1063/1.1660466`.

[7] L. R. Elias et al., “Observation of Stimulated Emission of Radiation by Relativistic Electrons in a Spatially Periodic Transverse Magnetic Field”, *Phys. Rev. Lett.* 36, 717–720, (1976), DOI: `10.1103/PhysRevLett.36.717`.

[8] P. Schmüser et al., *Free-Electron Lasers in the Ultraviolet and X-Ray Regime*, Springer International Publishing, 2014.

[9] Z. Huang and K.-J. Kim, “Review of x-ray free-electron laser theory”, *Phys. Rev. ST Accel. Beams* 10, 034801, (2007), DOI: `10.1103/PhysRevSTAB.10.034801`.

[10] J. D. Jackson, *Classical electrodynamics*, 3rd ed., New York, NY: Wiley, 1999.

[11] A. Kondratenko and E. Saldin, “Generation of Coherent Radiation by a Relativistic Electron Beam in an Ondulator”, *Part. Accel.* 10, 207, (1980).

[12] R. Bonifacio et al., “Collective instabilities and high-gain regime in a free electron laser”, *Optics Communications* 50, 373–378, (1984), DOI: `10.1016/0030-4018(84)90105-6`.

[13] P. Schmüser et al., *Free-Electron Lasers in the Ultraviolet and X-Ray Regime: Physical Principles, Experimental Results, Technical Realization*, Springer Tracts in Modern Physics, Springer International Publishing, 2014.

[14] Ming Xie, “Exact and variational solutions of 3D eigenmodes in high gain FELs”, *Nucl. Instrum. Meth. A* 445, 59–66, (2000), DOI: `10.1016/S0168-9002(00)00114-5`.

[15] M. Xie, “Design Optimization for an X-Ray Free Electron Laser Driven by SLAC LINAC”, *Proc. of Particle Acc. Conf. 95*, 183–185, Dallas, Texas, (1995).

[16] Ya. S. Derbenev et al., “On the possibility of using a free electron laser for polarization of electrons in storage rings”, *Nucl. Instrum. Methods Phys. Res.* 193, 415–421, (1982), DOI: 10.1016/0029-554X(82)90233-6.

[17] S. Krinsky, “Stochastic Temporal Properties of the SASE FEL”, *Proc. of FEL2009*, 1–7, Liverpool, United Kingdom, (2009).

[18] E.L. Saldin et al., “Statistical properties of radiation from VUV and X-ray free electron laser”, *Opt. Commun.* 148, 383–403, (1998), DOI: 10.1016/S0030-4018(97)00670-6.

[19] M. Hogan et al., “Measurements of High Gain and Intensity Fluctuations in a Self-Amplified, Spontaneous-Emission Free-Electron Laser”, *Phys. Rev. Lett.* 80, 289–292, (1998), DOI: 10.1103/PhysRevLett.80.289.

[20] S. V. Milton et al., “Exponential Gain and Saturation of a Self-Amplified Spontaneous Emission Free-Electron Laser”, *Science* (2001), DOI: 10.1126/science.1059955.

[21] V. Ayvazyan et al., “A new powerful source for coherent VUV radiation: Demonstration of exponential growth and saturation at the TTF free-electron laser”, *Eur. Phys. J. D* 20, 149–156, (2002), DOI: 10.1140/epjd/e2002-00121-4.

[22] W. Ackermann et al., “Operation of a free-electron laser from the extreme ultraviolet to the water window”, *Nat. Photonics* 1, 336, (2007).

[23] J. Blau et al., “Free Electron Lasers in 2014”, 580–584, Basel, Switzerland, (2014).

[24] B. Faatz and S. Schreiber, “The free-electron laser FLASH”, *H. P. Laser* 3, e20, (2015).

[25] B. Faatz et al., “Simultaneous operation of two soft x-ray free-electron lasers driven by one linear accelerator”, *New J. Phys.* 18, 062002, (2016).

[26] S. Lederer et al., “Photocathodes at FLASH”, *Proc. of FEL2011*, 511–514, Shanghai, China, (2011).

[27] E. Vogel et al., “Test and Commissioning of the third harmonic rf System for FLASH”, *Proc. of 1st International Particle Accelerator Conference*, 4281–4283, Kyoto, Japan, (2010).

[28] K. Tiedtke et al., “Challenges for Detection of Highly Intense FEL Radiation: Photon Beam Diagnostics at FLASH1 and FLASH2”, *Proc. of FEL2013*, 417–420, New York, USA, (2013).

[29] S. Ackermann et al., “Generation of Coherent 19- and 38-nm Radiation at a Free-Electron Laser Directly Seeded at 38 nm”, *Phys. Rev. Lett.* 111, 114801, (2013), DOI: 10.1103/PhysRevLett.111.114801.

[30] L. H. Yu, “Generation of intense uv radiation by subharmonically seeded single-pass free-electron lasers”, *Phys. Rev. A* 44, 5178–5193, (1991), DOI: 10.1103/PhysRevA.44.5178.

[31] E. Hemsing et al., “Beam by design: Laser manipulation of electrons in modern accelerators”, *Rev. Mod. Phys.* 86, 897–941, (2014), DOI: 10.1103/RevModPhys.86.897.

[32] G. Dattoli et al., "Bunching and exotic undulator configurations in SASE FELs", *Nucl. Instrum. Meth. A* 507, Proceedings of the 24th International Free Electron Laser Conference and the 9th Users Workshop., 388–391, (2003), DOI: 10.1016/S0168-9002(03)00950-1.

[33] E. Jaeschke et al., *Synchrotron Light Sources and Free-Electron Lasers*, Springer International Publishing, 2016.

[34] G. Stupakov, "Using the Beam-Echo Effect for Generation of Short-Wavelength Radiation", *Phys. Rev. Lett.* 102, 074801, (2009), DOI: 10.1103/PhysRevLett.102.074801.

[35] D. Xiang and G. Stupakov, "Echo-enabled harmonic generation free electron laser", *Phys. Rev. ST Accel. Beams* 12, 030702, (2009), DOI: 10.1103/PhysRevSTAB.12.030702.

[36] L.-H. Yu et al., "High-Gain Harmonic-Generation Free-Electron Laser", *Science* 289, 932–934, (2000), DOI: 10.1126/science.289.5481.932.

[37] L. H. Yu et al., "First Ultraviolet High-Gain Harmonic-Generation Free-Electron Laser", *Phys. Rev. Lett.* 91, 074801, (2003), DOI: 10.1103/PhysRevLett.91.074801.

[38] M. Svandrlik et al., "FERMI Status Report", *Proc. of FEL2014*, 564–568, Basel, Switzerland, (2014).

[39] E. Allaria et al., "Two-stage seeded soft-X-ray free-electron laser", *Nat. Photon.* 7, Article, 913–918, (2013), DOI: 10.1038/nphoton.2013.277.

[40] Z. T. Zhao and D. Wang, "Seeded FEL Experiments at the SDUV-FEL Test Facility", *IEEE T. Nucl. Sci.* 63, 930–938, (2016), DOI: 10.1109/TNS.2016.2527678.

[41] G. Wang et al., "Harmonic Lasing Options for Dalian Coherent Light Source", *Proc. of IPAC2016*, 770–773, Busan, Korea, (2016).

[42] D. Xiang et al., "Demonstration of the Echo-Enabled Harmonic Generation Technique for Short-Wavelength Seeded Free Electron Lasers", *Phys. Rev. Lett.* 105, 114801, (2010), DOI: 10.1103/PhysRevLett.105.114801.

[43] E. Hemsing et al., "Echo-enabled harmonics up to the 75th order from precisely tailored electron beams", *Nat. Photon.* 10, Letter, 512–515, (2016), DOI: 10.1038/nphoton.2016.101.

[44] J. Bödewadt et al., "Recent Results from FEL Seeding at FLASH", *Proc. of IPAC2015*, 1366–1369, Richmond, United States of America, (2016).

[45] Z. T. Zhao et al., "First lasing of an echo-enabled harmonic generation free-electron laser", *Nat. Photon.* 6, 360–363, (2012), DOI: 10.1038/nphoton.2012.105.

[46] D. Hai-Xiao et al., "Simulation studies on laser pulse stability for Dalian coherent light source", *Chinese Phys. C* 38, 028101, (2014).

[47] J. Amann et al., "Demonstration of self-seeding in a hard-X-ray free-electron laser", *Nat. Photon.* 6, 693–698, (2012), DOI: 10.1038/nphoton.2012.180.

[48] D. Ratner et al., "Experimental Demonstration of a Soft X-Ray Self-Seeded Free-Electron Laser", *Phys. Rev. Lett.* 114, 054801, (2015), DOI: 10.1103/PhysRevLett.114.054801.

[49] P. Salén et al., "Results from the Optical Replica Synthesizer at FLASH", *Proc. of FEL2009*, 739–745, Liverpool, UK, (2009).

[50] M. Tischer et al., "Undulators of the sFLASH Experiment", *Proc. of IPAC10*, 3114–3116, Kyoto, Japan, (2010).

[51] J. Bödewadt et al., "A Compact Electron Photon Diagnostic Unit for a Seeded FEL", *Proc. of DIPAC09*, 203–205, Basel, Switzerland, (2009).

[52] Ph. Amstutz et al., "Confining continuous manipulations of accelerator beam-line optics", *Phys. Rev. Accel. Beams* 20, 042802, (2017), DOI: 10.1103/PhysRevAccelBeams.20.042802.

[53] N. Ekanayake et al., "Indirect Measurements of NIR and UV Ultrashort Seed Laser Pulses using a Transverse Deflecting RF-Structure", *Proc. of FEL2014*, 272–274, Basel, Switzerland, (2014).

[54] T. Plath et al., "Free-electron laser multiplex driven by a superconducting linear accelerator", *J. Synchrotron Rad.* 23, 1070–1075, (2016), DOI: 10.1107/S1600577516009620.

[55] M. Altarelli (ed.) et al., *The European X-Ray Free-Electron Laser Technical Design Report*, Report, Deutsches Elektronen Synchrotron DESY, 2007.

[56] R. Ganter (ed.) et al., *SwissFEL Conceptual Design Report*, Report, Paul Scherrer Institut PSI, 2010.

[57] J. Albino et al., *Linac Coherent Light Source II (LCLS-II) Conceptual Design Report*, Report, SLAC National Accelerator Laboratory, 2011.

[58] K. Tiedtke et al., "Gas detectors for x-ray lasers", *J. Appl. Phys.* 103, 094511, (2008).

[59] H. Wabnitz et al., "Multiple ionization of atom clusters by intense soft X-rays from a free-electron laser", *Nature* 420, 482–485, (2002), DOI: 10.1038/nature01197.

[60] U. Saalmann et al., "Mechanisms of cluster ionization in strong laser pulses", *J. Phys. B* 39, R39, (2006).

[61] Th. Fennel et al., "Laser-driven nonlinear cluster dynamics", *Rev. Mod. Phys.* 82, 1793–1842, (2010), DOI: 10.1103/RevModPhys.82.1793.

[62] Y. Ding et al., "Femtosecond x-ray pulse temporal characterization in free-electron lasers using a transverse deflector", *Phys. Rev. ST Accel. Beams* 14, 120701, (2011), DOI: 10.1103/PhysRevSTAB.14.120701.

[63] T. Plath et al., "Mapping few-femtosecond slices of ultra-relativistic electron bunches", *Sci. Rep.* 7 (2017), DOI: 10.1038/s41598-017-02184-3.

[64] M. Röhrs et al., "Time-resolved electron beam phase space tomography at a soft x-ray free-electron laser", *Phys. Rev. ST Accel. Beams* 12, 050704, (2009), DOI: 10.1103/PhysRevSTAB.12.050704.

[65] C. Behrens et al., "Few-femtosecond time-resolved measurements of X-ray free-electron lasers", *Nat. Commun.* 5 (2014), DOI: 10.1038/ncomms4762.

[66] D. Ratner et al., "Time-resolved imaging of the microbunching instability and energy spread at the Linac Coherent Light Source", *Phys. Rev. ST Accel. Beams* 18, 030704, (2015), DOI: 10.1103/PhysRevSTAB.18.030704.

[67] E.A. Schneidmiller and M.V. Yurkov, "Coherence properties of the radiation from FLASH", *J. Mod. Optic.* 63, 293–308, (2016), DOI: 10.1080/09500340.2015.1066456.

[68] C. Behrens and C. Gerth, "Measurement of the Slice Energy Spread induced by a Transverse Deflecting RF Structure at FLASH", *Proc. of DIPAC2011*, 371–373, Hamburg, Germany, (2011).

[69] W. K. H. Panofsky and W. A. Wenzel, "Some Considerations Concerning the Transverse Deflection of Charged Particles in Radio-Frequency Fields", *Rev. Sci. Instrum.* 27, 967–967, (1956), DOI: 10.1063/1.1715427.

[70] M. Borland, "elegant: A Flexible SDDS-Compliant Code for Accelerator Simulation", *Advanced Photon Source LS-287* (Septmeber 2000).

[71] E. Prat and M. Aiba, "Four-dimensional transverse beam matrix measurement using the multiple-quadrupole scan technique", *Phys. Rev. ST Accel. Beams* 17, 052801, (2014), DOI: 10.1103/PhysRevSTAB.17.052801.

[72] E. Prat and M. Aiba, "Four-dimensional transverse beam matrix measurement using the multiple-quadrupole scan technique", *Phys. Rev. ST Accel. Beams* 17, 052801, (2014), DOI: 10.1103/PhysRevSTAB.17.052801.

[73] M. E. Hernandez, "Four Dimensional Trace Space Measurement", PhD thesis, Stanford University, 2003.

[74] This work was created in collaborations with M. Dohlus and Ch. Lechner.

[75] E. A. Schneidmiller and M. V. Yurkov, "Using the longitudinal space charge instability for generation of vacuum ultraviolet and x-ray radiation", *Phys. Rev. ST Accel. Beams* 13, 110701, (2010), DOI: 10.1103/PhysRevSTAB.13.110701.

[76] Z. Huang et al., "Suppression of microbunching instability in the linac coherent light source", *Phys. Rev. ST Accel. Beams* 7, 074401, (2004), DOI: 10.1103/PhysRevSTAB.7.074401.

[77] C. Lechner et al., "Demonstration of SASE Suppression Through a Seeded Microbunching Instability", *Proc. of the FEL2014*, 177–180, Basel, Switzerland, (2014).

[78] M. Dohlus and Ch. Henning, "Periodic Poisson model for beam dynamics simulation", *Phys. Rev. Accel. Beams* 19, 034401, (2016), DOI: 10.1103/PhysRevAccelBeams.19.034401.

[79] M. Dohlus, private communication.

[80] D. Ratner et al., "Laser phase errors in seeded free electron lasers", *Phys. Rev. ST Accel. Beams* 15, 030702, (2012), DOI: 10.1103/PhysRevSTAB.15.030702.

[81] G. Stupakov, "Effect of finite pulse length and laser frequency chirp on HGHG and EEHG seeding", *SLAC-PUB-14639* (2011).

[82] S. Reiche, "GENESIS 1.3: a fully 3D time-dependent FEL simulation code", *Nucl. Instrum. Meth. A* 429, 243–248, (1999), DOI: `10.1016/S0168-9002(99)00114-X`.

[83] H. W. Lilliefors, "On the Kolmogorov-Smirnov Test for Normality with Mean and Variance Unknown", *J. Am. Stat. Assoc.* 62, 399–402, (1967).

[84] A. Meseck et al., "HGHG Scheme for FLASH II", *Proc. of the FEL2011*, 107–110, Shanghai, China, (2011).

[85] M. Feldhaus et al., "Possible application of X-ray optical elements for reducing the spectral bandwidth of an X-ray SASE FEL", *Opt. Commun.* 140, 341–352, (1997).

[86] Y. Feng et al., "System Design for Self-Seeding the LCLS at Soft X-Ray Energies", *Proc. of FEL2012*, Nara, Japan, (2012).

[87] E. Hecht, *Optik*, 5. Auflage, München: Oldenbourg Wissenschaftsverlag, 2009.

[88] F. Schäfers, "Beschreibung des Programms REFLEC", *BESSY Technischer Bericht Nr. 157* (1990).

[89] J. Gaudin et al., "Investigating the interaction of x-ray free electron laser radiation with grating structure", *Opt. Lett.* 37, 3033–3035, (2012), DOI: `10.1364/OL.37.003033`.

[90] Ya. S. Derbenev et al., *Microbunch Radiative Tail-Head Interaction*, Report, Deutsches Elektronen-Synchrotron, 1995.

[91] Ya. S. Derbenev et al., "Microbunch Emittance Growth Due to Radiative Interaction", *Proc. of EPAC1996*, Barcelona, Spain, (1996).

[92] M. Dohlus and T. Limberg, "CSRtrack: Faster Calculation of 3-D CSR Effects", *Proc. of the 2004 FEL Conference*, 18–21, Trieste, Italy, (2004).

[93] S. Serkez et al., "Grating monochromator for soft X-ray self-seeding the European XFEL", *ArXiv e-prints* (2013).

[94] G. Feng et al., "Seeded FEL Study for Cascaded HGHG Option for FLASH2", *Proc. of FEL2015*, 246–250, Daejeon, Japan, (2015).

[95] This work was created in collaborations with J.Bödewadt, G. Feng and Ch. Lechner.

[96] W. M. Fawley, "Algorithm for loading shot noise microbunching in multidimensional, free-electron laser simulation codes", *Phys. Rev. ST Accel. Beams* 5, 070701, (2002), DOI: `10.1103/PhysRevSTAB.5.070701`.

[97] S. Ackermann, "Experimental and numerical investigations on seeding options for the multi-beam line Free-Electron Laser facility FLASH", PhD thesis, University of Hamburg, 2016.

[98] N. Kroll et al., "Free-electron lasers with variable parameter wigglers", *IEEE J. Quantum Elect.* 17, 1436–1468, (1981), DOI: `10.1109/JQE.1981.1071285`.

[99] E. A. Schneidmiller and M. V. Yurkov, "Optimization of a high efficiency free electron laser amplifier", *Phys. Rev. ST Accel. Beams* 18, 030705, (2015), DOI: `10.1103/PhysRevSTAB.18.030705`.

[100] J. L. Devore, *Probability and Statistics for Engineering and the Sciences*, Brooks/Cole, 2010.

[101] G. Bohm and G. Zech, *Introduction to Statistics and Data Analysis for Physicists*, Verlag Deutsches Elektronen-Synchrotron, 2010.

Acknowledgements

It goes without saying that a PhD thesis conducted at a large and complex facility like FLASH is not possible without the support of many people. I want to thank Prof. Dr. Jörg Roßbach for being the supervisor for my doctoral thesis and for giving me the opportunity to work in his research group. He always offered helpful advice and fruitful discussions on all aspects of my work, whether it was the big picture or pen and pencil physics.

I would not have been able to conclude my thesis in time without the exceptional help of my advisor Dr. Jörn Bödewadt. Over more than three years, he always had an open door and supported me in all challenges I had to overcome. His pragmatic advice and experimental experience took a crucial role in taking forward my PhD project.

I am grateful to the FLASH seeding team for the good atmosphere during work days as well as nights. I am thankful to Dr. Nagitha Ekanayake who kept the seed laser system running at optimum performance and paved the way for the experimental data presented in my thesis. Many thanks to Dr. Velizar Miltchev for educating me in statistics and for his device on data analysis. Thanks to Dr. Theophilos Maltezopulos for a constant supply of coffee and latest flight information (D'oh!). Especially thankful I am to my fellow PhD colleagues Dr. Sven Ackermann, Leslie Lamberto Lazzarino and Dr. Christoph Lechner. Christoph was always of great help regarding almost every aspect of my work and at all times had a proposal up his sleeves to improve myself.

I want to express my gratitude to Priv.-Doz. Dr. Tim Laarmann who constantly encouraged me to publish my findings and was of extraordinary help when it came down to preparing and editing my manuscripts.

I would like to express my gratitude to the FEL beam dynamics group at DESY. In particular, Dr. Igor Zagorodnov and Dr. Martin Dohlus, who always offered their advice when needed.

I am thankful to Dr. Jörn Bödewadt, Dr. Velizar Miltchev and Dr. Christoph Lechner for proofreading chapters of this work.

For their coordinative work at the FLASH accelerator, I want to thank the FLASH machine coordinator team as well as the team of machine operators for their help during experimental campaigns. I am thankful to Fenna Reinholdt and Heike Kaminski for their administrative support.

Finally, all of this would not have been possible without the support of my friends, my family and my partner Kim. I am very grateful for the countless joyful hours I spent with my friends that balanced even the most challenging days during these years. I am thankful to my family for providing me with unfailing support and continuous encouragement throughout my years of study and through the process of researching and writing my thesis. I am grateful to you, Kim, for your unconditional support and love during the last years. You always believed in me and gave me something to hold on to.

Eidesstattliche Versicherung

Hiermit erkläre ich an Eides statt, dass ich die vorliegende Dissertationsschrift selbst verfasst und keine anderen als die angegebenen Quellen und Hilfsmittel benutzt habe.

Die eingereichte schriftliche Fassung entspricht der auf dem elektronischen Speichermedium.

Die Dissertation wurde in der vorgelegten oder einer ähnlichen Form nicht schon einmal in einem früheren Promotionsverfahren angenommen oder als ungenügend beurteilt.

Hamburg, den ____________________ ________________________________

Tim Plath